Università degli Studi di Torino
Dipartimento di Fisica
Corso di Laurea Magistrale in Fisica

Tesi di Laurea Magistrale in Fisica

Characterization and performance of 3D silicon pixel detectors for CMS

Relatore
Prof. Ada Solano

Co-relatore
Dott. Maria Margherita Obertino

Candidato
Fabio Ravera

Anno accademico 2012-2013

Sommario

L'upgrade di LHC, denominato High Luminosity-LHC (HL-LHC), prevede di aumentarne la luminosità fino a raggiungere 10^{35} cm^{-2}s^{-1}, ponendo nuove sfide, in particolare a causa dell'alto livello di radiazioni. Nelle condizioni previste, i rivelatori al silicio a pixel degli strati interni del sistema di tracciamento di CMS dovranno sopportare un livello di irraggiamento pari a $\sim 10^{16}$ n$_{eq}$/cm^2. Poiché gli attuali sensori sono qualificati per una tolleranza alle radiazioni inferiore, si è reso necessario iniziare un programma di ricerca e sviluppo per lo studio di nuovi rivelatori più resistenti alle radiazioni. Tra i possibili candidati, i rivelatori al silicio a pixel 3D sembrano essere tra le soluzioni più promettenti per questo tipo di applicazioni. Questi rivelatori sono caratterizzati da elettrodi a colonna scavati attraverso il bulk di silicio. Grazie a questa tecnologia si riescono ad ottenere interessanti proprietà in termini di resistenza alle radiazioni.

Per introdurre l'argomento, il primo capitolo presenta una panoramica sulle proprietà del silicio e sull'interazione delle particelle con la materia. Il secondo capitolo è dedicato ai rivelatori a pixel ibridi ed in particolare alle caratteristiche dei rivelatori 3D prodotti dalla Fondazione Bruno Kessler (FBK) di Trento (Italia), dal Centro Nacional de Microelectrónica (CNM) di Barcellona (Spagna) e dalla SINTEF di Trondheim (Norvegia). Vengono inoltre presentati i principali risultati ottenuti su questi rivelatori dalla ATLAS 3D Collaboration.

Questa tesi è focalizzata sul lavoro di sviluppo e realizzazione di una procedura di laboratorio per la caratterizzazione di rivelatori a pixel 3D per CMS. Il terzo capitolo è dedicato alle misure di corrente di buio, rumore e raccolta di carica, queste ultime realizzate con l'uso di una sorgente radioattiva. Viene inoltre illustrata la calibrazione del chip di lettura.

Il quarto capitolo descrive il lavoro svolto per approntare un setup per misure di efficienza con il laser su rivelatori di silicio a pixel, basato sull'idea di simulare con un laser da 1060 nm il passaggio di una particella. Verranno presentate le mappe di efficienza ottenute con la scansione laser sull'area di un singolo pixel.

Abstract

The LHC luminosity upgrade, referred to as High Luminosity-LHC (HL-LHC), will increase the luminosity up to 10^{35} $cm^{-2}s^{-1}$, posing several challenges mainly because of the expected high radiation levels. In this conditions, the CMS silicon pixel detectors of the inner layers of the tracking system will need to withstand particle fluences up to $\sim 10^{16}$ n_{eq}/cm^2, and the low radiation tolerance of the currently available silicon sensor technology becomes an issue, requiring to design and test new radiation-hard sensors. Among the proposed candidates, 3D silicon sensors seem to be one of the more promising for applications in these scenarios. These types of detector use columnar electrodes etched through the silicon bulk. Thanks to this technology, interesting properties of radiation hardness are obtained.

For introducing the argument, an overview on silicon properties and particle detection is presented in the first chapter. The second chapter is dedicated to hybrid pixel detectors, and in particular the features of 3D silicon sensors produced by Fondazione Bruno Kessler (FBK) in Trento, Italy, Centro Nacional de Microelectrónica (CNM) in Barcelona, Spain and SINTEF in Trondheim, Norway, are described. The main results obtained with these devices by the ATLAS 3D Collaboration are also presented.

This thesis focuses on the work done to develop and set up the laboratory characterization procedure for the CMS 3D silicon pixel detectors. The third chapter is dedicated to the measurements of the leakage current, the noise and the charge collection, the latter done with a radioactive source test. The readout chip calibration procedure is also explained.

The fourth chapter presents the realization of a laser setup for silicon pixel detector measurements, based on the idea of simulating a minimum ionizing particle with a 1060 nm laser, in order to study the efficiency of the detectors. Measurements of the efficiency map obtained by scanning a single pixel area are shown.

Contents

Chapter 1

Semiconductor detectors

This chapter describes particle interaction with matter and how the charge deposited in a material can be used to obtain information on the particle passage. In particular, semiconductor detectors are presented and the effect of radiation damage is investigated.

1.1 Particle interaction with matter

Interactions of particles with matter can be distinguished in directly and indirectly ionizing. The first ones are characteristic of charged particles, which directly excite or ionize atoms and molecules with electromagnetic interaction. In this case, the energy is lost almost continuously across the material. Indirect ionization is instead typical of neutral particles like photons or neutrons, which generate secondary particles which then produce excitation or ionization. In this type of interaction the particle energy is usually lost in a single collision. These events are particularly interesting because the energy deposited in the interaction is known exactly and can be used for calibration. Interactions of charged particles and photons, mainly with silicon, will be now briefly described.

1.1.1 Energy loss by charged particles

Charged particles crossing a medium are mainly subject to electromagnetic interactions, in the form of inelastic collisions with electrons or elastic collisions with nuclei. The first ones lead to a gradual energy loss which excites atoms or produces electron-ion pairs (ionization). In particular, electrons emitted in the latter process can have an energy higher than the material ionizing potential and furthermore ionize atoms, creating secondary electrons

called δ rays. On the contrary, elastic collisions with nuclei produce a lateral diffusion of the incoming particle (multiple scattering) without appreciable energy loss.

For small mass ionizing particles, beside the interactions described above, other electromagnetic processes such as bremsstrahlung, Cerenkov effect and transition radiation, become relevant. For this reason, in describing charged particles energy loss in matter, it is necessary to consider separately light mass particles, such as electrons and positrons, and heavy mass particles, such as muons, pions, protons and ions.

Stopping power

The mean value of energy loss per unit path length is called stopping power:

$$S = -\frac{dE}{dx} \tag{1.1.1}$$

where E is the energy and x the path length. The minus sign makes S positive. The stopping power depends on the interacting particle and on the material crossed.

A more useful way to define the energy loss is the mass stopping power:

$$S_m = -\frac{dE}{d(\xi)} = -\frac{dE}{d(\rho x)} = -\frac{1}{\rho}\frac{dE}{dx} \tag{1.1.2}$$

where ρ is the material density. Defining S_m in this way it does not differ greatly for materials with similar atomic composition.

Energy loss by heavy charged particles

The mean energy loss of a heavy charged particle in matter is described by the Bethe-Bloch formula [1]:

$$\frac{dE}{d\xi} = 2\pi N_{AV} r_e^2 m_e c^2 \frac{Z}{A}\frac{z^2}{\beta^2}\left[ln\left(\frac{2m_e\gamma^2 v^2 W_{max}}{I^2}\right) - 2\beta^2 - \delta - 2\frac{C}{Z}\right] \tag{1.1.3}$$

where terms in eq. 1.1.3 are described in table 1.1.

As shown in fig. 1.1 [2], defining the energy loss in terms of the path length expressed in g/cm^2, its dependence on the particle momentum is almost the same. In particular, the minimum energy loss is $1 \div 2$ MeVcm^2/g for all materials, with the exception of H_2. For silicon $< dE/d\xi >_{min} \sim$ 1.66 MeVcm^{2}g^{-1}. A particle with an energy loss in the minimum of the Bethe-Bloch formula is called minimum ionizing particle (MIP). Due to the flatness

$\frac{dE}{d\xi}$	particle energy loss
$2\pi N_{AV} r_e^2 m_e c^2$	0.1535 MeVc^2/g
ξ	path length in g/cm^2
r_e	classical electron radius
m_e	electron mass
N_{AV}	Avogadro's number
I	effective ionizing potential avaraged over all electrons
Z	atomic number of the medium
A	atomic weight of the medium
z	particle charge
β	velocity of the traversing particle in units of the speed of light
γ	$\frac{1}{\sqrt{1-\beta^2}}$
δ	density correction
C	shell correction
W_{max}	maximum energy transfer in a single collision

Table 1.1: Parameters of the Bethe-Bloch formula (eq. 1.1.3).

(fig. 1.1) of the function after the minimum, the so-called Fermi plateau, this expression is often used to refer to all particles with $\beta\gamma > 3$.

Fig. 1.2 [2] shows the energy loss of a muon in copper. From the plot it can be seen that for $\beta\gamma < 0.007$ the Bethe-Bloch formula is not valid anymore. This happens because the particle has a speed almost equal to the one of the electrons of the material and it is absorbed. In fig. 1.2 it is also visible the effect of radiative losses, which for heavy particles only occur at high energy.

The energy deposit can be measured in terms of charge produced, since a ionizing particle produces an amount of electron-ion pairs proportional to the energy loss. This is due to the fact that in each medium a fixed energy value for the production of a pair is needed.

The fluctuation of the energy loss, and as a consequence of the charge deposit, in a thin layer of matter produces an asymmetric distribution. The typical shape is a narrow peak with a long tail at higher values of energy. This effect is due to the small number of collisions with a high energy loss. The mathematical expression of this function is the so-called Landau distribution. In particular, for a 250 μm thick silicon sensor, the expected distribution is shown in fig. 1.3 [3].

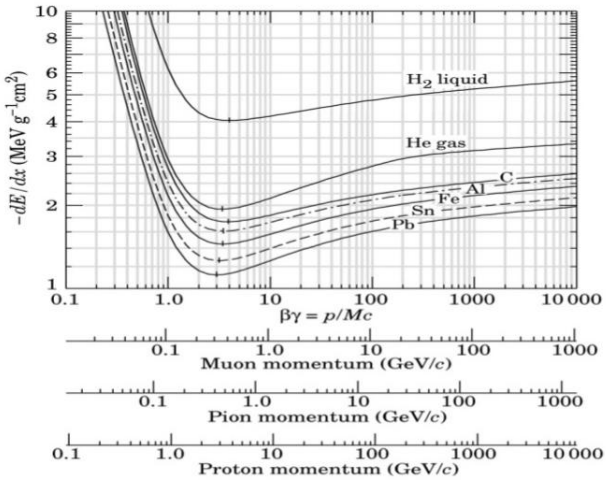

Figure 1.1: Energy loss for heavy charged particles in different materials.

Energy loss by light charged particles

In case of electrons, because of their low mass, the contribution to the energy loss due to photon radiation, the so-called bremsstrahlung, is relevant and must be taken into account in the overall energy loss:

$$\langle\frac{dE}{d\xi}\rangle = \left(\frac{dE}{d\xi}\right)_{Brem} + \left(\frac{dE}{d\xi}\right)_{Ion} \tag{1.1.4}$$

The radiative energy loss is described by:

$$-\frac{1}{\rho}\left(\frac{dE}{dx}\right)_{Brem} = \frac{E}{X_0} \tag{1.1.5}$$

with

$$\frac{1}{X_0} = \frac{4Z(Z+1)N_{AV}}{137A} r_0^2 ln\frac{183}{Z^{\frac{1}{3}}} \tag{1.1.6}$$

where X_0 is called radiation length and it is the distance within which the electron energy is reduced by a factor e. For the other parameters the notation is the same of table 1.1.

At relativistic energy, the ratio of the energy loss by bremsstrahlung to the one by ionization is proportional to the particle kinetic energy and to the atomic number of the crossed material:

$$\frac{\left(\frac{dE}{dx}\right)_{Brem}}{\left(\frac{dE}{dx}\right)_{Ion}} = \frac{1}{580}ZE \tag{1.1.7}$$

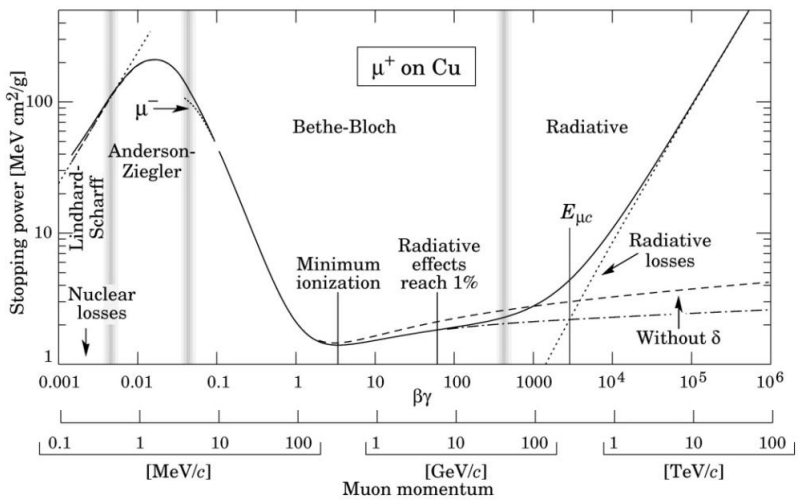

Figure 1.2: Energy loss of a muon in copper.

from where it is possible to determine the critical energy E_c at which the energy loss by radiation is equal to the one by ionization:

$$E_c \sim \frac{580\,\mathrm{MeV}}{Z} \tag{1.1.8}$$

1.1.2 Interaction of photons with matter

Interaction of photons in matter depends on their energy. The main three processes are: photoelectric effect, Compton scattering and pair production. The overall absorption of a beam of photons can be described with an exponential law:

$$N(x) = N_0 e^{-\mu_L x} \tag{1.1.9}$$

where N_0 is the number of incident photons, $N(x)$ is the number of photons still present after a path distance x, and μ_L is the linear absorption coefficient given by:

$$\mu_L = \frac{\sigma N_A \rho}{A} \equiv \frac{1}{\lambda} \tag{1.1.10}$$

with σ the total cross section, and the other parameters as in table 1.1. The inverse of μ_L is defined as attenuation length or mean free path λ, and represents the average distance travelled by a photon before being absorbed.

The total cross section is obtained by the sum of the three main processes introduced above:

$$\sigma = \sigma_{Photoelectric} + \sigma_{Compton} + \sigma_{Pair} \tag{1.1.11}$$

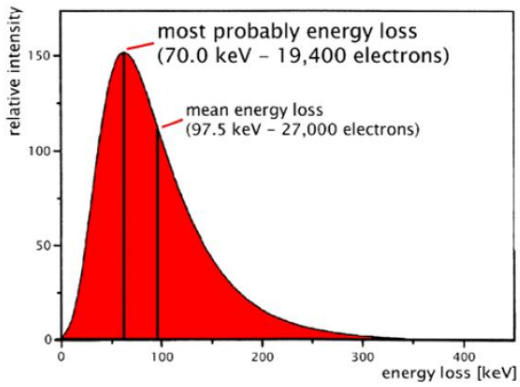

Figure 1.3: Landau distribution expected for a MIP crossing a 250 μm thick silicon sensor.

The photoelectric effect consists in the absorption of a photon with the subsequent emission of an electron from one of the shells of the hit atom. In order to break the bounded state of the atomic electron, the energy of the photon, E_γ, must exceed the ionization potential of the matter crossed. As a consequence, the emitted electron carries the remaining energy E_e:

$$E_e = E_\gamma - E_B \tag{1.1.12}$$

where E_B is the ionization potential. This process, which dominates at photon energies lower than 100 keV, is useful for detector calibration because, neglecting the threshold energy E_B, the energy lost in the collision is known, in particular using gamma radioactive elements like ^{241}Am and ^{109}Cd.

The Compton scattering takes place when a photon scatters off an electron, yielding a photon of lower frequency, and therefore lower energy, with a different direction. The absorption cross section of this interaction is small at low energy, rises to a peak at photon energy of the order of 1 MeV and declines at higher energy.

The pair production occurs when a photon is converted into an electron-positron pair. Due to the conservation of angular momentum, the phenomenon must happen in a medium, where virtual photons produced by nuclei of the material allow to respect the angular momentum conservation law. The photon energy at which the process starts to take place is $2m_ec^2 \sim 1.022$ MeV.

The sum of these three contributions is shown in fig. 1.4 for a 300 μm thick silicon [4].

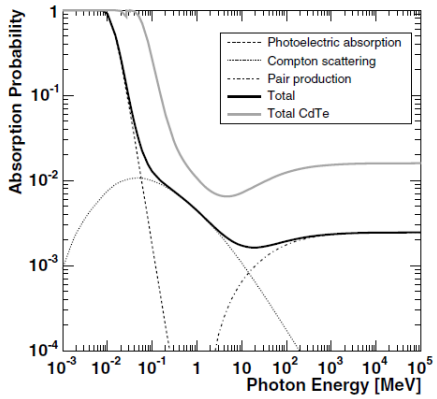

Figure 1.4: Probability of photon absorption in 300 μm silicon as a function of the photon energy and comparison with CdTe of the same thickness.

1.2 Silicon properties

Thanks to its interesting characteristics, silicon is the most common semiconductor material used in electronics. It has four valence electrons, so it forms covalent bounds with four nearby atoms. Its structure, projected on a plane, is shown in fig. 1.5. The number of free electrons depends on the temperature. Considering that electrons must respect the Pauli exclusion principle[1], the Fermi energy is defined as the energy of the electron in the highest occupied state of a material at the temperature of 0 K.

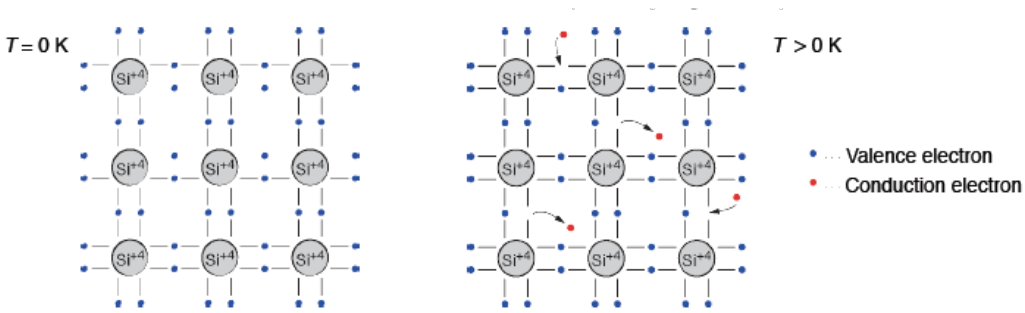

Figure 1.5: Two-dimensional representations of the silicon lattice, showing the different behaviour of the material at different temperatures.

Increasing the temperature, the probability for having conduction electrons increases. In particular, the Fermi-Dirac statistics leads to an energy

[1]The Pauli exclusion principle says that the probability of finding two fermions (particle with spin 1/2) in the same state is null.

distribution given by

$$f(E) = \frac{1}{1 + e^{\frac{E-E_F}{kT}}} \tag{1.2.1}$$

where E is the energy of the electrons, E_F the Fermi energy, T the temperature of the system and k the Boltzmann constant. The distribution at different temperatures is shown in fig. 1.6.

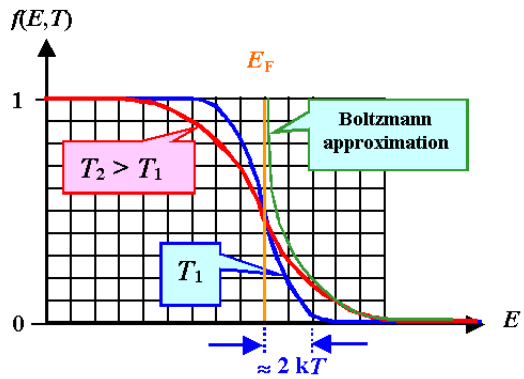

Figure 1.6: The Fermi-Dirac distribution at different temperatures.

An interesting characteristic of semiconductor materials like silicon is that the hole produced when an electron is removed from its energy level in turn attracts an electron. Unbounding this electron a new hole is produced while the first one is filled. The result is that holes move in the material and participate to the conduction. For intrinsic[2] silicon, since for each free electron there is a hole, the carrier density is the same for electrons n and holes p ($n_i = n_n = n_p = 1.45 \cdot 10^{10}/\text{cm}^3$ [5]) and it is a function of the temperature:

$$n_i = T^{\frac{3}{2}} \cdot \exp\left(-\frac{E_{gap}}{2kT}\right) \tag{1.2.2}$$

where E_{gap} is the energy gap between the conduction and valence bands (see sec. 1.2.1).

The drift velocity of the carriers is written as

$$\vec{v}_{p,n} = \pm\mu_{p,n}\,\vec{E} \tag{1.2.3}$$

where $\vec{E}$ is the electric field and $\mu_{p,n}$ are the mobilities of holes and electrons given by

$$\mu_{p,n} = \frac{e\,\tau_{p,n}}{m_{p,n}} \tag{1.2.4}$$

[2]Intrinsic silicon means that the crystal is without impurities.

with e the electron charge, $\tau_{p,n}$ the mean free time between two collisions, and $m_{p,n}$ the effective mass of holes and electrons. In silicon, the mobilities of the two carriers are constant to a good approximation when the electric field is below 1 kV/cm. At a temperature of 300 K the mobilities are:

$$\mu_n \sim 1400 \text{ cm}^2\text{V}^{-1}\text{s}^{-1} \tag{1.2.5}$$

$$\mu_p \sim 450 \text{ cm}^2\text{V}^{-1}\text{s}^{-1} \tag{1.2.6}$$

To define the resistivity both charge carriers must be considered:

$$\rho = \frac{1}{e\left(\mu_n n_n + \mu_p n_p\right)} \tag{1.2.7}$$

Using the values above, the intrinsic silicon resistivity can be evaluated to be ~ 230 Ωcm at a temperature of 300 K.

1.2.1 Band structure

From quantum mechanics it is known that in a single atom the electrons only stay in discrete levels of definite energy. However, this description is not useful to understand the behaviour of a lattice of atoms. In fact, due to the huge number of electrons, the energy levels form continuous bands that can be separated by not-allowed energy regions. The extension of these forbidden gaps is the characteristic which determines the electric behaviour of a material.

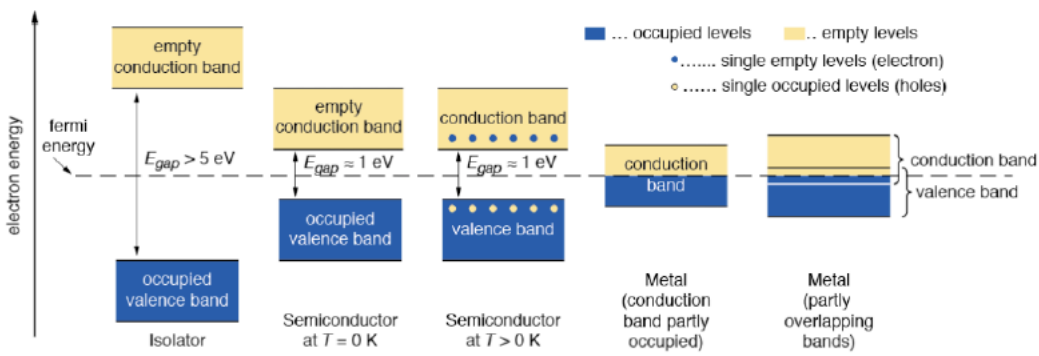

Figure 1.7: Representation of the band structures for isolators, semiconductors and metals.

The highest energy band which at 0 K is completely filled is called valence band, and the next more energetic, which can be empty or partially filled, conduction band. Figure 1.7 shows the band structure of isolator,

semiconductor and conductor materials. As one can see, both isolators and semiconductors have a gap between the two bands, but in semiconductors the energy of the forbidden region is significantly lower than in isolators. For silicon this value is $E_{gap} = 1.11$ eV. For metals, the two bands are partially overlapped or the conduction band is partially filled, ensuring the current passage.

1.2.2 Doping

For using silicon to detect particles, it is necessary that the charge deposited in the material is well distinguishable from the amount of free carriers due to thermal effects. Considering an intrinsic silicon detector of thickness $d = 300$ μm and area $A = 1$ cm^2 at the temperature of 300 K, the amount of free carriers due to thermal effects, which is the noise, can be expressed as

$$noise = n_i \cdot d \cdot A \sim 4.35 \cdot 10^8 \, e^- h^+ \, pairs \tag{1.2.8}$$

The mean energy needed for producing an electron-hole pair in silicon is $I_0 = 3.62$ eV. A MIP in silicon has an energy loss for path length unit of $dE/dx = 3.87$ MeV/cm. Thus, the expected signal is:

$$\frac{dE/dx \cdot d}{I_0} \sim 3.2 \cdot 10^4 \, e^- h^+ \, pairs \tag{1.2.9}$$

which is four orders of magnitude lower than the noise. As a consequence, intrinsic silicon cannot be used for particle detection, but it must be doped and then depleted from free carriers by means of a n-p junction (see sec. 1.2.3).

To dope a semiconductor, atoms of another element need to be introduced in the material to change its electric characteristics. The idea is to insert a surplus of electrons in the conduction band (n-type doping) or holes in the valence band (p-type doping). To do this, donor or acceptor atoms must be added to the silicon, respectively. Acceptors are atoms with five valence electrons (group V in the periodic table), while donors have three (group III). The resulting silicon lattice is shown in fig. 1.8.

It can be shown that for maintaining the property of semiconductor and therefore producing a so-called non-degenerate semiconductor, the densities of electrons and holes must respect the mass-action law:

$$n_n \cdot n_p = n_i^2 \tag{1.2.10}$$

It is also important to introduce the concept of majority and minority carriers. In a p-type silicon holes are majority and electrons are minority carriers and vice versa for a n-type silicon.

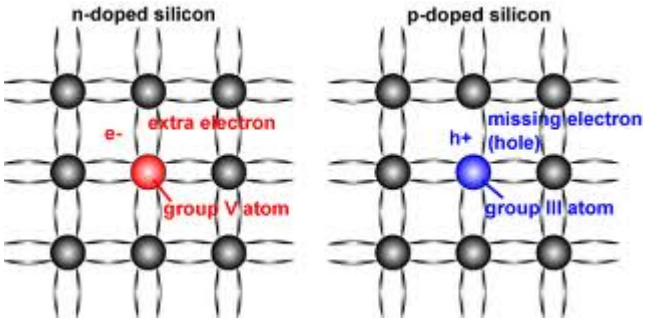

Figure 1.8: Two dimensional representation of doped silicon lattice.

The Fermi level of a semiconductor lies very close to the middle of the gap. It is possible to demonstrate that by the addition of acceptor or donor atoms, the Fermi level shifts towards the valence or the conduction band, respectively [5]. This effect is shown in fig. 1.9.

1.2.3 n-p junction

As already said in sec. 1.2.2, it is not possible to detect a particle with intrinsic silicon due to the free carriers produced by thermal effect. The way out is to create a region depleted from free charges. This is obtained by means of a n-p junction. The idea is to connect two different doped silicons with the result that electrons from the n-type diffuse towards the p-type, which have a much smaller concentration of them, while the holes make the opposite process. The diffusion produces a current density $J_{p,n}$ proportional to the gradient of charge along the direction of flow:

$$J_n = +q\, D_n \frac{dn_n}{dx} \tag{1.2.11}$$

$$J_p = -q\, D_p \frac{dn_p}{dx} \tag{1.2.12}$$

where $D_{n,p}$ are the diffusion constants of electrons and holes, respectively.

Diffusion leaves fix charges due to acceptor and donor ions, creating an electric field in the region around the junction. The equilibrium is reached when the current produced by the electric field is the same as the one due to diffusion:

$$q\, D_n \frac{dn}{dx} + q\mu_n n_n E = 0 \tag{1.2.13}$$

$$-q\, D_p \frac{dp}{dx} + q\mu_p n_p E = 0 \tag{1.2.14}$$

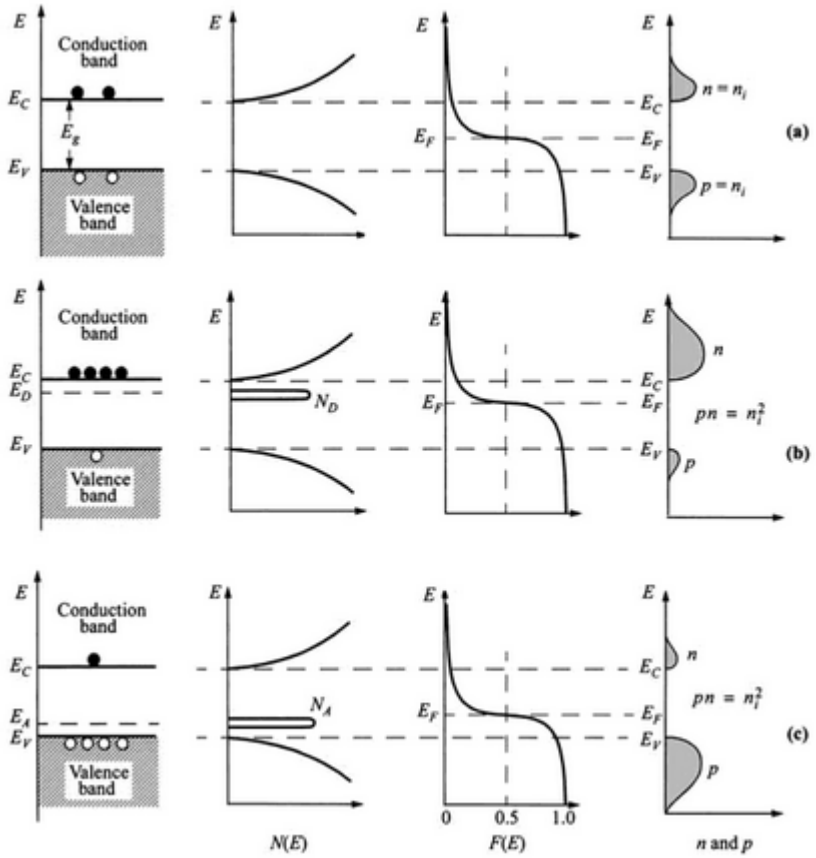

Figure 1.9: Schematic band diagrams, density states, Fermi-Dirac distributions and carrier concentrations for (a) intrinsic, (b) n-type, and (c) p-type semiconductors. Note that $n_n \cdot n_p = n_i^2$ for all cases [5].

As a consequence, the so-called built-in potential ψ_{bi} is induced in the junction and the region nearby the junction, called depletion region, becomes empty of free charges. The n-p junction allows to use doped silicon as particle detector since the charge deposited by a particle will not be hidden by the noise as it happens in intrinsic silicon.

To increase the detection capability, different doping concentrations and the reverse biasing can be used. What happens in the depletion region is shown in fig. 1.10.

It is possible to demonstrate [5] that the extension of the depletion region in the two different substrates (W_{Dp} in the p-type and W_{Dn} in the n-type) depends on the doping concentration N_A (acceptor concentration) and N_D

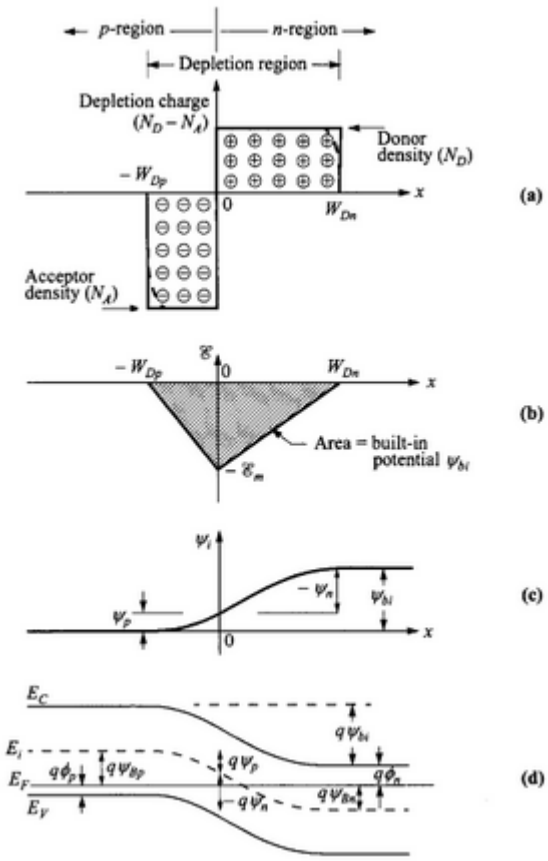

Figure 1.10: *p-n* junction in thermal equilibrium. (a) spatial charge, (b) electric field and (c) potential distribution and (d) energy band diagram.

(donor concentration), as shown in eq. 1.2.15 and 1.2.16

$$W_{Dp} = \sqrt{\frac{2\varepsilon_0\varepsilon_{Si}\psi_{bi}}{q}\frac{N_D}{N_A(N_A+N_D)}} \tag{1.2.15}$$

$$W_{Dn} = \sqrt{\frac{2\varepsilon_0\varepsilon_{Si}\psi_{bi}}{q}\frac{N_A}{N_D(N_A+N_D)}} \tag{1.2.16}$$

where ε_{Si} with the relative silicon dielectric constant.

Changing the doping concentrations, it is thus possible to unbalance the extension of the depletion region in one direction with respect to the junction contact, and also to modify the total width:

$$W_D = W_{Dp} + W_{Dn} = \sqrt{\frac{2\varepsilon_0\varepsilon_{Si}}{q}\frac{N_A+N_D}{N_AN_D}\psi_{bi}} \tag{1.2.17}$$

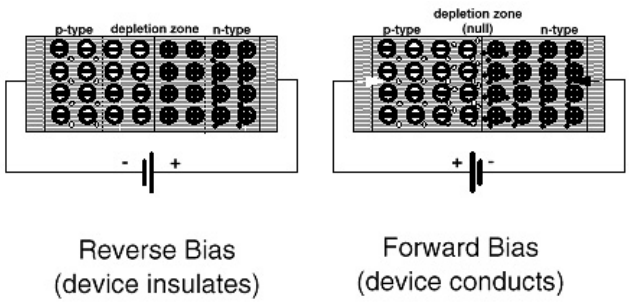

Figure 1.11: Effect on the depletion voltage of reverse and forward biasing.

In case of an abrupt junction (p^+-n or n^+-p where the + apex indicates a high concentration doping[3] are also used), the depletion region is expanded in the less doped side and the potential can be reduced to

$$W_D = \sqrt{\frac{2\varepsilon_0 \varepsilon_{Si} \psi_{bi}}{qN}} \tag{1.2.18}$$

where N is N_D or N_A depending on whether $N_A \gg N_D$ or vice versa.

n-p junctions are also the basis for photoelectric cells, because in the depletion region the electron-hole pairs generated by photons do not recombine thanks to the electric field described above, and holes and electrons can drift towards the opposite sides and can be collected.

In the case of a particle detector, the built-in potential is not sufficient to provide a good enough collection efficiency of the produced charges, and therefore an external potential must be applied. Applying a potential of the same sign of the built-in potential (reverse bias), it is possible to increase the depletion width and so the region in which a particle can be measured. In particular, for a bias much larger that the built-in one, the width of the region which is empty of free charges is proportional to the root square of the bias potential V_R applied:

$$W_D = \sqrt{\frac{2\varepsilon_0 \varepsilon_{Si}}{q} \frac{N_A + N_D}{N_A N_D} (\psi_{bi} + V_R)} \sim \sqrt{\frac{2\varepsilon_0 \varepsilon_{Si}}{q} \frac{N_A + N_D}{N_A N_D} V_R} \tag{1.2.19}$$

On the other hand, applying a potential of the opposite sign of the built-in one (forward bias), the depletion region reduces and a current starts flowing between the two doped sides of the junction. Figure 1.11 shows the effect on the depletion region of applying a reverse or a forward bias.

[3]For very high concentrations p^{++} or n^{++}

The current vs bias voltage characteristic is an exponential in the forward bias region and almost constant in the reverse one (fig. 1.12):

$$I_D = I_S \left(e^{\frac{V_D}{kT}} - 1 \right) \tag{1.2.20}$$

Applying a large reverse bias voltage, breakdown occurs and a huge current flows through the junction. The current which flows in a silicon sensor when a reverse bias is applied is called leakage current. The measurement of its value as a function of the reverse applied bias voltage is fundamental for the characterization of silicon sensors.

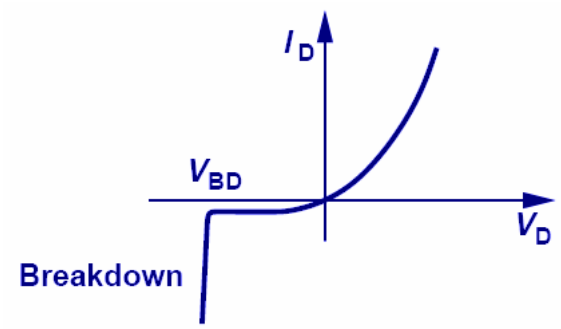

Figure 1.12: I-V characteristic curve.

1.3 Silicon detectors

In principle a silicon detector works as a ionization chamber. The huge advantage in comparison with traditional gas chambers is that the mean energy required to create an electron-hole pair (3.6 eV) is much smaller than the one to ionize a gas molecule (approximately 30 eV), so that it is possible to realize really thin detectors with a large signal response.

The *n-p* junction is connected to the readout electronics with two highly doped electrodes that allow to collect the charge produced in the depleted region. As already said, the region empty of free charge produced by the junction is not sufficient for particle detection. For this reason, one of the two electrodes is used to apply the reverse bias required. Usually, the signal is read out from the opposite electrode. Figure 1.13 shows these connections.

From eq. 1.2.19 it is possible to derive that the potential required to fully deplete the sensor depends, in first approximation, on the square of the sensor thickness:

$$V_{depl} = \frac{eNd^2}{2\varepsilon_{Si}} \tag{1.3.1}$$

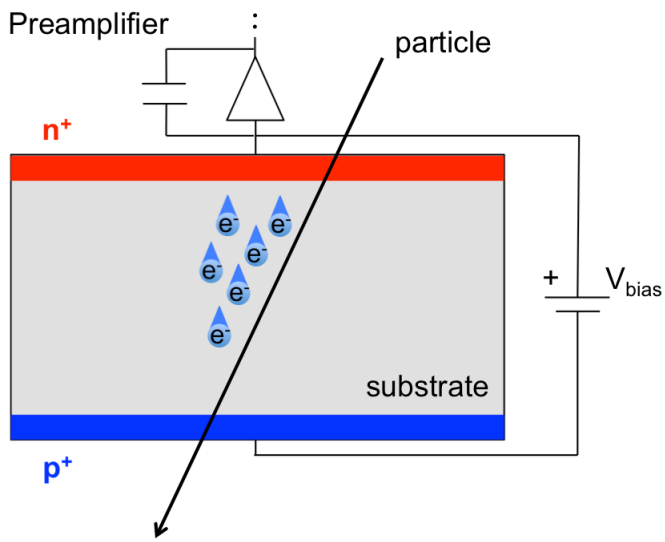

Figure 1.13: Sketch of a silicon detector.

The depleted region, being empty of free charge, can be considered as an isolator, which forms a capacitor with the two electrodes on both sides. Since the capacitance depends on the width of the depleted region, it is a function of the bias voltage:

$$C(V_{bias}) = \begin{cases} \sqrt{q\varepsilon_{Si}\frac{N}{V_{bias}}}, & \text{for } V_{bias} < V_{depl} \\ \frac{\varepsilon_{Si}}{d}, & \text{for } V_{bias} > V_{depl} \end{cases} \tag{1.3.2}$$

Therefore, increasing the bias voltage, the capacitance is reduced and, as better explained in sec. 1.3.1, the signal to noise ratio (SNR) increases.

Actually, this is only an approximation. Silicon detectors have usually segmented electrodes, in forms of strips or pixels, and the capacitance between nearby electrodes must be taken into account due to its important contribution. This capacitive coupling produces the so-called cross talk, which happens when the charge deposit in one pixel or strip induces a signal in the nearby electrodes.

1.3.1 Noise

Noise is made of different contributions, which are summed quadratically. The overall noise can be written as

$$ENC = \sqrt{ENC_C^2 + ENC_I^2 + ENC_{Rp}^2 + ENC_{Rs}^2} \tag{1.3.3}$$

ENC stands for Equivalent Noise Charge, which is the noise expressed in terms of electrons. The different contributions are related to

- Leakage current (ENC_I)
- Sensor capacitance (ENC_C)
- Sensor parallel resistor (ENC_{Rp})
- Sensor serial resistor (ENC_{Rs})

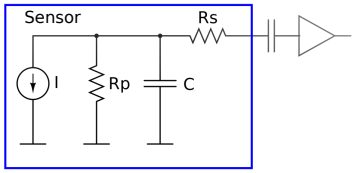

Figure 1.14: Sensor noise contributions.

The most important contribution to noise comes from the sensor capacitance. In particular, there is a linear correlation [6] between these quantities:

$$ENC_C = a + b \cdot C \tag{1.3.4}$$

a and b are related to the design of the amplifier and C is the sensor capacitance at the input of the amplification chain. A short integration time of the readout leads usually to larger a and b values.

Because of the noise, detectors need to have a threshold to distinguish the signal produced by a particle from thermal fluctuations. The threshold value must be high enough to cut the noise but at the same time as low as possible to avoid any efficiency loss.

1.3.2 Charge sharing

Silicon detectors are used in high energy physics thanks to the possibility of producing readout channels of the order of hundred microns, determining a very good spatial resolution.

The relevant parameter is the electrode pitch. To evaluate the resolution provided by a pitch length p, one supposes that the probability for a particle to cross the region between two nearby electrodes is constant. Evaluating the second momentum of this distribution, the resolution is determined to be $p/\sqrt{12}$.

This resolution is usually improved by the charge sharing effect. The threshold, which is externally set to trigger an event, is as low as possible, just enough to cut away the noise. The deposited charge can be shared and exceed the threshold in two or more adjacent electrodes. The group of electrodes which show a signal from the same particle is called cluster.

This is usually the case when the track passes in between two pixels as indicated with s in fig. 1.15(b). In this way, for a binary readout, the resolution is improved to $s/\sqrt{12}$ for a particle that leaves a signal in two readout channels and to $(p-s)/\sqrt{12}$ in case of only one pixel hit.

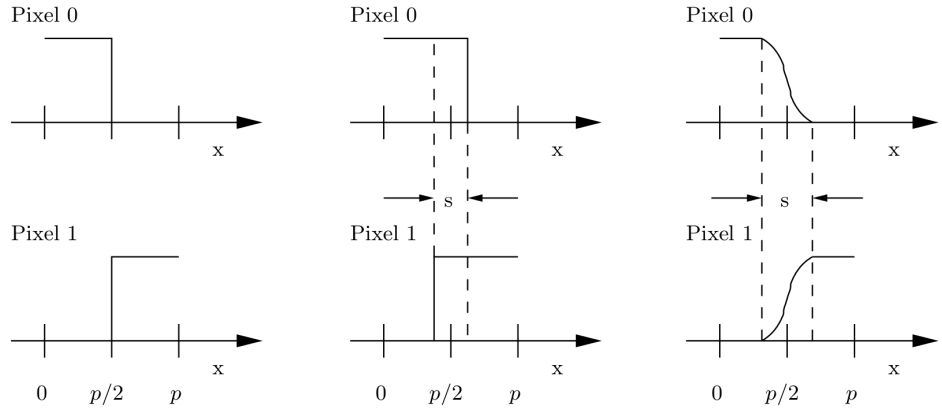

(a) Binary readout without charge sharing.

(b) Binary readout with charge sharing.

(c) Analog readout with charge sharing.

Figure 1.15: Signals in two adjacent pixels as a function of the impact position x.

The spatial resolution can be further improved with an analog readout or, more in general, a readout that provides information on the collected charge. With non-trivial algorithms it is possible to derive a better spatial resolution considering the ratio of signals in adjacent electrodes. However, in case of only one hit pixel the resolution remains the one of the binary readout case.

To increase the probability that more readout channels are triggered, detectors are usually tilted with respect to the particle direction or take advantage of the Lorentz angle[4]. As one can see in fig. 1.16, the effect of a magnetic field can increase or decrease the charge sharing, depending on the the track direction.

Sometimes also the reduction of charge sharing can be useful if the SNR does not guarantee a good detection efficiency of double hits.

1.3.3 Active area and guard rings

The sensor edge termination is a critical issue for the long term stability of a silicon detector. After some time the surface of the sensor always adjusts to the potential of the metal line close by. However, outside the sensitive region, the situation is more complex. In particular the edges of the sensor, due to the mechanical damages caused during the cutting process, are conductive.

[4]In the presence of an electromagnetic field a charge particle is deflected from its trajectory. In high energy experiment, where a magnetic field is often used, this effect must be taken into account.

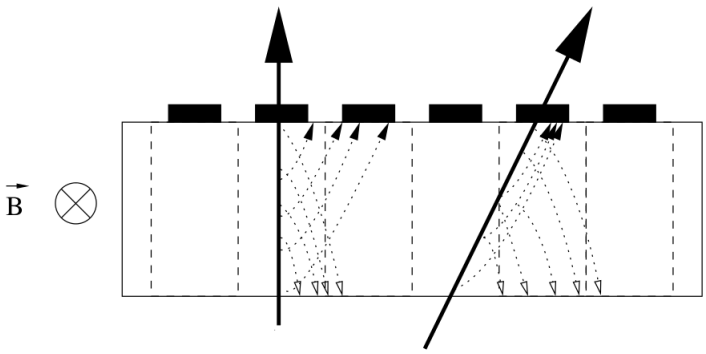

Figure 1.16: Charge sharing effects due to a magnetic field, for different track directions.

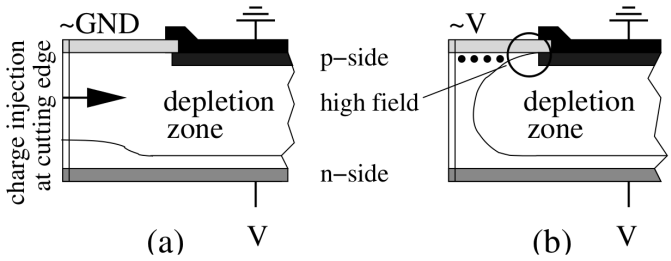

Figure 1.17: Two problematic situations at the sensor edges: (a) the depletion zone reaches the cutting edges and induces a large leakage current; (b) the electron accumulation layer produces a high electric field that leads to a low breakdown voltage.

Figure 1.17 shows two extreme cases that occur at the edges of the sensor. In the first case the ground is extended from the central region almost to the edges. This leads to a lateral extension of the depletion zone which produces a dramatical increase of the leakage current.

The second scenario happens when the surface potential adjusts to the backside potential. As a consequence, an accumulation layer of electrons is formed at the lateral end of the junction. Since this layer is conductive it adjusts to the backside potential and therefore the potential drops over a very short distance, producing a very high electric field and a low breakdown voltage.

The purpose of multiguard rings is to establish a smooth reduction of the electric field to avoid that it reaches the sensor edge. The guard rings bias themselves with the punch-through mechanism. This happens when the depletion region reaches a floating implant.

A typical layout of guard rings is shown in fig. 1.18, where it is visible

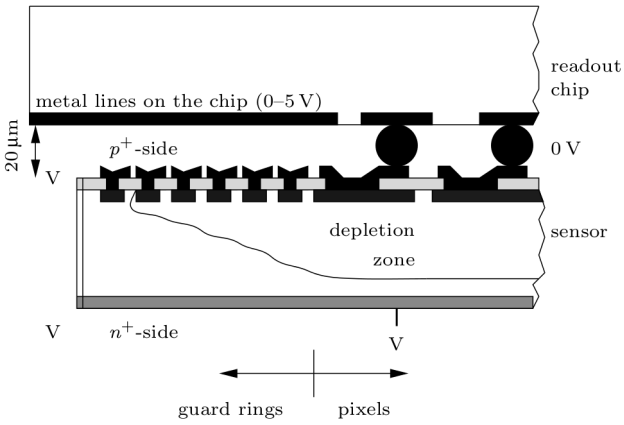

Figure 1.18: Depletion voltage under guard rings.

that the depletion region does not touch the edge. The importance of the technology developments to produce efficient guard rings is fundamental. In fact, the sensor region occupied by guard rings is an inactive area and therefore big efforts are devoted to reduce it as much as possible.

1.3.4 Radiation damage

Thanks to their high granularity, silicon detectors are used in the innermost layers of high energy experiments to provide the best spatial resolution possible. As a consequence, the fluence of radiation that they must tolerate is very high.

Radiation in silicon produces two main types of damage: bulk and surface defects. The former causes misplacement of silicon atoms in the lattice and it is relevant at high hadron fluences, the latter involves the increase of charge in the dielectric at the surface of the sensor. The damage produced by a particle depends on the energy and on the type of interaction. The energy must be sufficient to break the lattice configuration and determine the atom misplacement. For what concerns the type of interaction, a charged particle sees the silicon nucleus screened by an electron cloud, while neutrons interact only with the nucleus.

In order to have an independent measurement unit, radiation damage is scaled with the non-ionizing energy loss (NIEL), which represents the energy deposit of a particle which is not used for the reversible process of ionization[5].

[5]Ionization and excitation cannot be considered as radiation damages because they are processes fully reversible. NIEL is a quantity which describes the rate of energy loss due to the atomic displacements as a particle traverses a material.

Neutrons of 1 MeV are used as reference particles. In this way, the fluence Φ_{phys} of an arbitrary particle is converted into the electron equivalent fluence Φ_{eq} by means of the hardness factor k in accordance to [7].

The primary defects caused by irradiation are vacancies or interstitials which are not stable and can move in the lattice. Therefore, when two opposite defects meet each others an annealing process happens. However, also secondary defects can be formed, which are usually more stable and can create energy levels in the band gap. These levels are shown in fig. 1.19.

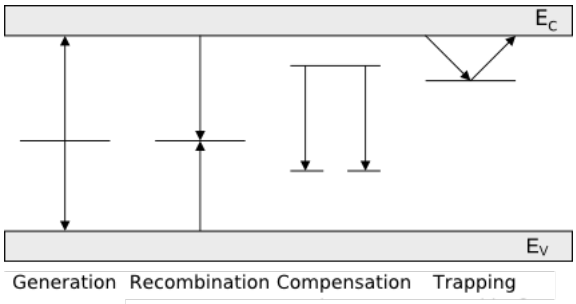

Figure 1.19: Energy levels in the gap produced by radiation damage.

The main effects of radiation damage are:

- Increase of the leakage current.
- Change of the space charge in the depleted region and subsequent increase of the full depletion voltage.
- Charge trapping

Leakage current

The energy levels in the band gap caused by crystal defects act as generation-recombination centres. The most important observables of this type of damage are the increase of the leakage current, as shown in fig. 1.20 [8], and the decrease of the generation lifetime τ_g. The leakage current can be related to the volume current I_{Vol}, which increases with the radiation fluence Φ:

$$\frac{I_{Vol}}{V} = \frac{I_{Vol,\Phi=0}}{V} + \alpha\Phi \tag{1.3.5}$$

where α is the current-related damage rate.

After irradiation, leakage current anneals with time. This process is strongly temperature dependent, due to the fact that the defects can move in the lattice and their speed depends on the temperature.

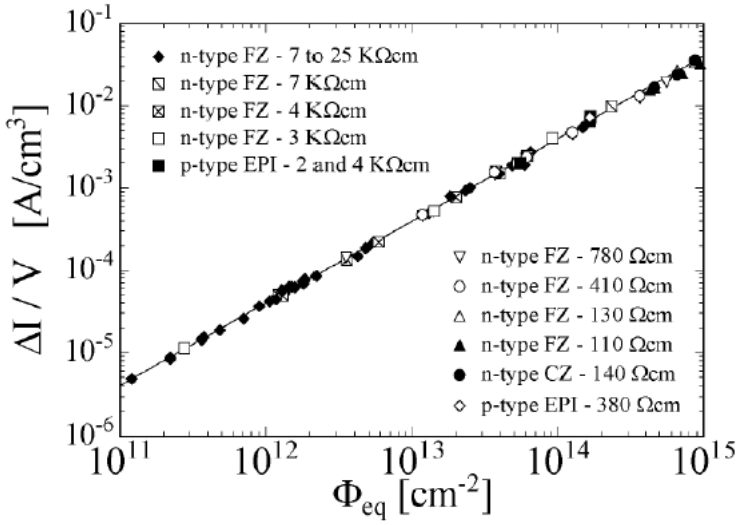

Figure 1.20: Induced leakage current for several detector materials as function of the fluence. Current has been measured after an annealing step at 60 ℃ for 80 min.

Effective doping

For an unirradiated sensor the doping concentration can be well approximated by the concentration of donors N_D or acceptors N_A assuming that one of them is so much dominant that all other contributions may be neglected.

For an irradiated silicon this is not correct any more. It is useful to define the effective doping N_{eff}, which represents the difference between all donor-like states and all acceptor-like states and can be determined from the full depletion voltage:

$$|N_{eff}| = \frac{2\varepsilon_0 \varepsilon_{Si} V_{depl}}{ed^2} \tag{1.3.6}$$

Figure 1.21 shows the effect of radiation on a sensor with a n-type bulk. It is visible that after a certain irradiation amount the type inversion occurs and this is due to the fact that radiation damage produces mainly acceptor-like states. Inversion does not occur in sensors with p-type bulk.

Trapping

An important effect of the creation of energy states in the band gap is the formation of traps, where electrons and holes can be stopped for a long time with respect to the signal collection time, causing a loss in the signal height.

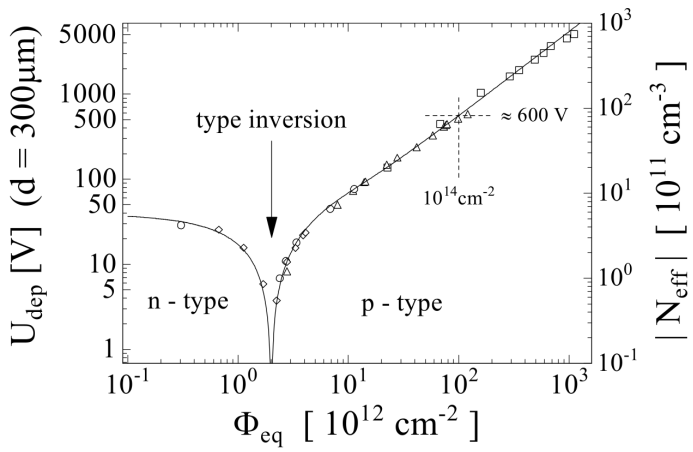

Figure 1.21: Change of full depletion voltage and absolute effective doping as a function of radiation damage in a 300 μm thick silicon sensor.

The dependence of this effect on the radiation fluence is expressed in terms of the trapping time τ_t:

$$\frac{1}{\tau_t} = \frac{1}{\tau_{t,\Phi=0}} + \gamma\Phi \tag{1.3.7}$$

where γ is a parameter which was measured to be $0.41 \cdot 10^{-6}$ cm^2/s for electrons and $0.60 \cdot 10^{-6}$ cm^2/s for holes after neutron irradiation [4].

For devices which do not need to stand a high fluence this effect is not so relevant. In fact, for a fluence of 10^{14} n$_{eq}$/cm^2 the signal for a 300 μm thick planar silicon sensor is still about 90% of the original one. However, for higher level of radiation, this effect becomes crucial: for a fluence of 10^{15} n$_{eq}$/cm^2 the signal decreases to $\sim$ 50%.

The effect of trapping acts as a free mean path: as larger the drift space as bigger the trapping probability.

Surface damage

In silicon the surface is a critical point for radiation damage. Silicon sensors are usually covered by a silicon oxide layer which provides the insulation. In this material, ionization is not a fully reversible process. Electrons in the SiO_2 have a high mobility ($\mu_{n,oxide} \sim 20$ cm^{2}V^{-1}s^{-1}) and will be collected by the nearest positive biased electrode. Holes, instead, have a very low mobility ($\mu_{p,oxide} \sim 2 \cdot 10^{-5}$ cm^{2}V^{-1}s^{-1}) because of the large number of shallow hole traps. When a hole in the oxide comes near the interface with the silicon where there are many deep hole traps, it may be stopped permanently.

The positive oxide charge influences the electric field in the silicon bulk close to the surface and induces a compensating electron accumulation layer in n-type silicon and a depletion layer in p-type silicon [4].

1.4 Diamonds

As already said, a big effort in R&D is made for building detectors able to tolerate very high radiation levels for future high energy experiments. Instead of silicon, diamond is investigated as an alternative solution [9].

1.4.1 Chemical vapor deposit

Diamond can be produced artificially via a **C**hemical **V**apor **D**eposition (CVD) [10]. The process starts from a substrate, usually of silicon or molybdenum. A gas mixture containing carbon, hydrogen and oxygen is ionized and under particular pressure and temperature conditions it is possible to deposit carbon in the form of graphite and diamond lattice [11]. Thanks to the other two gases, graphite is etched, while diamond is grown. The growth rate is typically about 1 $\mu\mathrm{m\,h}^{-1}$. After the process, the wafer is lapped to final thickness and laser cut. Finally, a metal is deposited for the ohmic contacts, allowing to create different electrode geometries. Materials used in this step are primarily chromium, because it forms a carbide with the diamond, followed by a gold layer to prevent oxidation.

1.4.2 Characteristics

A CVD diamond sensor is characterized by the charge collection distance (d_c), defined as the distance that holes and electrons drift apart in an electric field. This value takes into account the drift values (μ^+ and μ^-) and lifetimes (τ^+ and τ^-) of both charges and the electric field (E_{eff}) applied to the sensible volume:

$$d_c = (\mu^+\tau^+ + \mu^-\tau^-)E_{eff}$$

Natural diamonds have $d_c \sim 30\ \mu$m. With a moderate irradiation fluence the charge collection distance, and hence the signal output, increases. This effect is due to trapping by non-diamond atoms in the bulk. These sites are typically located deep in the gap between the two bands of the semiconductor. The result is that, once traps are filled, they become inactive, providing an increase in response. This effect is called pumping. The process is fully reversible by irradiating the bulk with an UV light, which releases the particles in the traps taking back the diamond to unpumping state. Furthermore,

this process can be repeated without damaging the sensor. The pumping transition occurs for all types of particles at usually 10^{10} particles/cm^2.

Because of the large band gap ($\sim$ 5.5 eV), diamonds are good isolators with a very high breakdown voltage, allowing to apply high electric fields with low leakage currents.

Another interesting feature is the charge collection speed. The mobility of holes and electrons is 1800 and 1200 cm^{2}V^{-1}s^{-1}, respectively, faster than in silicon, where is 1400 and 450 cm^{2}V^{-1}s^{-1}. Therefore a diamond detector of few hundred microns thickness can collect all charges in $\sim$ 1 ns.

Other two aspects are interesting. The low dielectric constant (5.7 compared to 11.9 of silicon) makes possible to reduce the sensor capacitance thus reducing the noise. Moreover the good thermal conductivity, five times higher than copper, provides easier handling of thermal load than for other materials,

Finally, the most promising feature is the radiation hardness. Thanks to the very large band gap, the increase of leakage current in diamond due to new energy levels created by the defects in the gap is negligible and because of the strong inter-atoms bounding the lattice damage in diamond is less frequent than in silicon.

While for the aforementioned characteristics the large band gap is a positive feature, on the other hand it causes a much lower charge production in comparison to silicon, making more difficult the readout. As an example, for a 300 μm silicon 24000 e-h pairs are expected, while for a diamond of the same thickness less than 11000.

Chapter 2

Silicon pixel detectors

In this chapter the two main types of silicon pixel detectors, monolithic and hybrid, are presented. Within the hybrid class, this thesis concentrates on the advanced technology of 3D sensors. These devices are currently being considered for the upgrades of the experiments ATLAS and CMS at the Large Hadron Collider (LHC). The ATLAS 3D Collaboration has shown that these detectors accomplish the strict requirements, in terms of radiation hardness, for the inner layers of the pixel tracking detectors. In particular, 3D sensors produced by the Fondazione Bruno Kessler (FBK - Trento, Italy) for CMS are described in detail, together with the readout chip bump-bonded to them. These detectors are the subject of this thesis and their characterization will be presented in the following chapters.

2.1 From strip to pixel silicon detectors

The aim of tracking detectors in high energy experiments is to provide precise information on the trajectory of particles, from which, often with the presence of a magnetic field, particle characteristics can be derived, like sign and momentum, and the event vertex can be reconstructed. Because of their high granularity, silicon detectors are often used, with different performance depending on the technology. In fig. 2.1 single-sided strip (a), double-sided strip (b) and pixel detectors (c) are shown.

The first configuration is obtained with a thin parallel segmentation of one of the two electrodes. Using an independent readout channel for each strip, a one-dimensional position information is obtained. This type of detector is quite simple to produce, but for measuring both the x and y coordinates two of them are required.

A possible solution to get both measurements with only one device is

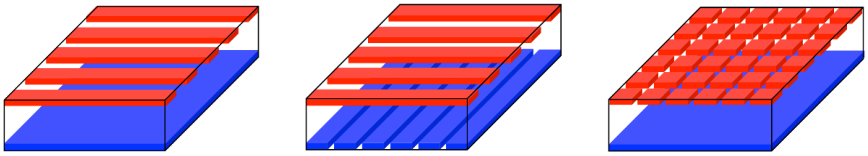

(a) (b) (c)

Figure 2.1: Main families of tracking detectors: (a) single-sided strip, (b) double-sided strip and (c) pixel detectors.

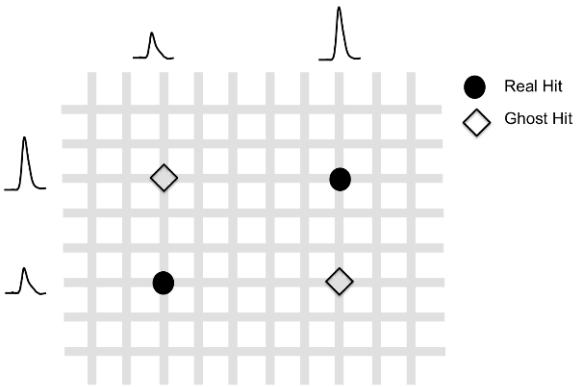

Figure 2.2: Ambiguity problem for a two particles event in a double-sided strip detector.

a double-sided strip detector (fig. 2.1(b)). In this case the two electrodes are segmented so that the directions of the strips on the opposite sides are perpendicular. However, this technique presents an ambiguity problem if more than one particle hit the detector at the same time. What happens is clearly shown in fig. 2.2. For a two particles event, the collected charge can be associated to four different points on the surface of the detector. In general, for n simultaneous hits, n^2 points will be reconstructed of which $n!$ are not real (*ghost* hits).

A solution to this problem, without increasing the number of detector layers, is to use pixel detectors. The device shown in fig. 2.1(c) is a planar pixel sensor, that will be discussed in sec. 2.3.1. The novel technology of3D pixel detectors will then be presented in detail from sec. 2.6.

2.2 Readout layouts

Because of the small area of each electrode, pixel detectors present lots of benefits in comparison to other architectures. Besides providing a more precise spatial information, the fine segmentation allows to have a lower leakage current, a better signal over noise ratio and reduced hit rate. The drawback is a more complex readout electronics.

The solution often adopted when the event rate is not very high is that of charge-coupled devices (CCD). These structures collect signals from all pixels of the sensor and send them one by one to a device for amplification and analysis [12]. Because of the way data are handled, CCDs are slow and this type of readout is only useful in case of a low event rate, like in digital cameras or in medical applications.

In high energy experiments, characterised by very high event rates, each pixel is connected to a readout channel. The two most common solutions (fig. 2.3) are: hybrid pixel detectors (sec 2.3), where the signal collected in a sensitive volume is elaborated by a separate readout chip, and monolithic detectors (sec 2.4), in which sensor and electronics are integrated.

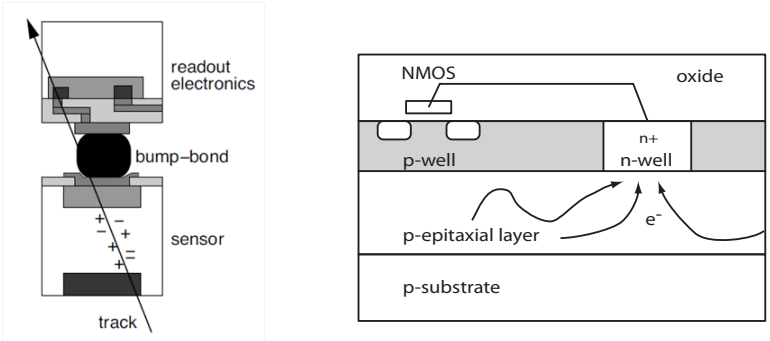

(a) Hibrid pixel (b) Monolithic pixel

Figure 2.3: The two principal families of pixel detectors.

2.3 Hybrid pixel detectors

The vertex detectors of the LHC experiments use hybrid pixel detectors. Ionizing particles create charges in the sensor that are collected and sent to the readout chip, which amplifies, filters and temporarily stores the signal until it is transferred to the periphery data buffer, where it waits for the trigger. The technique to link sensor and readout chip is called bump-bonding.

2.3.1 Planar pixel sensor

The simplest planar pixel geometry uses a p^+ pixel implant on a n-type substrate, which has usually a thickness between 200 and 300 μm. Electrodes are implemented on the frontside of the silicon bulk. The backside houses the ohmic contact, which is obtained with an overall n^+ implant and an aluminization. This configuration, called single-sided, is simple to realize because it is not necessary a photolithographic step[1] on the backside.

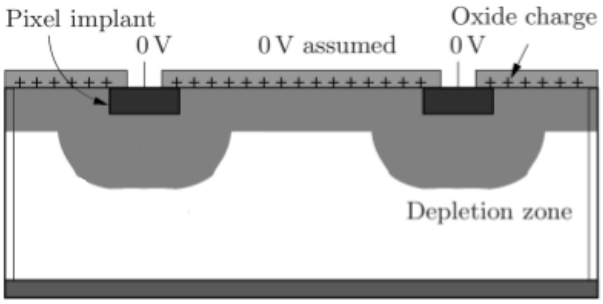

Figure 2.4: Schematic cross section of a simple silicon pad sensor.

Applying a positive bias on the backside, the depletion zone starts to grown from the junction into the bulk, until the bulk is completely depleted. In this type of sensors the charge deposited by a crossing particle drifts perpendicularly to the silicon surfaces, holes to the frontside, where are collected by the pixel electrodes and electrons to the backside.

In principle there are two choices for the substrate doping and two choices for the doped electrodes. Four combinations are thus possible and they are listed in table 2.1.

The size of the collecting electrodes is an important parameter to tune the signal characteristics. In fact, the segmentation decides the volume within which the generated charge is collected by an electrode: reducing the pixel area, also the pulse height of the signal reduces.

Other signal characteristics are determined by the bulk thickness. Increasing the thickness, the time needed to collect all the deposited charge becomes higher. Furthermore, in a thicker bulk the probability of charge trapping increases, which is a problem for irradiated sensors. For these reasons, thin sensors are preferred, compatibly with the noise requirements[2].

[1]The photolithographic step uses a photoresistive film (called photoresist or simply resist) which can be selectively removed exposing the material to light and leaving in shadow zones that must be protected.

[2]A thinner sensor has higher capacitance which means higher noise (sec. 1.3.1)

Readout electrode	Substrate	
	p-type	n-type
p^+	Double-sided process (expensive). No advantage over p^+-in-n	Typical single-sided sensor for most of the applications
n^+	Single-sided process. May be a replacement of n^+-in-n in future	Double-sided process. "Standard-device" if radiation hardness is required

Table 2.1: All possible combinations of substrate and electrode types.

2.3.2 Readout electronics

One of the biggest challenges of producing a pixel detector is to build a readout chip suited for arranging thousand of channels. Usually the chip architecture can be divided in three main areas: the pixel unit cell (PUC), the column periphery and the chip periphery. A sketch of this structure is shown in fig. 2.5.

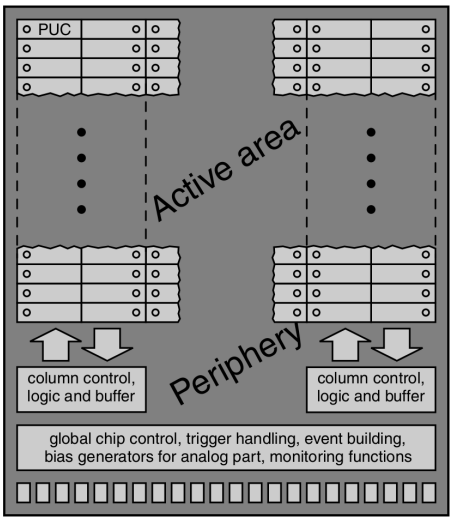

Figure 2.5: Sketch of a tipical readout chip.

The most important constrain for a readout chip is the density of transistors per unit area. This is fixed by the technology used, defined by the

minimum gate length achievable. As a consequence, the PUC dimensions are determined by the number of devices which need to be integrated.

In the PUC there are the amplification circuits, usually made of a one or two stages amplifier, a comparator for the threshold and a storage where the data are saved waiting to be read out by the column periphery. For the calibration procedure, in the PUC a circuit is usually present that allows to inject charge directly to the amplifier chain instead of through the sensor.

Pixels are normally arranged in columns or column pairs. In this way signals only pass through the column periphery at the bottom of the chip, and therefore no electronics on the sides or above the chip is required. In the column periphery signals wait for a valid trigger and then pass to the chip periphery, from which are sent to the Data AcQuisition (DAQ) chain.

The chip periphery contains the Digital to Analog Converters (DACs) used for setting the global parameters of the chip. This is the interface between the chip and the external readout chain to which the chip is connected via wire-bonding.

To reduce the insensitive area and the number of readout channels for the data acquisition, pixel detectors are often arranged in modules. In this way the information is merged serially and then sent to the data acquisition for further processing and storage.

2.3.3 Bump-bonding techniques

The bump-bonding process is a technique extensively used in the electronics industry for the connection of integrate circuit dies to printed circuit boards or other substrates. The bump-bonding techniques, which have been proven to work at the contact density required for particle physics, use either electroplated solder bumps or indium bumps deposited by evaporation.

The bump-bonding deposit is usually made on the wafer before cutting the single dies, except for the gold-stud bump-bonding, where the process can be made on single chip.

Solder bump-bonding

On the metal contacts of the chip the under bump metallization (UBM), made of layers of different metals, is deposited to favour the adhesion with the bump. Then a photolitographic step allows to selectively deposit the metal for bumps. The metal used in this case is a eutectic solder[3] (35Pb/Sn).

[3]An eutectic material is a mixture of two chemical elements, that solidifies at a lower temperature than any other composition made up of the same elements.

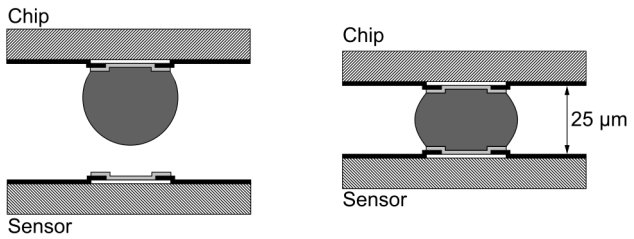

Figure 2.6: Flip chip process for the solder bump-bonding.

Because of the low Sn vapour pressure, the eutectic solder can be hardly evaporated. Therefore the 35Pb/Sn deposit is made through electroplating. This type of process produces cylinders that are turned in spheres of 25 μm diameter thanks to the reflow process. During this process, made approximately at the temperature of 350 ℃, the bump undergoes a collapse to a truncated sphere shape.

After applying the bumps on the chip, the UBM is also deposited on the sensor pads, and then the flip chip can be made. The chip bumps are tacked to the UBMs of the sensor by solder flux, as shown in fig. 2.6. After a reflow process chip and sensor self-align thanks to the superficial tension of the bumps. This type of process produces a connection between chip and sensor of $\sim 1\,\Omega$ impedance.

Indium bump-bonding

The indium bump-bonding process was developed for applications which require good mechanical and electrical properties also at low temperature, approximately the one of liquid nitrogen. Typically the indium deposit is grown with the evaporation technique. The result is a bump with a maximum height of 10 μm [4].

The same process must be applied both on the chip and on the sensor, as shown in fig. 2.7. In this case the flip chip can be performed at room temperature, but the best result is obtained at a temperature of approximately 100 ℃.

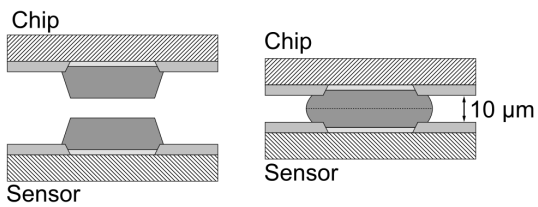

Figure 2.7: Flip chip of an indium deposited sensor.

This process produces a connection with $\sim 10\,\Omega$ impedance and a distance between chip and sensor of approximately 10 μm. Actually, due to its properties, indium oxidises easily and this effect must be taken into account during the production.

There is also another technique to produce an indium deposit, similar to the solder bump-bonding described previously. However, this technique requires a two masks process, one for the sputtering of the base and the other for the indium deposit. The reflow process arranges the indium in a sphere. In this case it is also required a thin deposit of indium on the sensor contacts.

Gold-stud bump-bonding

Among the materials that can be used for bump-bonding, gold offers two important characteristics: it does not oxidise and it deforms easily allowing a good electrical contact. Gold can be applied by electroplating or, more interesting for pixel application, placed through stud bonding. This technique is a variation of the traditional ultrasonic wire-bonding.

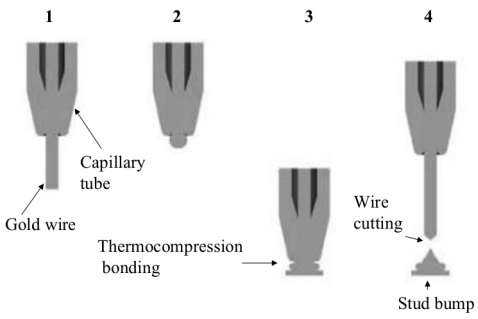

Figure 2.8: Au-stud bump formation process: a gold wire passes through a capillary tube (1), is heated (2), and pressed against the bonding pad (3). The wire is then pulled away and is cut close to the stud bump (4).

The wire is intentionally broken after the thermocompression bonding to the die pad and a coining process is used to make the bump more planar, as shown in fig. 2.8. The bumps are applied one after the other. This type of process is used when the devices are not available on a wafer scale.

2.4 Monolithic pixel detectors

The idea of this architecture is to join sensible volume and readout electronics in the same entity. The charge produced by the ionizing particle is

collected by a diode connected to a gate of a transistor. The cross section and the schematic of the device are shown in figs. 2.9(a) and 2.9(b), respectively.

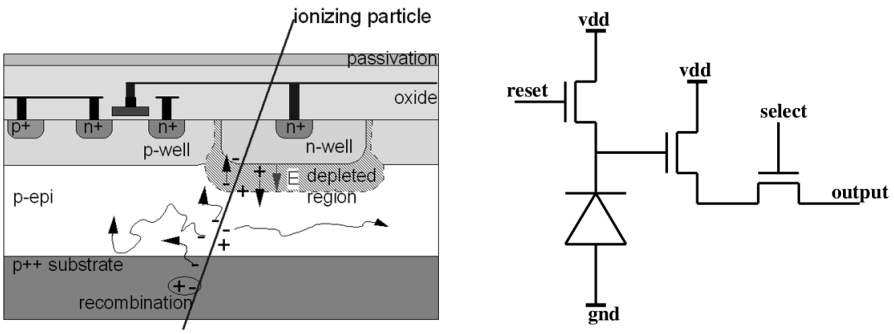

(a) (b)

Figure 2.9: Monolithic detector: (a) cross section and (b) equivalent circuit of a pixel.

The electrons produced by the particle passage are collected by a n-well diode. The depletion area is shallow and the resulting charge collection is poor. The solution to this problem is to make the diode junction with a p-type epitaxial layer (MAPS-epi pixels). Since this structure has a doping which is three orders of magnitude smaller that the p^{++} substrate, a potential barrier is created between the two layers which acts like a mirror [13], so that the electrons created in the epitaxial layer thermally diffuse towards the collecting diode, as shown in fig. 2.9(a). The signal is then sent to a transistor gate (fig. 2.9(b)) where it waits to be selected from the logics.

An interesting advantage of this technique is that it makes possible to produce pixels much smaller than the ones which can be obtained with the hybrid technology. Pair production occurs in the entire sensor but only in the epitaxial layer it is not subject to recombination. Based on its thickness (usually $12 - 16$ μm) about 1000 e^- are expected for a MIP, which means that a low noise readout is the challenge of these devices.

To increase the charge production, the MAPS-SoI pixel detector has been proposed [14]. The idea is to isolate a high resistive bulk from the CMOS layer with a SiO_2 deposit, making use of the silicon on insulator (SoI) technique (fig. 2.10(a)). In this way the result of joining the readout to a sensitive volume with large charge collection can be reached.

The problem of the SoI detector is the backgate-effect (fig. 2.10(b)). In fact a new gate controlled by a high voltage (HV) is created which shifts the transistors threshold of more than 100 mV, which is not tolerable by the

CMOS[4] technology.

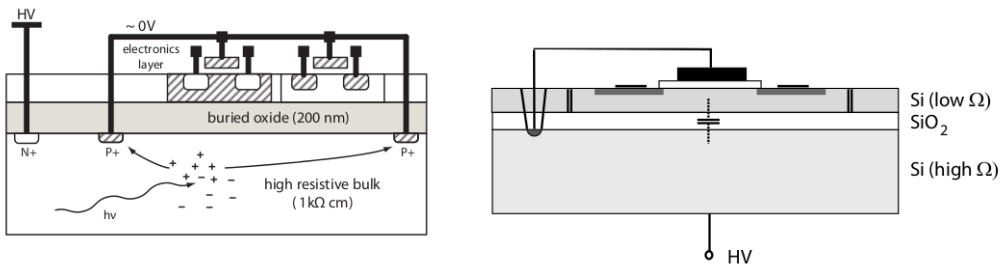

(a) (b)

Figure 2.10: (a) Structure of MAPS-SoI and (b) simplified schematic of the backgate-effect.

2.5 New requirements for high energy physics

Future high energy experiments at colliders will have to work with very high luminosities. For example, in the foreseen upgrade of the Large Hadron Collider (HL-LHC) this parameter will reach 10^{35} cm^{-2}s^{-1}, which corresponds to an equivalent hadron fluence up to 10^{16} n_{eq}/cm^2 in the innermost layer of the tracker detector [15]. For this reason ATLAS and CMS have started a strong R&D program to develop pixel detectors which can operate up to a fluence of $\sim 10^{16}$ n_{eq}/cm^2.

Another important issue for the next pixel detectors is the active area. In fact, the guard ring zone of the current sensors, which is described in sec. 1.3.3, is not a sensible area for particle detection. Therefore detectors must be overlapped to cover the complete solid angle. The possibility to reduce or eliminate the guard ring area would allow to solve this spatial occupancy problem.

The reduction of this insensitive region is a fundamental requirement of the High Precision Spectrometer project (HPS) under approval for CMS. The idea is to install detectors approximately at 240 m from the CMS interaction point, in order to detect protons at very small angles. Reducing the insensitive edges allows to approach closer to the beam.

3D silicon pixel detectors can provide both the radiation hardness and the implementation of active edges.

[4]Complementary Metal-Oxide Semiconductor

2.6 3D pixel detectors

The structure of 3D pixel sensors was proposed in 1997 [16]. The electrodes penetrate through the silicon bulk perpendicularly to the surface. In this way the distance between opposite electrodes can be made smaller than in planar sensors. This determines the relevant properties of 3D sensors:

- because of the reduced depth of the region to be depleted, 3D detectors work consequently (eq. 1.3.1) with a voltage almost ten times less than for planar ones (between 10 and $30\,V$);
- since in 3D silicon sensors thickness and electrode distance are decoupled, the produced charges travel for a shorter drift distance providing a faster response with respect to planars, keeping at the same time a comparable signal since the amount of generated charge only depends on the substrate thickness, which is normally the same for planar and 3D sensors;
- because of the charges drifting for a short path, the radiation hardness is improved since the trapping probability is reduced (1.3.4).

Different 3D structures have been proposed [17], which can be classified based on the following features:

- the type of electrode: it can be a junction (p-n) or an ohmic contact (n^+-n or p^+-p);
- side of the silicon bulk from where the columns are etched;
- structure implemented on the backside in case columns do not pass completely through the substrate;
- depth of columns.
- number of readout columns per pixel (1E, 2E, ...), which determine the distance between electrodes.

The cross sections of different 3D sensors are presented in fig. 2.11.

The choice of the substrate doping is p^{--}-type, because such a bulk suffers the radiation damage less than n^{--} [18]. In particular, irradiation produces positive charges which do not determine type inversion in p substrates (sec. 1.3.4).

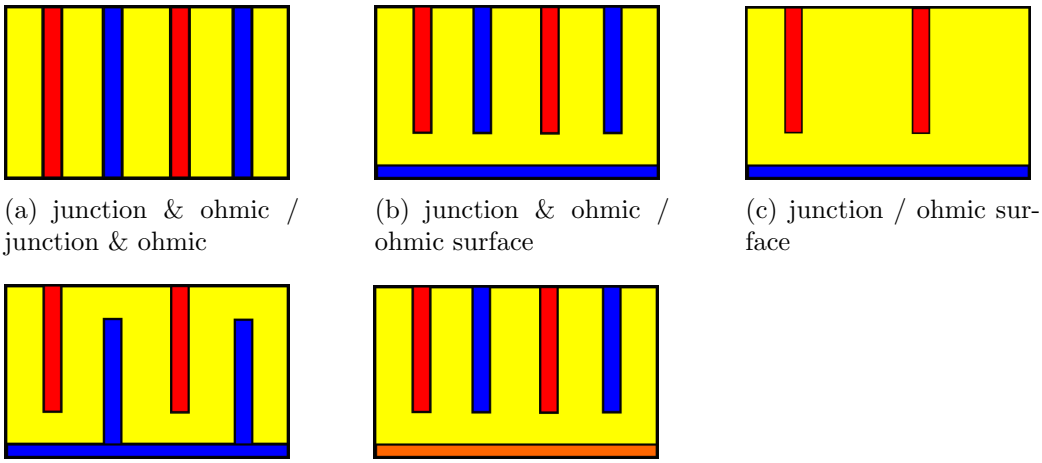

(a) junction & ohmic / junction & ohmic

(b) junction & ohmic / ohmic surface

(c) junction / ohmic surface

(d) junction / ohmic column and surface

(e) junction & ohmic / SiO_2 surface

Figure 2.11: Possible layouts of 3D pixel sensors. They can be classified according to the type of the two surface structures. Colours indicate the type of doping: yellow p^{--}, blue p^{+}, red n^{+}, orange SiO_2.

2.6.1 Fabrication process

The fabrication processes of 3D sensors vary depending on the different structures. The first 3D sensor was produced in 1999 [19] at Stanford Nanofabrication Facility.

Generally speaking, the fabrication of 3D sensors requires a much more complex procedure with respect to that for planar sensors. As an example, the fabrication process for the first 3Ds was made of 25 steps, of which the principal ones are shown in fig. 2.12:

(a) A support wafer is used to prevent possible breaking of the detector during the following steps where the temperature can reach 125 ℃ [19]. This step prevents the possibility to make a double-sided fabrication. After all fabrication steps are finished the support wafer can me removed[5].

(b) Windows for subsequent steps are etched in the silice (SiO_2). The etching of silice uses a photoresist film deposited on the surface, which is selectively illuminated making use of a mask. Part of the resist which is hit from light is removed, while the remaining part protects the chosen SiO_2 from the etching agent.

[5]This can seriously damage the detector wafer and for the first fabricated sensors, treated in this section, was not applied.

(c) 3D detectors need deep holes with small diameter. To obtain this an anisotropic etching is necessary, which is typically the Deep Reactive Ion Etching (DRIE). The anisotropy (A) is defined in terms of speed of vertical (V_r) and lateral (V_l) etching (eq. 2.6.1):

$$A = 1 - \frac{V_l}{V_r} \tag{2.6.1}$$

This value is an essential parameter and to produce 3Ds it must be close to one. The technique consists of two alternating steps [20]: reduce the spontaneous etching on the sidewalls and passivate them for controlling the etching direction. Repeating cycles of etching and passivation, deep holes can be produced.

(d) After etching, columns are empty and hence no charge can be deposited by a crossing particle. For reducing this drawback, columns can be filled with polysilicon. This process can be realised either after doping the electrodes or in two steps: partially before and partially after the doping.

(e) and (f) The procedure of etching, filling and doping is repeated for the other type of electrodes.

(g) At the end of the fabrication procedure, a metal deposition is applied for creating pads for bump-bonding.

2.6.2 Active and slim edges

A very interesting feature of 3D sensors is the possibility to implement active edges.

Sensors based on planar technology have an insensitive region near the edges due to various features:

- the field of the last electrode bulges near the edge and it is necessary to have a margin that prevents to reach it (fig. 2.13(b));
- chips or micro-cracks are sometimes near the edges (fig. 2.13(c));
- space must be allowed for the guard rings (fig. 2.13(a)).

For example, in the pixel sensor used in the ATLAS experiment at CERN this region occupies 14% of the surface area [21].

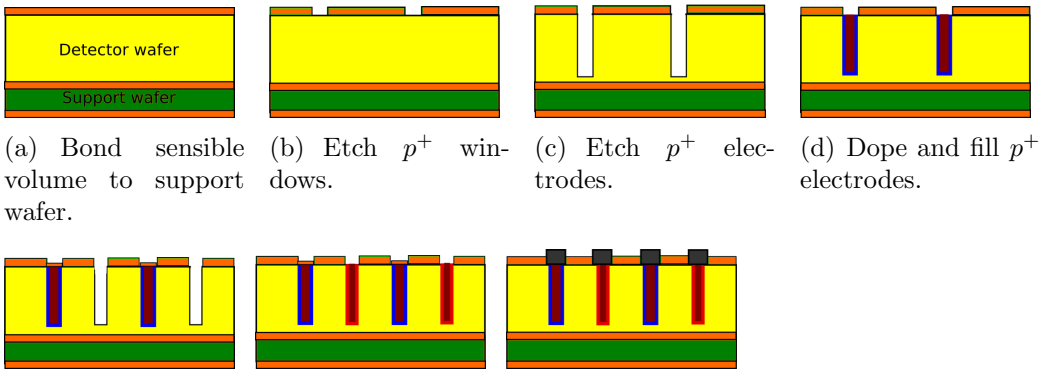

(a) Bond sensible volume to support wafer.

(b) Etch p^+ windows.

(c) Etch p^+ electrodes.

(d) Dope and fill p^+ electrodes.

(e) Etch n^+ windows and electrodes.

(f) Dope and fill n^+ electrodes.

(g) Deposit aluminium contacts.

Figure 2.12: Main production steps of the first 3D pixel detector. Colors represent: yellow p^{--}, orange SiO_2, red n^+, blue p^+, green support wafer, grey aluminium, brown polysilicon.

Because of this dead region, pixel detectors are usually overlapped to ensure the solid angle coverage, increasing the amount of material seen by the particles. To reduce it, active edges can be used. The main technique is to etch trenches around the margins of the device and then doping them either n or p-type. In this way, edges become electrodes themselves, ensuring the sensor to be active all across the surface (fig. 2.14). A consequence of this technique is that the sensor production must be single-sided due to the requirement of the support wafer.

An intermediate solution between active and standard edge is the slim edge (fig. 2.15). In this case a smooth reduction of the electric field is provided by a multiple fence of ohmic columns extending from the active area towards the scribe line. The result is an inactive region of $\sim$ 200 μm, significantly reduced in comparison to the $\sim$ 1 mm of the standard planar sensors with guard rings [22].

2.6.3 Evolution of 3D layout

A summary of the historical evolution of 3D sensors is proposed in fig. 2.16.

The first 3D sensor built in Stanford (USA) was characterised by full passing through columns (fig. 2.16(a)). This type of sensors is presently produced at SINTEF [23] thanks to a technology transfer.

Semi-3D detectors (fig. 2.16(b)) have been proposed and independently in 2004 by Fondazione Bruno Kessler (FBK) in Trento (Italy) [24] and VTT in Finland. The idea was to use only one doping type of column not full

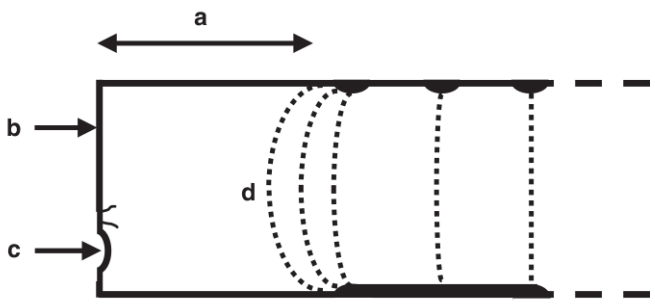

Figure 2.13: Schematic cross section of the edge of a planar pixel sensor: (a) space for guard and voltage-dropping rings, (b) the saw-cut edge are conductive and (c) often edges contains chips or micro-cracks. All these features produce a (d) bulging electric field in the depleted region.

passing through the wafer and an ohmic contact on the back plane. This architecture was tested with a Medipix2 readout chip and compared with a planar sensor [25]. The most important result, obtained with a laser beam, is that a uniform and highly efficient detector response could be achieved with a sufficient low energy threshold.

Other types of semi-3D detectors were proposed by the Bookhaven National Laboratory (BNL) (fig. 2.16(c) and (d)) [26]. These architectures have all the electrodes implemented on one surface, ensuring a simply single-sided process. Double-sided production was introduced independently by CNM (fig. 2.16(e)) and FBK (fig. 2.16(f)) and will be separately discussed below.

FBK production

FBK started fabricating **S**ingle-sided **S**ingle **T**ype **C**olumn (SSTC) sensors in 2004 [24]. As shown in fig. 2.16(b), these devices are realized with a surface implant of p^+ on the backside of a p-type bulk, and an etching of n^+ columns on the frontside.

These detectors presented a few problems: low field regions within the sensible volume, that affect the charge collection causing non uniform response; current signals with a fast peak (in the order of few ns) followed by a slow tail (several μm) due to the hole drifting.

To improve on these aspects the **D**ouble-sided **D**ouble **T**ype **C**olumn (DDTC) technology has been developed starting from 2007 [27]. Readout n^+ columns, with a diameter of $10 - 12$ μm, are etched in a p-type bulk of $200 - 230$ μm from the frontside, while the p^+ ohmic ones are etched from the backside.

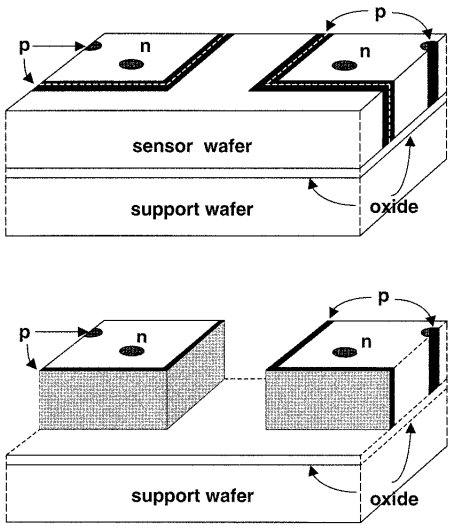

Figure 2.14: Schematic view of two adjacent active edge 3D sensors bounded to their support wafer. Top sketch: after holes and trenches are etched, doped and filled. Bottom sketch: after the larger dicing trench has been etched to separate the devices.

The technology has evolved from not-completely passing through columns to full passing through columns [28] (fig. 2.17), a feature implemented in the last FBK production for the ATLAS Insertable B-Layer (IBL) [29]. A cross section of a sensor produced with this technique is shown in fig. 2.17. Sensors from the latest FBK production also have slim edges of $\sim 200\ \mu$m.

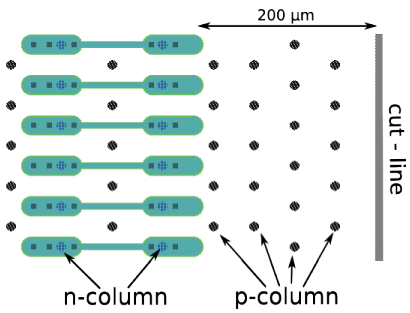

Figure 2.15: Top view of a slim edge solution for an ATLAS 3D silicon sensor.

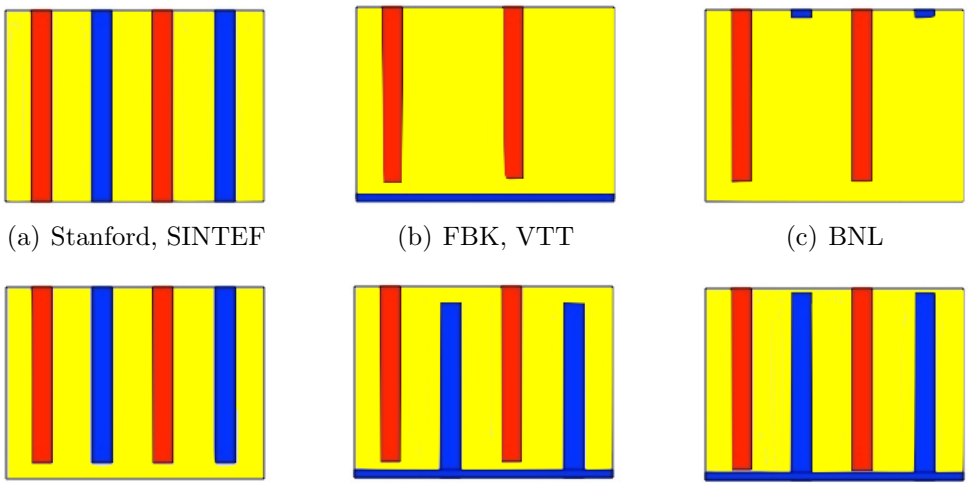

(a) Stanford, SINTEF (b) FBK, VTT (c) BNL

(d) BNL (e) CNM (f) FBK

Figure 2.16: Layouts of 3D sensor proposed by different research groups. Colours correspond to different doping: red n^+, blue p^+, grey p^{--} bulk.

CNM production

Independently of FBK, also the Centro Nacional de Microelectronica (CNM) in Barcelona developed a 3D DDTC sensor with not passing through columns [30], shown in fig. 2.18. The main differences with respect to FBK sensors are the holes partially filled with polysilicon and the bias columns connected together with a polysilicon plus metal layer instead of a p^+ doping implant. To prevent an early breakdown, p-stop implants are inserted under the oxide on the surface around the base of the n^+ columns.

The latest production for the ATLAS IBL implements slim edges of $\sim 200\ \mu$m [31].

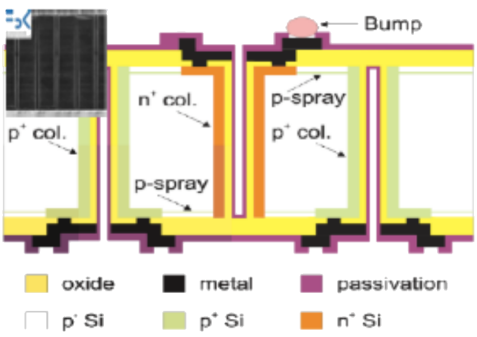

Figure 2.17: Cross section of a full 3D DDTC produced at FBK.

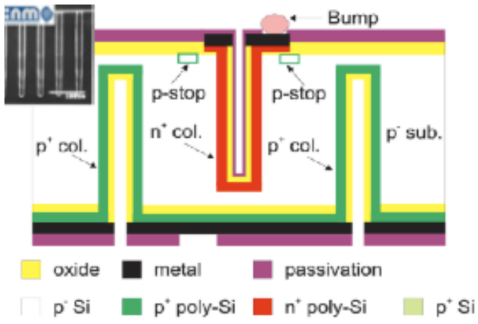

Figure 2.18: Cross section of a DDTC produced at CNM.

Both CNM and FBK developed a procedure which allows to connect together pixels in strips by means of a metal deposit. The metal layer is then removed after the measurements.

2.7 3D detectors for the ATLAS IBL

For the ATLAS experiment upgrade that is presently taking place a fourth layer of pixel detectors, the Insertable B-Layer (IBL)[29], will be added to improve primary and secondary vertex reconstruction. Thanks to the reduction of the beam pipe diameter a radial free space of 12.5 cm will host the IBL detector, which has a radius of 3 cm.

After several years of R&D studies, the ATLAS 3D Collaboration has been able to qualify 3D silicon pixel detectors for being installed in the forward part of the IBL. This is the first time that 3D detectors are used in a high energy experiment.

The IBL will consist of 75% of planar detectors and 25% of 3D detectors, of which half from CNM and half from FBK. Both technologies fulfill the IBL requirement of a hit efficiency in the active area greater then 97% after irradiation to fluences of $5 \cdot 10^{15}$ n_{eq}/cm^2.

A section of the IBL is partially shown in fig. 2.19. The layer is formed by 14 tilted and overlapped staves to guarantee the complete solid angle coverage, in the presence of sensors with slim edges.

Detectors are supported by a low density carbon foam, that also provides a small size pipe for the CO_2 evaporating cooling and aluminium conductors for the electrical power service.

Sensors for IBL are bump-bonded to the frontend readout chip FE-I4

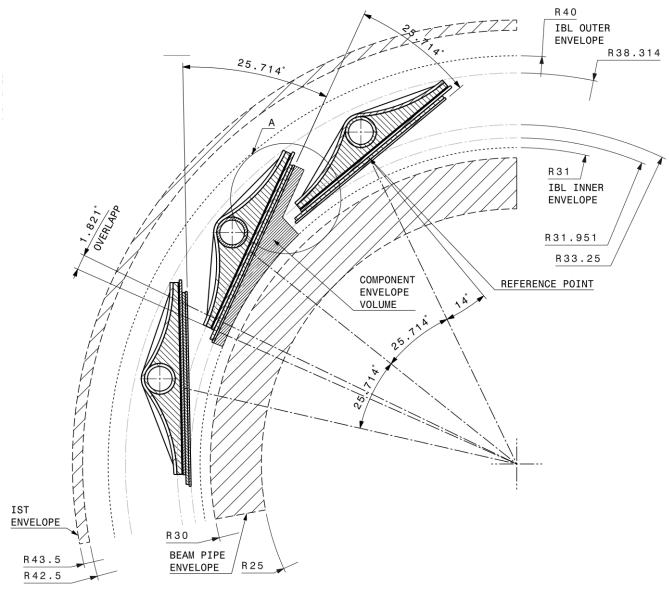

Figure 2.19: Section for the IBL layout.

[32]. The chip, realized with the 130 nm technology, is made of 2880 cells of 50×250 μm^2 arranged in a 80×336 matrix.

The ATLAS pixel detector uses a digital readout, which provides information on the digitized amplitude of the signal expressed in terms of Time over Threshold (ToT), which is the time measurement of the signal length above the discriminator threshold. From this information, and thanks to the calibration, it is possible to derive the charge deposited by the particle.

The FE-I4 chip is designed to stand the foreseen luminosity of the LHC upgrades and replaces the previous FE-I3 readout chip [33], which was realized with the $0.25\,\mu m$ technology and whose pixels had an area of 50×450 μm^2. Simulations performed at high luminosity [34] for the old FE-I3 show an unacceptable high number of signals lost due to pile up in pixel and congestion in the double column data bus. The FE-I4 pixel area, besides improving the spatial resolution, allows to reduce the occupancy and hence the lost hits.

The first 3D sensors tested by ATLAS were adapted to the pixel size of the FE-I3. 3D sensors were produced with two (2E), three (3E) or four (4E) readout columns per pixel, as shown in fig. 2.20.

For the IBL project it was finally chosen the so-called "2E-250" configuration, adapted for the FE-I4 chip [29]. This configuration corresponds to the 3E for the FE-I3 readout chip. It has an inter-electrode distance of

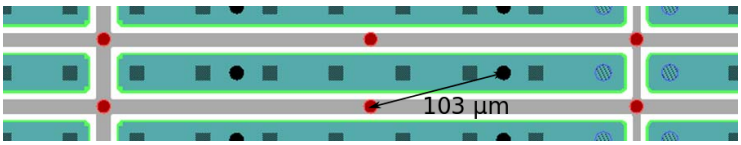

(a) 2E

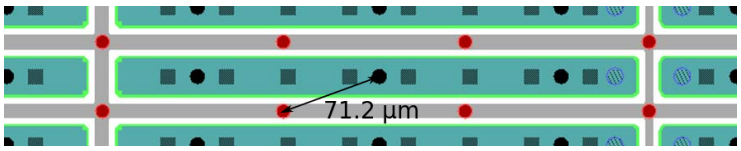

(b) 3E

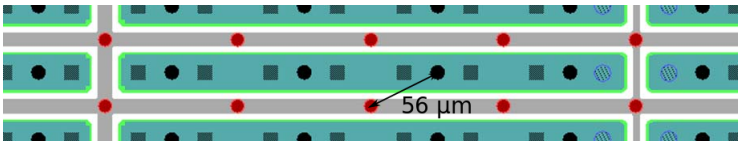

(c) 4E

Figure 2.20: Layout of ATLAS 3D sensors with different column configurations created for the front-end chip FE-I3.

~ 70 μm and, considering the IBL radiation dose level, it is a good compromise between signal efficiency (charge collection) and capacitive noise, which increases with the number of electrodes per pixel.

The depletion voltage for the IBL 3D sensors is $\sim 5 - 10$ V and the breakdown voltage is required to be greater than 25 V. Measurements on sensors produced by FBK show a breakdown above 50 V while the CNM ones are above 100 V. The noise level is ~ 150 e$^-$. 3Ds from FBK and CNM have been irradiated to fluences close to the IBL target of $5 \cdot 10^{15}$ n$_{eq}$/cm^2. For these devices, the optimal voltage setting of 160 V ensures high charge collection efficiency while maintaining the noise level low.

For studying hit efficiency and spatial resolution, testbeams have been performed on unirradiated and irradiated 3D sensors, obtaining a map of the efficiency like the ones in fig. 2.21. The plot at the top shows an irradiated CNM sensor placed perpendicularly to the beam, the plot in the middle an irradiated CNM sensor tilted of 15° with respect to the beam and the one at the bottom an unirradiated FBK sensor perpendicular to the beam. In the first one the readout electrodes are not visible because the non passing through electrodes and the high bias voltage applied allow to efficiently collect the charge even in the electrode region. When tilting the sensor of 15° with respect to the beam, the column inefficiency vanishes. For the FBK at the bottom, both readout and ohmic columns are visible, since they are full

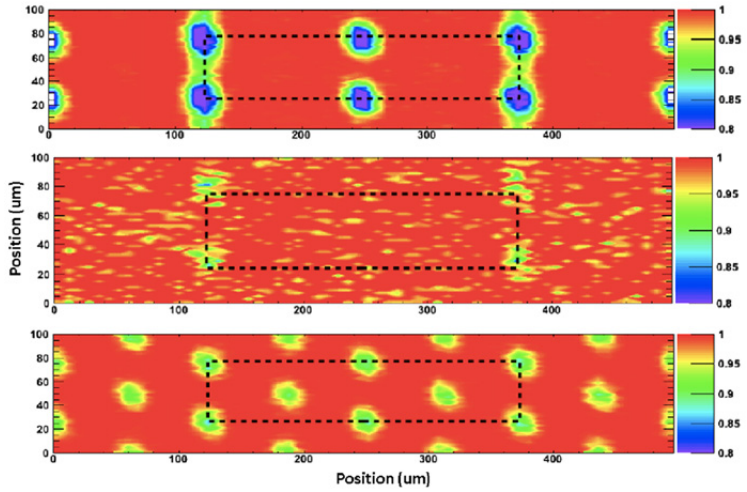

Figure 2.21: Hit efficiency pixel map for three 3D devices. The plot at the top shows the hit efficiency for perpendicular tracks for an irradiated CNM device operated at 160 V. The overall CNM efficiency is 96.5%. The middle plot shows the efficiency for an irradiated CNM device operated at 160 V. The track incidence is at 15° and the overall efficiency is 98.7%. The bottom plot shows the efficiency for an unirradiated FBK device operated at 20 V. For normal incidence tracks the efficiency is 98.8%. The passing through electrodes are clearly visible.

passing through. Irradiated 3D sensors, tilted of 15°, have a total efficiency higher than 97%, which is the requirement for IBL.

2.7.1 Radiation hardness

The radiation hardness is one of the most interesting characteristics of 3D sensors. As already said, the trapping probability is reduced by reducing the electrode distance, and as a consequence the drift path.

Studies have been performed by ATLAS on SINTEF 3D sensors, considering the various electrode configurations. The devices have been irradiated up to a fluence of $8.8 \cdot 10^{15} n_{eq}\, cm^{-2}$ and the signal collection studies have been carried out with an infrared laser [35].

The results are very interesting if compared with other standard devices used in tracking detectors, as shown in fig. 2.22. In this plot 3D detectors are compared with strips $p+n$ [36] and $n+p$ [37], planar pixels [38] and epitaxial[6] sensors [39] (fig.2.22). The performance of 3D sensors is the best

[6]Epitaxy denotes the growing of a thin layer on a single crystal substrate. The epitaxial

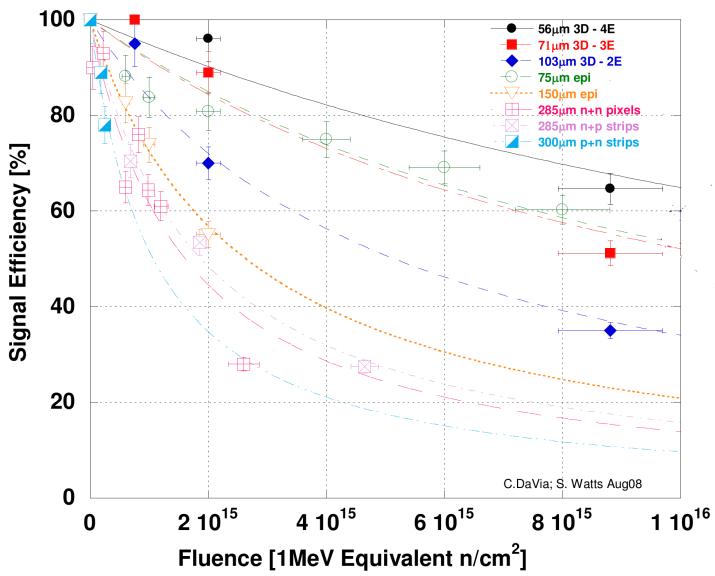

Figure 2.22: Radiation hardness of different silicon detectors. The signal efficiency loss for 3D detectors is strongly reduced with respect to the other devices [35, 36, 37, 38, 39].

one after a high radiation dose.

The data can be fitted with the curve

$$S_{\%} = \frac{\lambda}{L}\left[1 - e^{-L/\lambda}\right] \tag{2.7.1}$$

where λ is the parameter obtained from the fit and L is the electrode distance. If considering a planar and a 3D sensor, both with thickness of 210 μm and the 3D with an inter-electrode distance of 71 μm, at 10^{16} n_{eq}/cm^2 the signal of a MIP in the two sensors is:

$$S_{MIP,planar} = 2400e^- \tag{2.7.2}$$

$$S_{MIP,3D} = 10290e^- \tag{2.7.3}$$

which demonstrates that 3Ds can still work very well after high radiation doses.

layer adopts the crystal orientation of the substrate and is therefore also monocrystalline. Thanks to the Czochralski technique [40] it is possible to produce a material with high amount of oxygen impurities, producing a radiation hard detector.

2.8 FBK 3D production for CMS

Within the CMS experiment, besides the HPS project (sec. 2.5), 3D detectors are considered as promising candidates for the HL-LHC upgrade of the tracker system. 3D sensors compatible with the CMS pixel PSI46 readout chip (sec. 2.8.3) were produced by SINTEF, FBK and recently by CNM. This thesis focuses on the characterization in laboratory of 3D sensors produced by FBK with the DDTC process (sec.2.6.3).

2.8.1 CMS pixel layouts

The CMS sensors are made of 4160 pixels organised in 52 columns and 80 rows. Each pixel covers an area of 150×100 μm^2.

3Ds with single n-type electrode (1E), two n-type electrodes (2E) and four n-type electrodes (4E) per pixel cell (fig.2.23) have been designed for CMS. The resulting inter-electrode distance between readout n^+ and ohmic p^+ columns for 1E, 2E, and 4E configurations is 90 μm, 62.5 μm, and 45 μm, respectively.

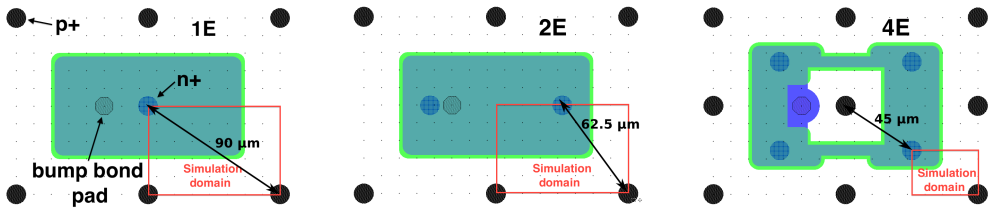

(a) 1E (b) 2E (c) 4E

Figure 2.23: 3Ds with different electrode configurations designed for CMS. The red rectangle indicates the area considered for simulation.

To study the performance of the different layouts, simulations have been performed at the University of Trento [42]. The red rectangle in fig 2.23 shows the simulation domain which can be chosen smaller than the entire pixel area due to the symmetries in column position.

The plot in fig. 2.24 shows the simulated capacitance versus the reverse bias voltage. The trend of the three curves in the plot is approximated by eq. 1.3.2. The fact that the capacitance does not seem to reach a stable plateau can be attributed to the presence of an additional capacitance component related to the n^+ to p-spray junctions [41]. The depletion voltage is already reached at very low voltage values.

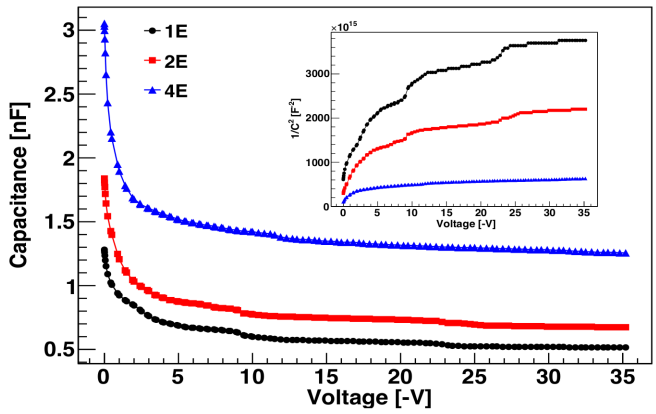

Figure 2.24: Simulated capacitance for the different electrode configurations. The corresponding $1/C^2$ versus reverse bias is shown in the inset [41].

2.8.2 ATLAS08 and ATLAS09 sensors for CMS

FBK production for CMS used of the two layouts shown in fig. 2.25. Both were produced with the double-sided process and have passing through columns.

The first layout, besides test structures, contains CMS sensors and ATLAS sensors compatible with the FE-I3 ROC, and was used for the production of a single batch of wafer, called ATLAS08.

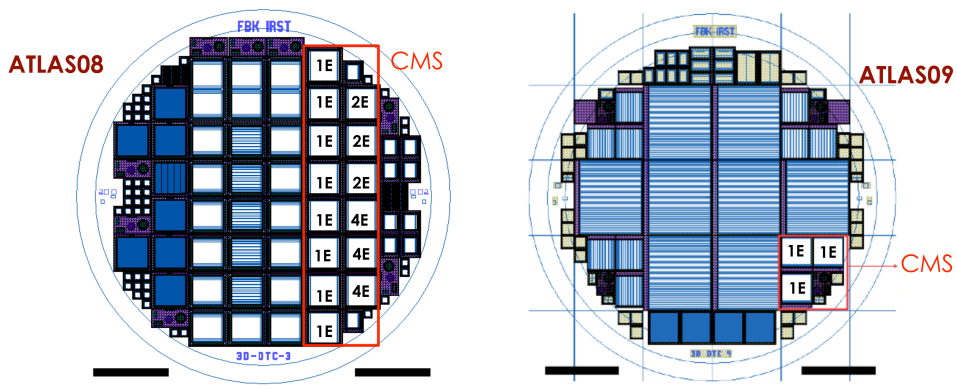

(a) ATLAS08 (b) ATLAS09

Figure 2.25: Layout of the two batches produced by FBK which contain 3D pixel sensors for CMS.

The ATLAS08 wafers accommodate eight 1E, three 2E and three 4E CMS sensors. The wafer thickness is 200 μm and standard edges with guard rings

of 1 mm are implemented. Two wafers of this batch, W3 and W8, were bump-bonded to the PSI46 readout chip at SELEX Sistemi Integrati, Italy. The bump-bond solder material is indium. All sensors tested for this thesis belong to wafer W8. A few other sensors belonging to both wafers have been previously tested in laboratory in Turin, at the University of Purdue (Indiana, USA) and at Fermilab (Illinois, USA), where they have been studied in testbeams before and after irradiation [41, 43].

The second layout is the one used for the ATLAS IBL production and mainly contains ATLAS sensors compatible with the FE-I4 readout chip. Four batches were produced with this layout: ATLAS09, ATLAS10, ATLAS11, ATLAS12. Each wafer also hosts three 1E CMS sensors with slim edges of 200 μm. Only one wafer of 230 μm thickness was bump-bonded at SELEX and the corresponding CMS sensors were tested in laboratory and with testbeam [44]. All the other wafers underwent the UBM at IZM (Germany) and several CMS sensors are currently being bump-bonded at the University of Purdue.

2.8.3 PSI46 ReadOut Chip

The CMS pixel sensors are read out by the PSI46 chip [45] designed at the Paul Scherrer Institute (PSI). It consists of a matrix of 52 $\times$ 80 pixels organized in double columns (DCol) [46]. The data are sent to the double column periphery (fig. 2.26) where are stored while waiting for the trigger decision. The ReadOut Chip (ROC) is read out serially via 40 MHz analog links.

The basic structure of the chip is the Pixel Unit Cell (PUC) which is divided in an analog part and a digital part (fig. 2.27). The signal produced in each sensor pixel and transferred through the bump-bonding enters a two-stage charge sensitive system made of a preamplifier and a shaper. The shaper output is sent to a comparator and, if it is above a preset threshold, is stored in a sample-and-hold circuit. At the same time a fast signal is sent to the column periphery via the column OR bus to warn the presence of hit information. The pixel becomes insensitive and waits to be read out.

The setting of the comparator threshold is done in two steps. A common global threshold is first set for all pixels; then, to compensate for local comparator offsets, a trim mechanism implemented with 4 trim bits allows to adjust the threshold pixel by pixel, reducing its spread within a chip from approximately 300 e^- to 80 e^-.

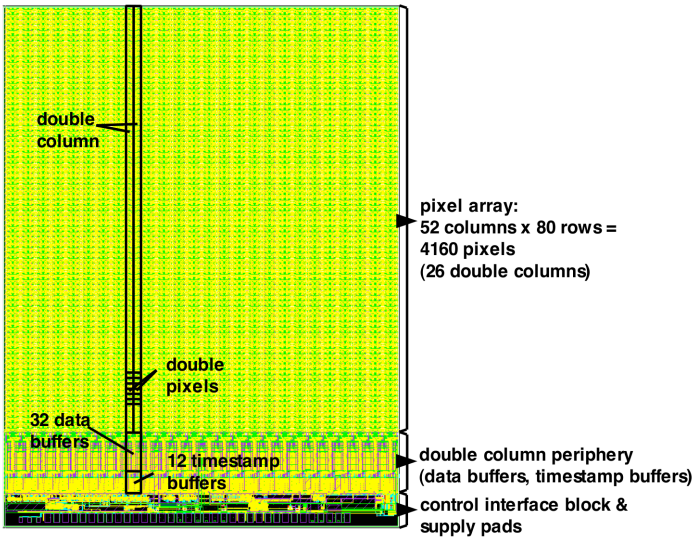

Figure 2.26: Architecture of the PSI46 readout chip.

Double column periphery

The double column periphery (fig. 2.28) controls the data transfer, stores information in buffers and performs trigger verification.

When a pixel is hit, an asynchronous column OR signal is sent to the DCol periphery and the corresponding value of the bunch crossing clock (BC) is saved in the time stamp buffer within one clock cycle (25 ns). The analog signal and the address of the hit pixel are sent to the periphery, where they are associated to the bunch crossing and stored in a second buffer, typically within six clock cycles. The mechanism of reading the pixel signals and saving the data in the DCol buffers is called "drain" and it is done in parallel for all double columns.

Pixels in the same double column are read clockwise from the bottom left to the bottom right position. The time necessary to drain a double column depends on the number of hit pixels; the resulting dead-time can be estimated as $50\,ns + (50\,ns \times number\,of\,hits)$.

Only one active and up to two pending column drains are allowed; further bunch crossing hits are lost. Time stamps and data are stored in the corresponding buffers for 3.2 μs.

The data buffer consists of 32-units, each made of a marker bit to indicate the beginning of a new event and to synchronize data and time stamp, and one analog and nine digital storage cells for pulse height and pixel address, respectively. The oldest entry in the time stamp buffer is continuously com-

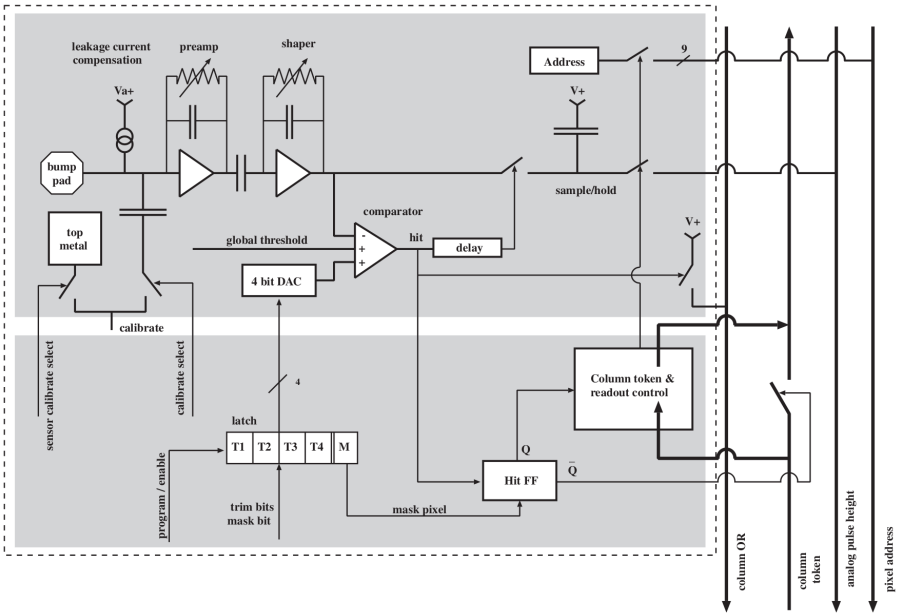

Figure 2.27: Schematic view of the pixel unit cell.

pared to the search bunch crossing counter (SBC), a 8-bit counter, delayed with respect to the BC by a programmable amount of time which corresponds to the trigger latency. In case of agreement, the trigger is checked: if it is present, the readout mode is set and the double column stops data acquisition to prevent overwriting of good data; otherwise, the time stamps and data buffers are cleared.

The output signal

The readout uses only analog differential signals. Therefore the pixel address is coded in six analog levels as shown in fig. 2.30. The readout sequence (fig. 2.29) starts with a header of three clock cycles: the first is an ultra black, a signal well outside the range of pixel data which separates the individual ROCs in the data stream. It is followed by a zero differential level (black) and then by a "last DAC", proportional to the most recently programmed DAC. After that, two levels are sent to identify the double column, followed by three levels related to the row address. The last level is proportional to the signal pulse height.

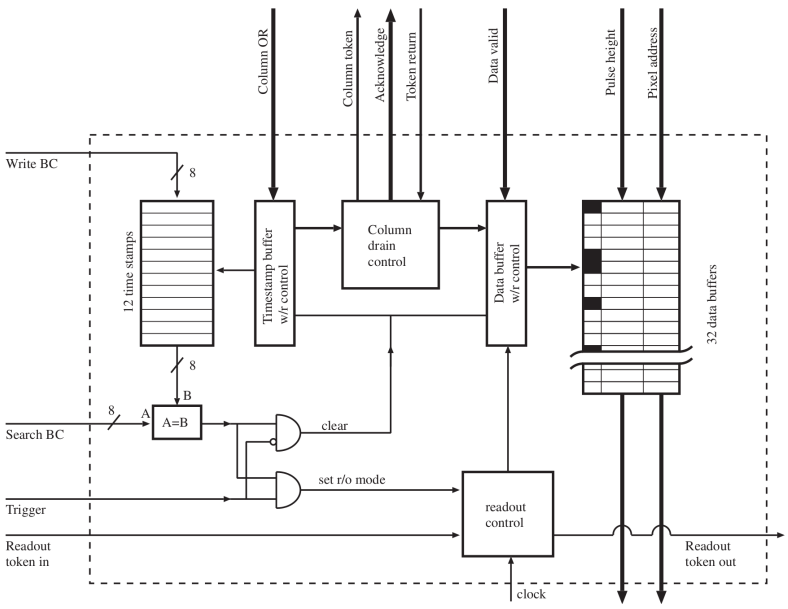

Figure 2.28: Schematic view of the double column periphery.

The calibration circuit

The chip is equipped with a self-calibration circuit which allows to determine gain and pedestal for each pixel. To this purpose, signals of different amplitudes are injected in the amplifier through a capacitor and the corresponding ADC response is recorded. The amplitude can be varied in two ranges: a low range (0-260 mV) and a high range (0-1800 mV). The signal can also be injected to a pad on the ROC surface inducing a charge in the sensor which mimics a hit in the sensor pixel. This option is used to test the quality of the bump-bonding.

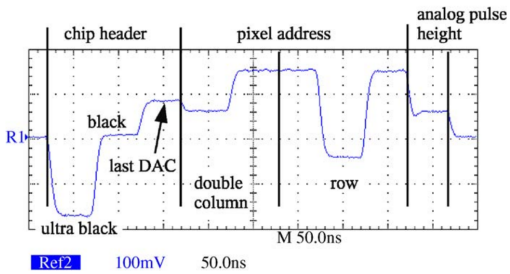

Figure 2.29: Readout sequence of a ROC with one pixel hit.

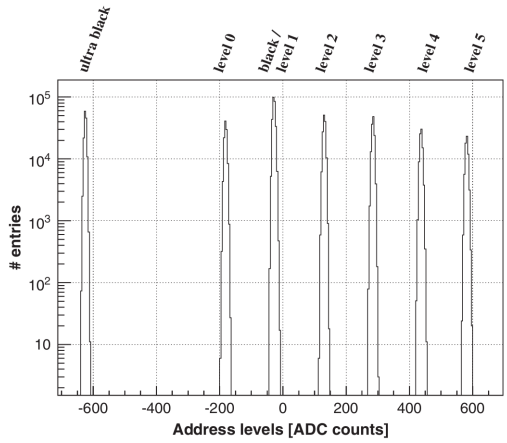

Figure 2.30: Histogram of the sampled address levels of the ROC.

Radiation hardness

Due to high energy particle irradiation, information stored in the chip can be corrupted (Single Event Upset or SEU). To protect trim and mask[7] storage cells, a capacitor is inserted in parallel to the classical double inverter structure, as shown in fig. 2.31. As a consequence, the circuit becomes slower and the critical charge needed to corrupt the saved value is increased. The probability of SEU was measured at PSI with a 300 MeV/c pion beam and was found to be reduced of two orders of magnitude with this solution. At the LHC luminosity the SEU rate is evaluated to be less that 3×10^{-2} Hz. The occupancy of each pixels is monitored online and pixel that show significant changes are reprogrammed.

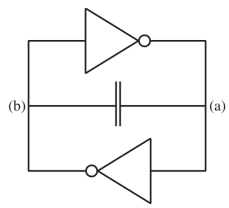

Figure 2.31: Single event upset (SEU) protected storage cell.

[7]Used for masking a pixel.

PSI46 DAC parameters

PSI46 contains more than 30 DACs used to configure and calibrate the chip. Each of them is controlled by the corresponding DAC parameter. Below, the ones which are set during the laboratory measurements reported in the next chapters are described:

- $Vana$ (8 bits) regulates the voltage applied to the preamplifier and the shaper in the range from 800 to 1300 mV. It is set to the value for which the chip analog current is $\sim$ 25 mA.
- $Vcal$ (8 bits) sets the amount of charge injected into the PUC for calibration purposes.
- $CalDel$ (8 bits) is the fine tuned delay for the injection of the calibration signal.
- $VrgSh$ (4 bits) controls the feedback resistance of the shaper.
- $VThrComp$ (8 bits) sets the global threshold value.
- $TrimBit$ (4 bits) is used to tune the threshold of individual pixels.
- $VTrim$ (8 bits) sets the global full scale for $TrimBit$ DACs.
- $VHldDel$ (8 bits) sets the delay between the time where the comparator switches to positive state and the one when the signal is sampled.
- WBC (8 bits) sets a time delay in bunch-crossing units (1 WBC unit = 25 ns). During the calibration procedure, it acts as a course delay in addition to $CalDel$. For data acquisition with external trigger it is set equal to the trigger latency.

Chapter 3

Laboratory test

For my thesis I characterized six CMS 3D sensors belonging to the W8 wafer of the ATLAS08 batch produced by FBK (sec. 2.8.2). In particular, I tested three 1E (1E_5, 1E_6 and 1E_7), two 2E (2E_10 and 2E_11) and one 4E (4E_12) sensors. The goal of my work was to study the performances of 3D silicon pixel detectors and, at the same time, to establish a procedure to be followed for future characterizations.

The complete test of the detector (sensor, read-out chip and their electrical connections) consists of four steps:

- IV curve: the leakage current is measured as a function of the bias voltage. This test is used to qualify the sensor and detect damages after dicing and chip flipping.
- ROC functionality test, DACs settings and calibration: the DAC parameters are tuned to optimize the readout chip operation. The main functionalities of the chip are verified and its calibration is performed. The noise of the detector and its evolution with the bias applied to the sensor is measured. Finally, the quality of the bump-bonding is checked.
- Source tests: the total collected charge produced by a MIP is measured as a function of the bias voltage. The full depletion voltage can be derived from the result of this test. Furthermore, the behaviour of the detector at different thresholds is observed.
- Laser test: the efficiency inside a pixel cell is studied by means of the signals produced by laser pulses.

To establish this test procedure I could profit from the experience gained by the CMS tracker group during the construction of the current pixel detector. In this chapter I will describe each step of the sensor characterization

and I will show the results obtained for the six 3D sensors mentioned above. I will dedicate chapter 4 to the laser test, since it was entirely set up by me.

3.1 Laboratory setup

Tests of 3D sensors have been performed at the Physics Department in Turin, at the Technological laboratory of INFN in Via Sette Comuni, Turin, and at CERN. The laboratory setup (fig. 3.1) is indeed compact and easily movable. It consist of a picoammeter/voltage source (Keithley 6487), a laptop and a test board.

The Keithley 6487 can be controlled manually or remotely by means of a LabVIEW program. In particular, this program is used to automatically perform the IV curve measurement.

The test board was designed at PSI for testing either single chip or modules. It provides the chip with the necessary supply voltages and electrical signals (trigger, clock, ..). An Altera FPGA controls the data flow from the readout chip to the computer. For what concerns data acquisition, the analog output of the PSI46 chip is converted by a 12-bit ADC[1] (1 ADC count corresponds to 0.128 mV and the analog signal is sampled in the interval -2048, $+2047$) and saved in a RAM of 32 M words of 16 bits, which correspond to 64 MB. To avoid the complete filling of the buffer, during data taking the memory occupancy is limited to 30 M words (60 MB). For protecting the sensor from external light during measurements, the board is closed in a black box.

The test board is connected to the computer through an USB cable and

[1]Analog to Digital Converter.

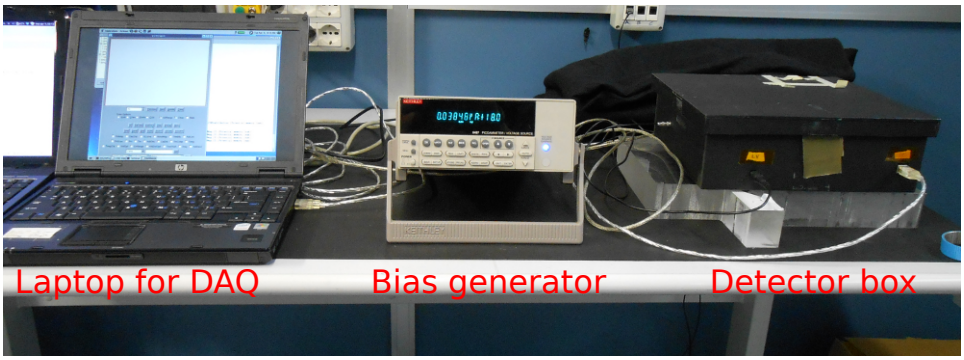

Figure 3.1: Laboratory setup.

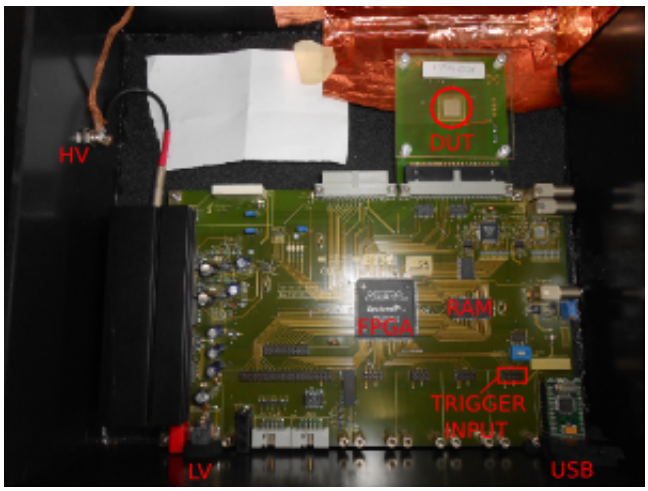

Figure 3.2: PSI board. LV stands for Low Voltage, HV for High Voltage and DUT means Detector Under Test.

data communication is controlled in a Linux environment. Calibration and data taking are performed with *psi46expert* and *takeData* programs, respectively, already compiled on the laptop. The board is also connected to a 6 V transformer which acts as a low voltage power supply.

Detectors are wire-bonded to two different boards: one designed at PSI and the other one at Fermi National Accelerator Laboratory (FNAL), both shown in fig. 3.3. The first one is smaller, with a metallised backside. As a consequence it cannot be used for irradiation tests, but it provides a better chip heat dissipation. The second one, instead, was produced for testbeam and irradiation studies and has no metallization on the backside. An adapter is needed to connect it to the PSI board. Detectors 1E_5, 1E_6 and 2E_10 were wire-bonded to the PSI board and 1E_7, 2E_11 and 4E_12 to the FNAL one.

The use of the two different boards as detector carriers has impact on the timing delay parameters and on the setup. While with the first board the source can be inserted in the black box, with the other one it must be leaned on the box cover. In this second case the distance from the chip is about 8 cm instead of $1 - 2$ cm; as a consequence, the number of hit pixels is lower.

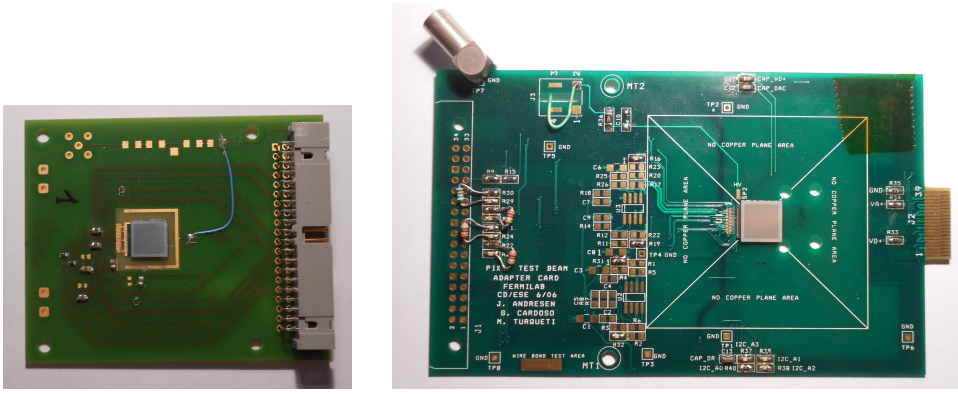

(a) DUT on PSI board (b) DUT on FNAL board

Figure 3.3: Two different boards used for testing 3Ds.

3.2 Leakage current vs bias voltage

The first step of laboratory characterization of a silicon detector is the measurement of the IV-curve. With this test it is possible to detect defects in the silicon sensor and find the maximum bias voltage that can be applied before the breakdown occurs. After this measurement, it is therefore possible to define a range for the bias voltage to be used in the following tests.

IV curves measured at room temperature for six ATLAS08 3D sensors studied in this thesis are shown in fig. 3.4. It is evident from these measurements that the leakage currents I_{leak} do not depend on the electrode configuration. All sensors have a leakage current between 50 and 120 nA. Almost all the detectors reach a plateau around 5 V and have a breakdown near 30 V with the exception of 4E_12 for which the maximum applicable voltage is 24 V. Sensor 1E_6 does not seems to work properly, since the plateau is not reached.

A singular behaviour is found for 2E_10 sensor: at about 21 V the current presents a step of $\sim$ 500 nA, then it stabilizes until the breakdown occurs at 28 V. This effect is thought to be due to a local defect.

For all the sensors the breakdown voltage is lower than expected. This is to be attributed to the high p-spray implanted dose. It should be remembered that the sensor tested belongs to a pre-production batch. The p-spray implanted dose was reduced in later batches and the reverse discharge was found to occur at higher voltages [47].

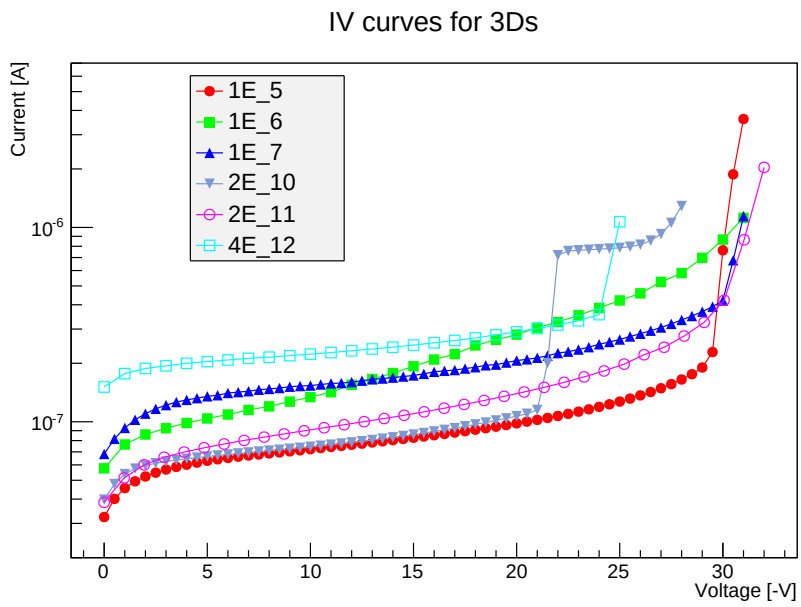

Figure 3.4: IV curves measured for six 3D sensors belonging to the ATLAS08 batch.

3.3 ROC functionality tests, DACs setting and calibration.

The tests and the calibration of the PSI46 readout chip in performed with the program *psi46expert*. The complete procedure is reported in appendix A; in this section I will focus on the fundamental steps. All the results presented here were obtained with detector 1E_5.

At the beginning all DAC parameters are set to their default value. For a more comprehensive explanation of these parameters refer to sec. 2.8.3.

3.3.1 Address Level

As explained in sec. 2.8.3, the PSI46 readout is completely analog. Each pixel address is coded with a six level analog signal. To avoid wrong decoding, these six levels must be clearly separated, like the ones shown in fig. 3.5. The further level with the lowest voltage value is called ultra black and used to separate signals from different ROCs in the data steam.

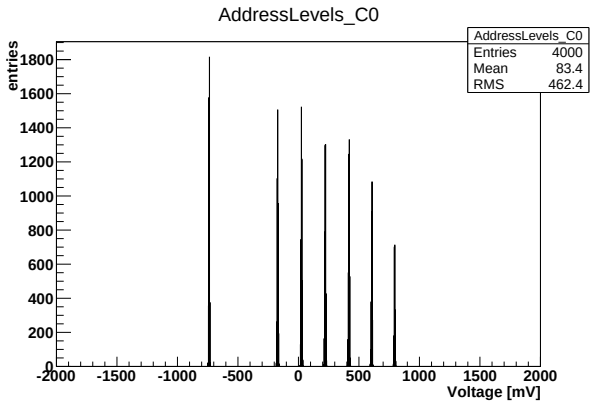

Figure 3.5: Histogram showing the ultra black signal and the six analog signals used for coding the pixel address. These levels must be sharp and well separated.

3.3.2 Setting of CalDel and VThrComp

In order to find the correct value of the comparator threshold ($VThrComp$) and of the delay of the calibration signal ($CalDel$), the chip efficiency is measured as a function of two. This step is very important because the ROC can only work in a specific region of the $VThrComp$ and $CalDel$ plane. For each value of $CalDel$ and $VThrComp$, five calibration signals are injected and the number of hits in the readout is counted. The amplitude of the calibration signals is set to 200 DAC units in low range. Since the working range does not change significantly within the same ROC, this procedure is performed only for one pixel. The typical shape of the working area is shown in the two dimensional histogram of fig. 3.6.

$VThrComp$ is set adding 50 DAC units to the minimum value of this parameter for which the signals are read out:

$$VThrComp_{set} = VThrComp_{min} + 50 \tag{3.3.1}$$

$CalDel$ is chosen as the mean value of the readout range corresponding to $VThrComp_{set}$. The described procedure works only if the working area is well centred with respect to the limits of the two dimensional histogram. To be in this situation, the WBC has to be set properly at the beginning of the test.

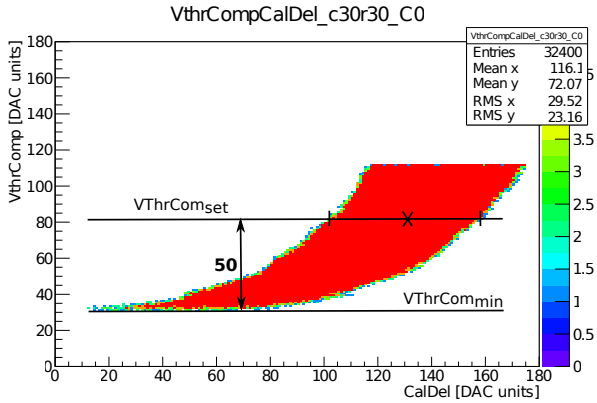

Figure 3.6: Two dimensional histogram used to determine a stable working point in the *CalDel-VThrComp* plane.

3.3.3 Pixel readout test

The correct functionality of each pixel is verified by sending ten calibration pulses with a *Vcal* value of 200 in the low range and reading out the corresponding analog signal. Since only one pixel at a time is enabled, it is sufficient to check for the presence of any hit in the analog readout. If less than ten hits are recorded the pixel is classified as dead; if more than ten hits are counted, the pixel readout is considered noisy. A typical result is shown in fig. 3.7.

This test also controls that pixels do not respond if they are masked. If this does not occur, the mask bit is labelled as defective. This functionality is very important since it is used to disable noisy pixels, which could prevent a whole double column from working properly by filling up the buffer in the DCol periphery.

3.3.4 TrimBit test

As described in sec. 2.8.3, the threshold can be adjusted pixel by pixel with a 4-bit DAC called *TrimBit*. To verify that this DAC works properly a *TrimBit* test is performed. The threshold is measured for each pixel five times: once for the untrimmed state and four times for the different values of *TrimBit* (7, 11, 13 and 14) obtained setting to zero only one bit at a time. A bit is considered defective if the difference between trimmed and untrimmed threshold is less than three DAC units. The typical result of the TrimBit test is shown in fig. 3.8. In this case problems do not occur.

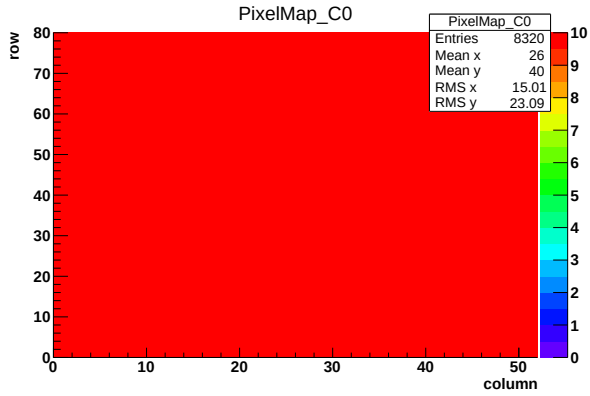

Figure 3.7: Pixel map. For this detector all pixels work fine.

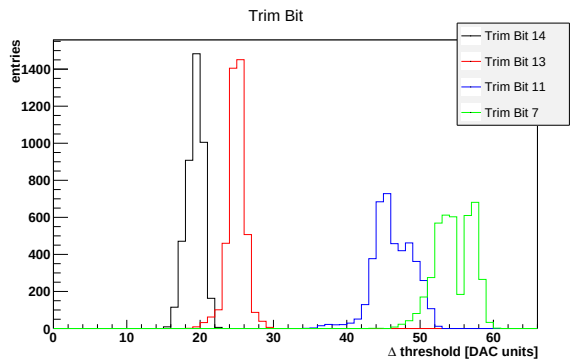

Figure 3.8: TrimBit test. In this case all the entries are higher than three DACs, ensuring that trimming is working correctly.

3.3.5 Trimming procedure

Trimming is the procedure used to equalize the threshold of all pixels in a ROC. Three DAC parameters are involved: $VThrComp$, $Vtrim$ and $TrimBit$.

$VThrComp$ is the global threshold; since signals at the end of the double stage amplifier are negative, increasing $VThrComp$ corresponds to decreasing the comparator threshold.

$Vtrim$ globally sets the range in which the threshold of each pixel can be reduced.

$TrimBit$ is the local 4-bit DAC which gives the value to be subtracted

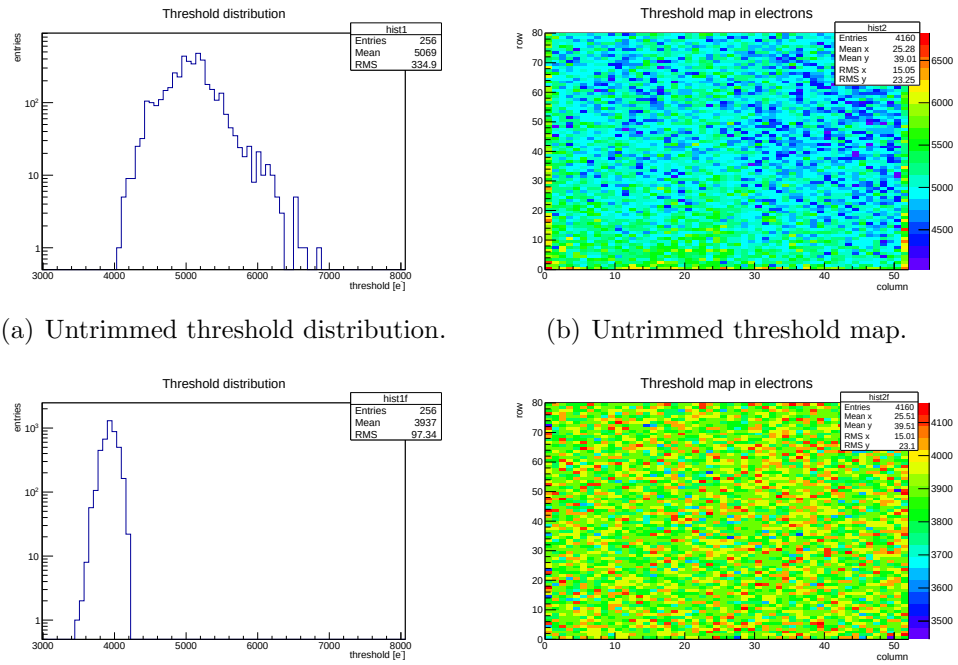

(a) Untrimmed threshold distribution.

(b) Untrimmed threshold map.

(c) Trimmed threshold distribution.

(d) Untrimmed threshold map.

Figure 3.9: Threshold distributions and maps before (upper plots) and after (lower plots) the trimming procedure. The plots on the left show that for the 1E_5 sensor the threshold was reduced from 300 e^- to less that 100 e^-.

to the global threshold to obtain the final threshold of each pixel:

$$V_{thres} = V_{ThrComp} - V_{trim} \cdot \frac{15 - TrimBit}{16} \tag{3.3.2}$$

The first step of the trimming procedure is to find the value of $VThrComp$ which corresponds to the target threshold (Thr_{target} defined in e^-). This is done by injecting pixel by pixel a signal with an amplitude $Vcal$ equal to Thr_{target} and by measuring the value of $VThrComp$ for which 50% of the signals are collected. The lowest value obtained (i.e. the highest threshold) from all pixels is chosen as the global $VThrComp$. This choice is motivated by the fact that the threshold can only be lowered with the trimming.

At this point $VTrim$ has to be fixed. First, the $Vcal$ value which corresponds to the $VThrComp$ set in the previous step is measured for each pixel. The pixel which needs the highest value of $Vcal$ is used to determine $VTrim$. For this pixel $TrimBit$ is set to 0 (i.e the threshold minimum value) and $VTrim$ is increased until its threshold corresponds to Thr_{target}.

Once $VTrim$ is set, pixel by pixel the $TrimBit$ configuration for which

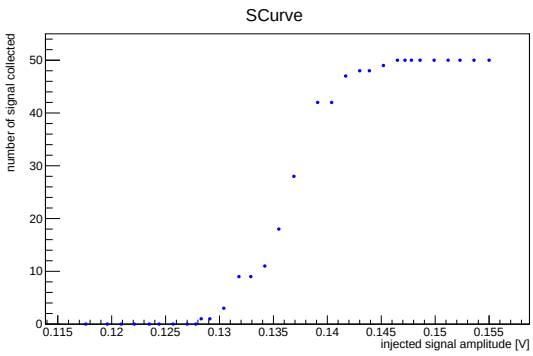

Figure 3.10: S-curve measurement. Fifty signals are sent to the amplification chain for each increasing amplitude and from the collected hits the efficiency is determined.

the threshold is as close as possible to Thr_{target} is found, with the same procedure applied in the first step.

Figure 3.9 shows the distribution of the thresholds before and after the trimming procedure for the chip bump-bonded to the sensor 1E_5. The effect of the trimming in reducing the threshold spread is clearly visible.

3.3.6 Noise vs bias voltage

An important aspect for the qualification of a detector is the identification of the noisy channels. The noise level of each pixel is determined by measuring the so-called S-curve, which represents the response efficiency as a function of the calibration signal amplitude. For an ideal pixel without any noise, this would be a simple step function: zero efficiency below the signal threshold and full efficiency above. The effect of the noise is to smear this step function. If the noise is assumed to be gaussian, the S-curve has the shape of an error function, with a width proportional to the noise.

An example of a measured S-curve is shown of fig. 3.10. For each value of the signal amplitude in the plot, 50 calibration pulses are injected in the pixel and the number of detected hits is recorded. The S-curve is fit by the error function:

$$Eff(x) = a \cdot \frac{2}{\sqrt{\pi}} \int_0^{c\cdot(x-b)} e^{-t^2} dt \; + \; d \tag{3.3.3}$$

and the width (noise) and the position of the 50% point (threshold) are extracted from the fit.

The noise distribution for the 1E_5 sensor is shown in fig. 3.11. The small

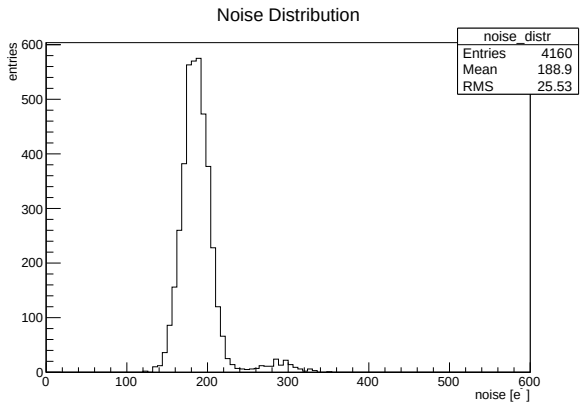

Figure 3.11: Noise distribution.

second peak at higher noise values is due to the pixels at the edges of the sensor, which have a double surface, i.e. a double capacitance. This pixel configuration was chosen to adapt the sensor to the PSI46 ROC [48].

The evolution of noise as a function of the applied bias voltage was measured for all sensors. Since the main contribution to the noise is directly proportional to the pixel capacitance (eq. 1.3.4), noise measurement can provide information on the depletion voltage. In fact, increasing the bias voltage the depletion region becomes more extended and the capacitance reduces, also reducing the noise.

The capacitance, and consequently the noise, also decreases when the electrodes distance increases. As a consequence, the noise is expected to be lower for sensors with a smaller number of electrodes per cell.

The noise measurements made on the tested detectors are shown in fig. 3.12. The first thing which can be observed is that the trend vs the bias voltage is the one expected. Detector 2E_10, as will be shown in sec. 3.4.1, has several noisy pixels and this effect is visible in the plot. Also detector 1E_5 seems to have a problem of noise, however from the qualification procedure (result shown in fig. 3.21) this does not seem to influence the sensor behaviour. With the exception of these two sensors, the distribution of the noise as a function of the electrode configuration is the one expected. In particular, sensors 1E_6 and 1E_7 have a noise slightly lower than 2E_11 and sensor 4E_12 has the highest noise, which almost reaches 240 e^- at full depletion.

3.3.7 Bump-bonding test

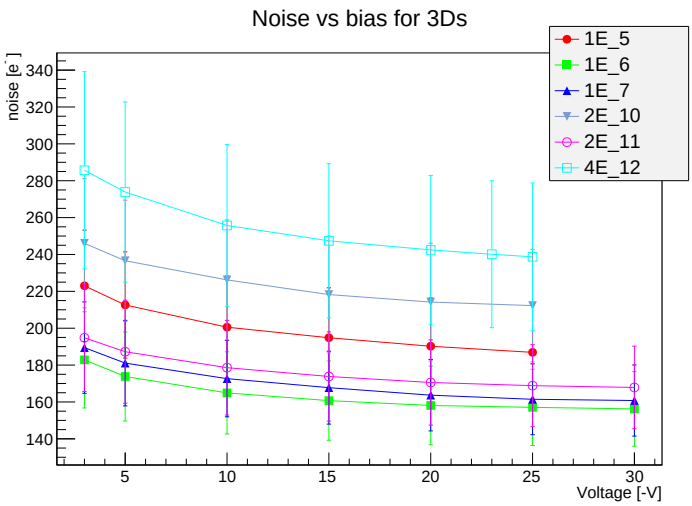

Figure 3.12: Measured noise as a function of the bias voltage.

The easiest way to test the quality of all bumps would be to send a calibration signal through the air capacitance described in sec. 2.8.3, and verify if it is recorded by the chip. However, occasionally the bump-bond is not completely missing but has only a poor connection to the sensor or to the ROC [49]. Even worse, if the signal amplitude is large enough, a hit can be triggered although the bump is missing. These hits are supposed to be originated from cross talk via a parasitic coupling between the calibration voltage line and the preamplifier.

In order to detect also this kind of problems the threshold is measured twice, first injecting directly the calibration signal into the sensor and then via cross-talk by keeping at the same time opened the two switches of the calibration signal shown in fig. 2.27. Only if the difference between these two values is greater than 5 DAC units, the quality of the bump is considered good for the pixel. Indeed the difference ensures that the directly injected signal does not suffer a cross-talk. Figure 3.13 shows the results for the 1E_5 detector.

3.3.8 Pulse height calibration

The aim of the calibration is to determine the parameters which are needed to convert the pulse height of the signal produced in the pixel by a traversing particle to the deposited charge. Ten calibration pulses are sent and read out, five in the low range and five in the high range of the signal amplitude.

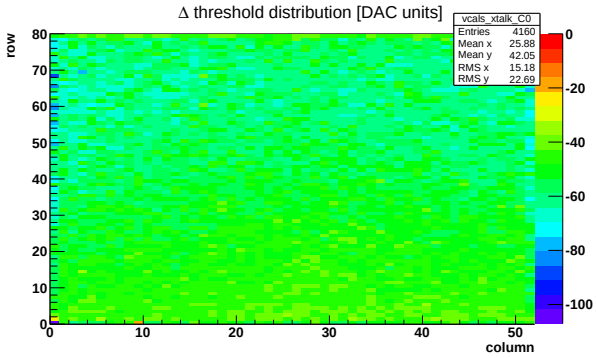

Figure 3.13: Bump-bonding test. The map shows that all the pixels are correctly bounded.

The amplitude values are chosen in such a way that the second-last point in the low range and the first point in the high range overlap.

Data are fitted by:

$$V_{PulseHeight} = d + c \cdot tanh(a \cdot charge - b) \tag{3.3.4}$$

and parameters a, b, c and d are estimated from the fit. The product $a \cdot c$ represents the gain, d is the pedestal and b is an estimator of the non-linearity of the response. To achieve the optimal hit resolution b has to be as small as possible.

The calibration procedure is repeated for each pixel. Fig. 3.15 shows the pedestal and the gain distribution obtained for sensor 1E_5.

Once the calibration is available, any signal pulse height can be converted in the corresponding ionization charge through the inverse function of eq. 3.3.4 with the parameters fixed by the fit. The result, in $Vcal$ units, has then to be converted in e^-. The conversion factors were measured with a variable energy X-ray source at PSI [50], and were found to be 65 e^- per $Vcal$ units in the low range and 455 e^- per $Vcal$ unit in the high range.

3.3.9 Summary page

In order to spot problems, a chip summary page with the main results of the tests described above is produced at the end each characterization. The summary pages of the six detectors analysed in this thesis are shown in the following pages.

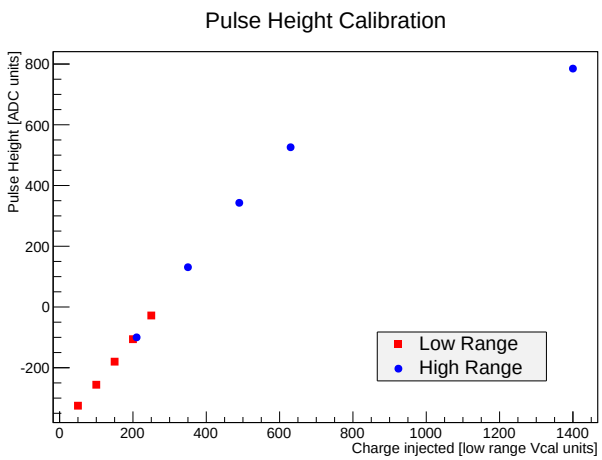

Figure 3.14: Calibration curve for one pixel of sensor 1E_5. The DAC values for the high range points are multiplied by a factor of 7 to take into account that the signal amplitude in the high range is about seven times higher than in the low range for the same DAC setting.

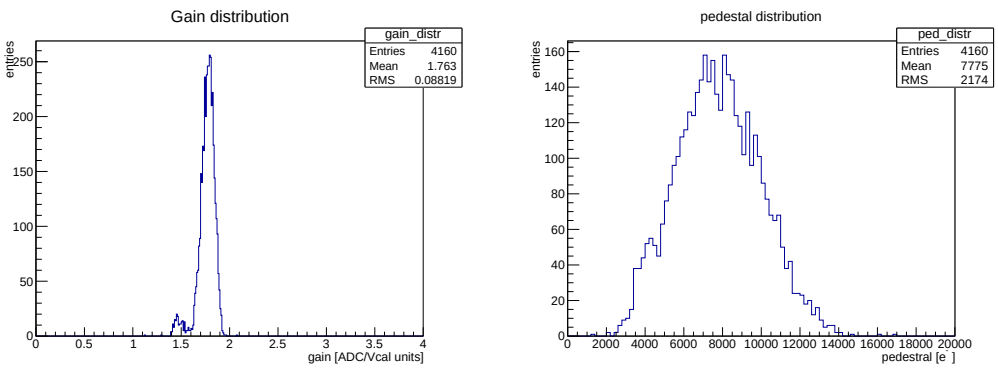

(a) Gain distribution.

(b) Pedestal distribution.

Figure 3.15: Pedestal and gain distributions obtained for sensor 1E_5.

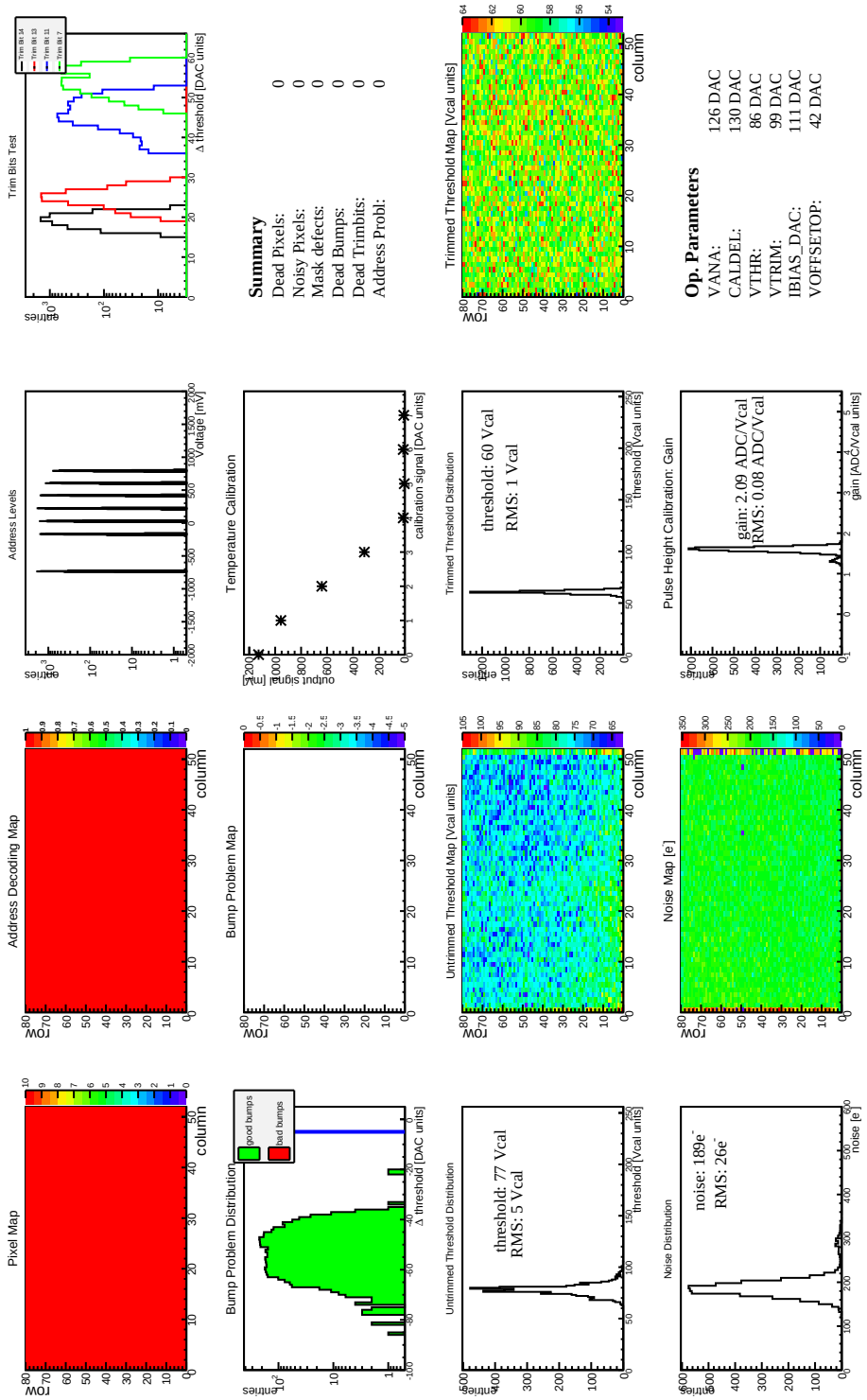

Figure 3.16: Chip summary page for 1E_5 detector.

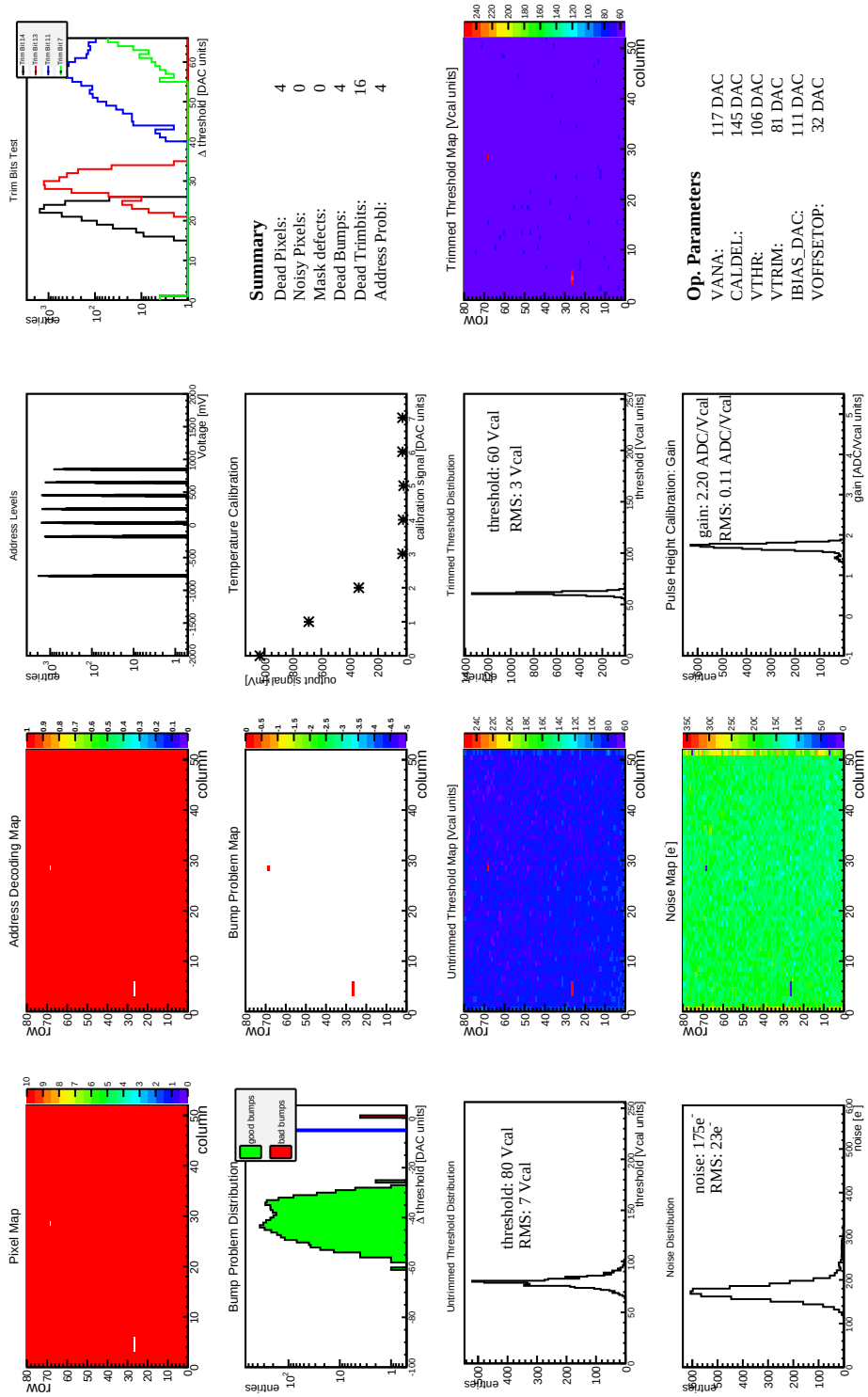

Figure 3.17: Chip summary page for 1E_6 detector.

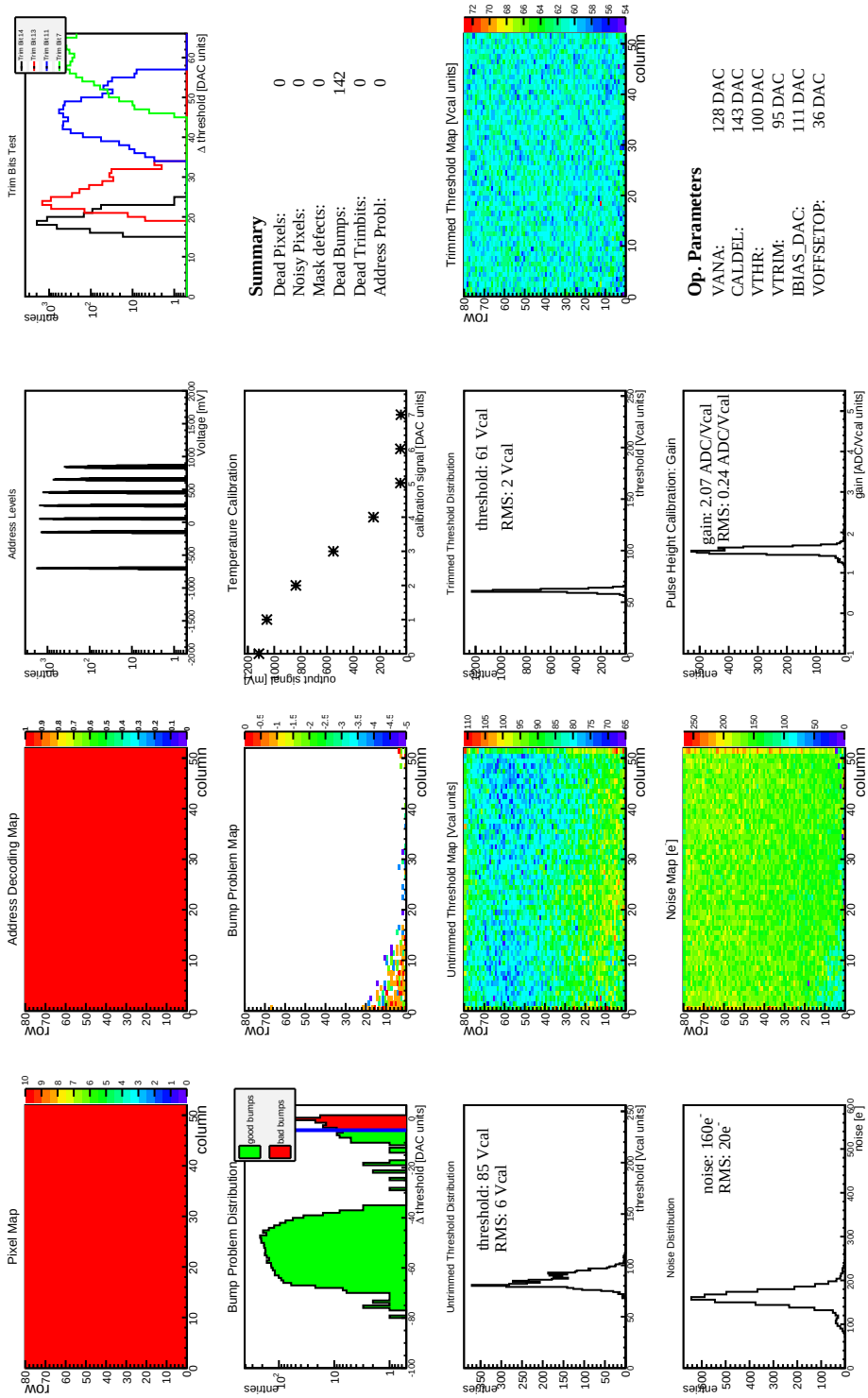

Figure 3.18: Chip summary page for 1E_7 detector.

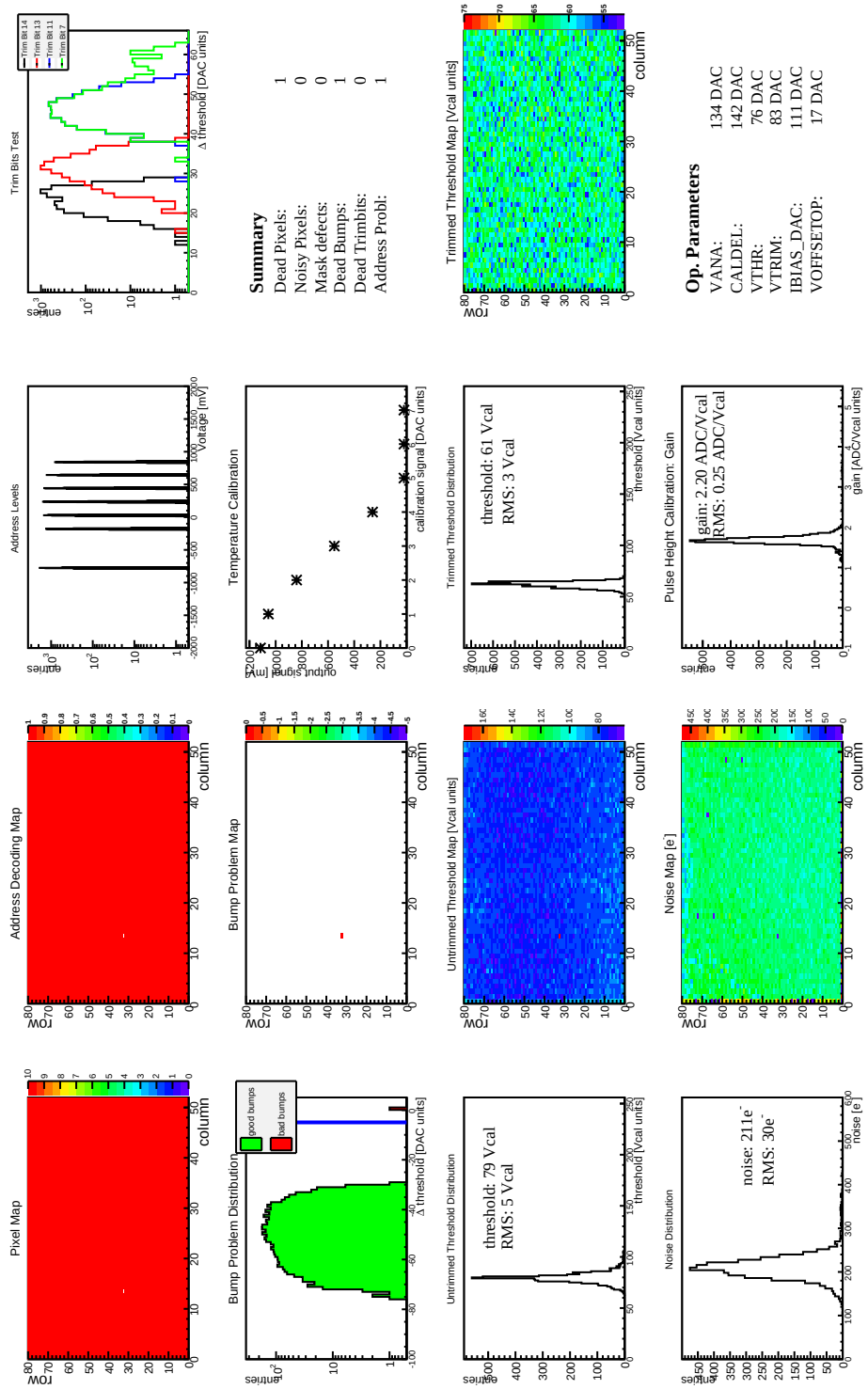

Figure 3.19: Chip summary page for 2E_10 detector.

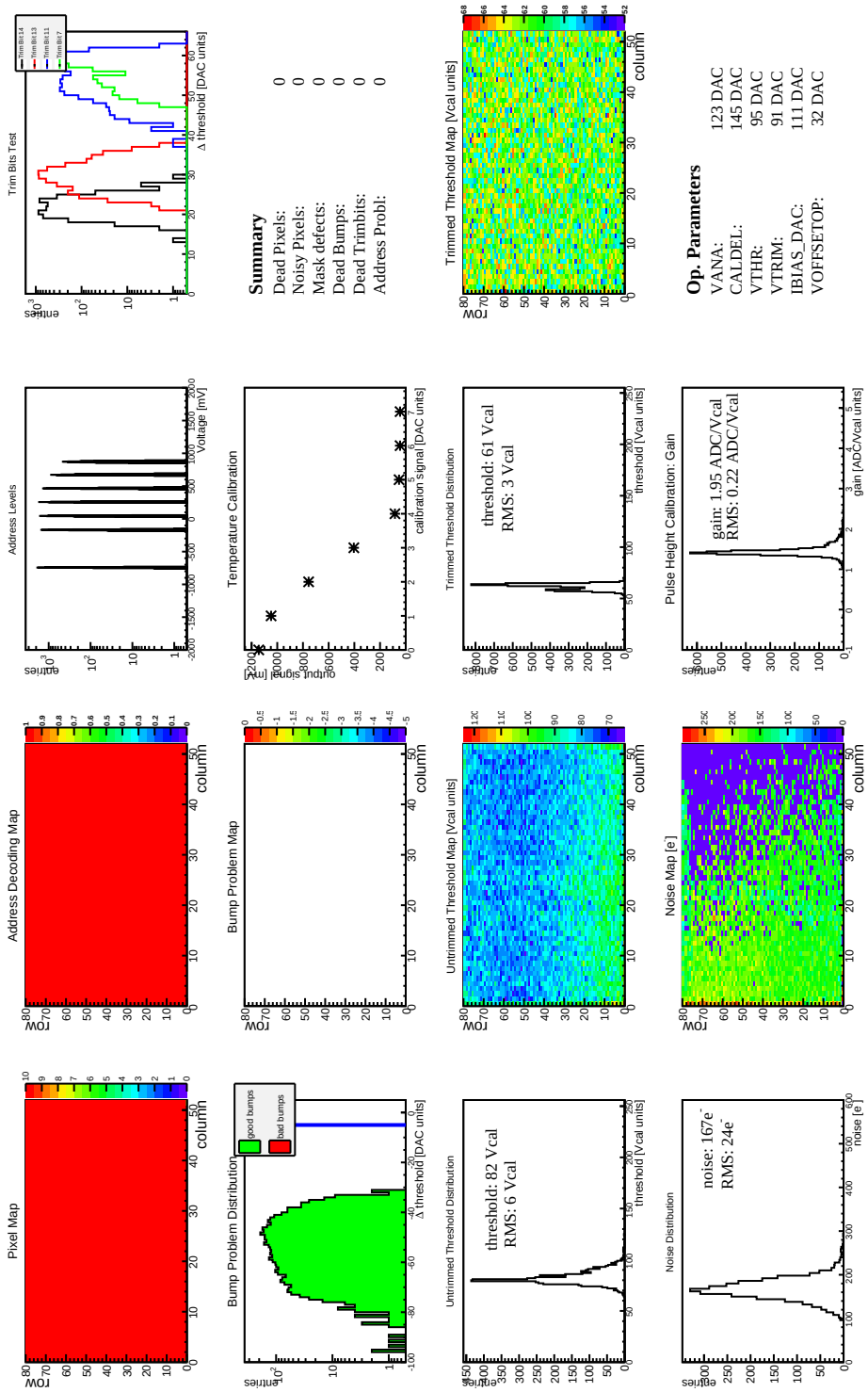

Figure 3.20: Chip summary page for 2E_11 detector.

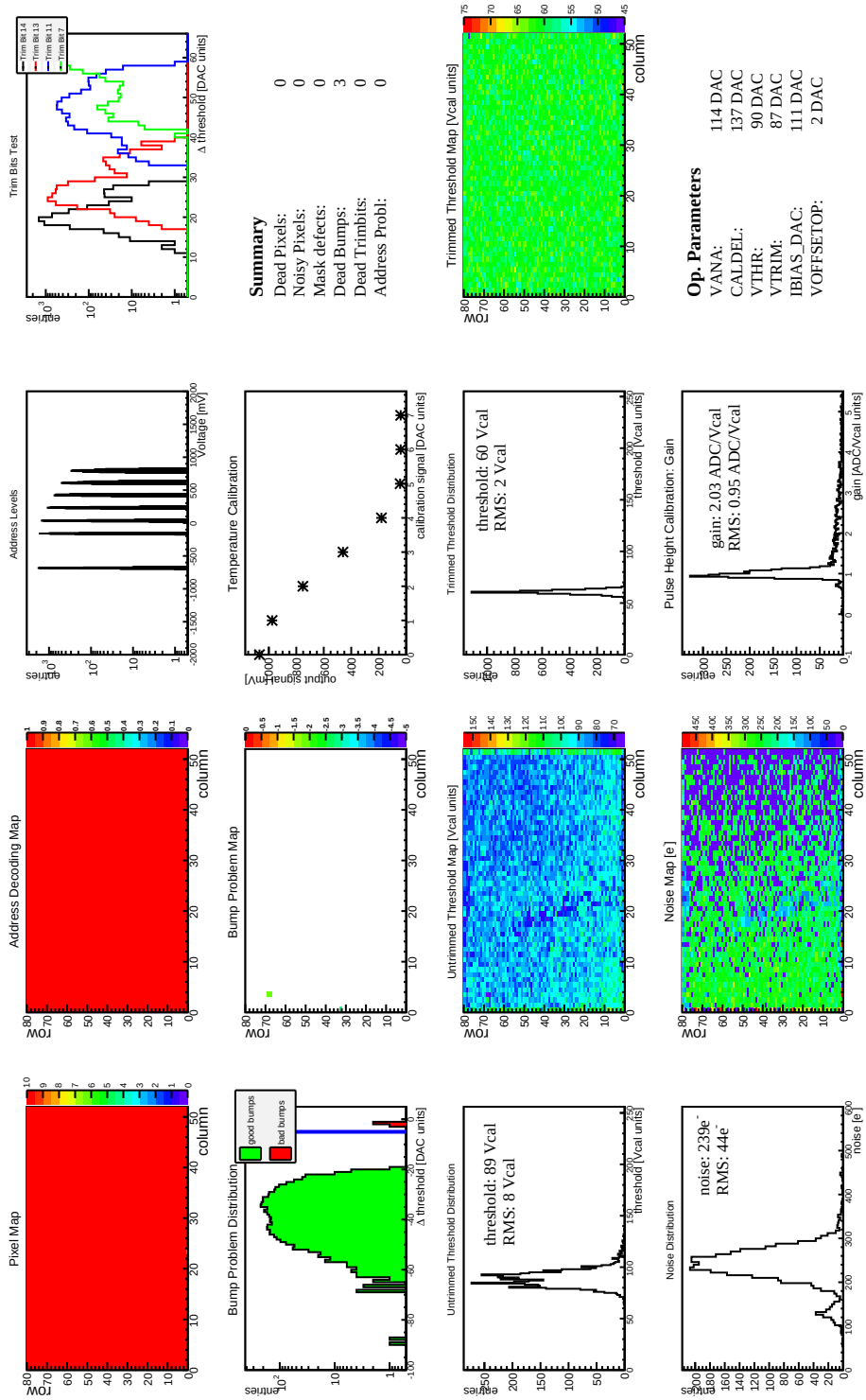

Figure 3.21: Chip summary page for 4E_12 detector.

3.4 Source tests

Tests with radioactive sources are a very convenient way to study the performance of the detectors in laboratory. For this thesis two types of measurements have been performed using ^{90}Sr β^- sources. The detector behaviour has been studied as a function of the readout threshold, to verify that the standard value of 60 $Vcal$, used for the CMS planar pixel detectors, is still reasonable for 3D detectors. The other important measurement done has been the evaluation of the collected charge.

3.4.1 Data acquisition and analysis software

The data acquisition is made with the *takeData* software, written at PSI specifically for the board. The graphical user interface allows to set, besides other parameters, the acquisition time and the trigger delay (WBC).

Acquisitions made for the source tests have been performed using the internal random trigger given by the FPGA on the PSI board. From the results obtained it can be derived that the internal trigger frequency is about 15.5 kHz. The external trigger has not been used for these tests.

A relevant problem encountered with the data acquisition system is the small dimension of the memory used to store the data on the PSI board. Since each time there is a trigger an header is stored, even if the trigger do not validate hits, the memory fills rapidly. As a consequence, it is not possible to run an acquisition for more than 100 s even if no entries are registered. This problems prevents to use sources with low activity of the order of the kBq, which would need a longer acquisition time.

Also the presence of a lot of noisy pixels is a problem for the memory filling. In the software the masking procedure was implemented but did not seem to work properly. Therefore I have modified the DAQ software to include this possibility of masking noisy pixels. The result is visible in fig. 3.22, where the pixel map of detector 2E_10 is shown before and after masking the noisy pixels.

Data acquisition saves information in a binary file, which is then converted in a ROOT Tree for the analysis. Several macros allow to study the detector response, and in particular to measure the distribution of the collected charge.

3.4.2 Detector behaviour with different thresholds

An important parameter for the efficiency of a detector is the readout threshold. Its value must be high enough to cut the noise but at the same time needs to be as low as possible to avoid losing useful signals. Indeed, a

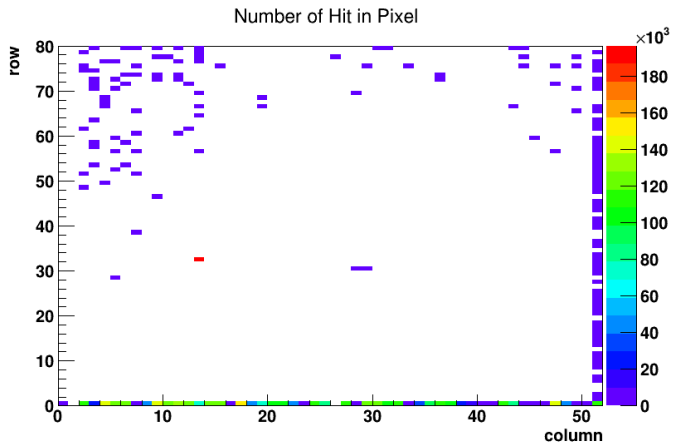

(a) Before masking

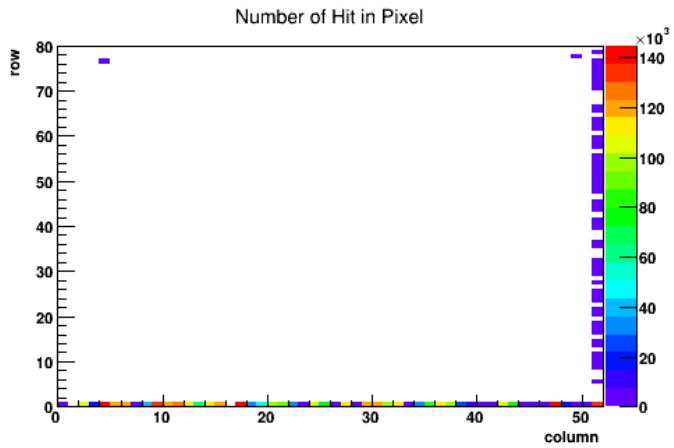

(b) After masking

Figure 3.22: Effect of masking on the 2E_10 detector.

particle leaving a charge deposit in more than one pixel, forming a cluster, can be tracked more precisely using the charge sharing in between hit pixels, and a too high threshold would cut the signal of some of these pixels reducing the spatial resolution of the detector. An interesting measurement is thus a threshold scan to understand when the noise contribution starts to be seen.

Tests were performed at the Technological Laboratory of INFN-Torino. The source used for these measurements is a ^{90}Sr β^- emitter whose precise activity could not be measured. The nominal activity of $\sim$ 31 MBq was attenuated by a thin plexiglass layer since during the same period the source was used for testing muon chambers. A consequence of the multiple scattering due to the attenuation layer was the increase of the cluster size.

The measurements were performed with and without source, to ensure that the measured signals were not noise. A known characteristic of the PSI46 readout chip is that it does not work with too low thresholds, for which even noise higher than the threshold is not detected. This was confirmed by the tests done for this thesis.

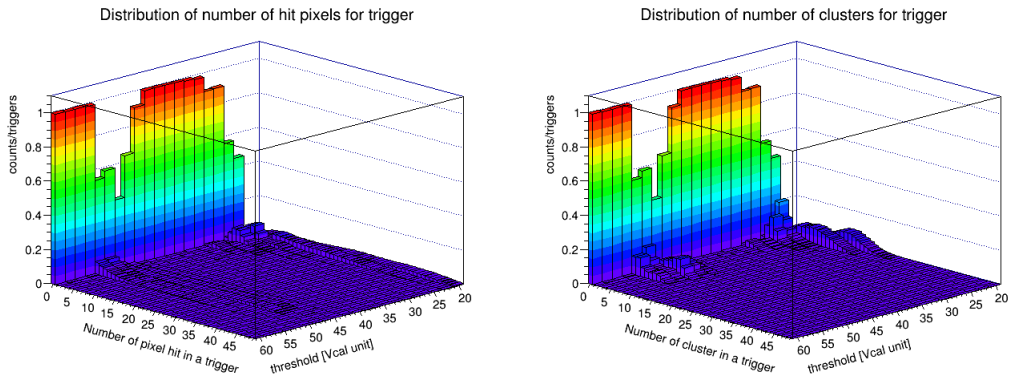

(a) Without source.

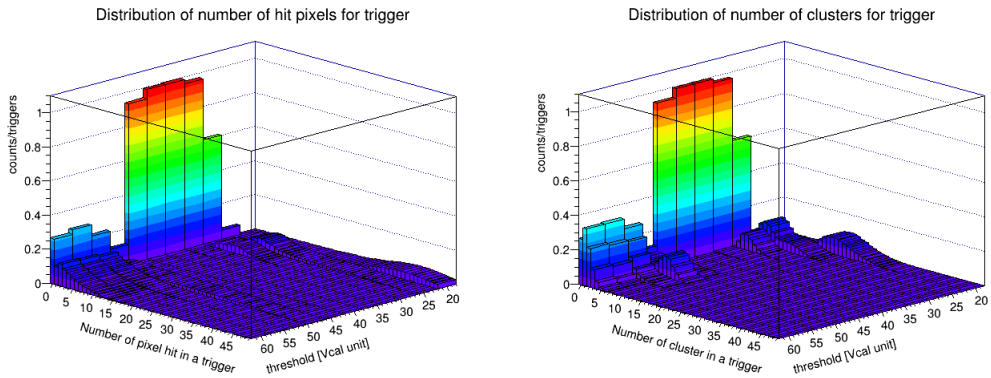

(b) With source.

Figure 3.23: Behaviour of detector 1E_5 at different thresholds.

The chosen way to illustrate the results of a threshold scan is a three dimensional plot like those shown in fig. 3.23. For each value of threshold the number of hit pixels in a trigger is plotted, normalized to the number of triggers of the acquisition to make the measurement independent of the acquisition time. The threshold is expressed in $Vcal$ units, which can be converted in electrons multiplying by 65 $e^-/Vcal$. The same distribution is also plotted after the clusterization, which is important to consider in case of measurements with source. The threshold of 60 $Vcal$ optimized for planar sensors, corresponding to 3900 e^-, is found to be adequate also for 3D sensors.

Results for the different sensors are collected in appendix C. Here only the measurements for sensor 1E_5, without (fig 3.23(a)) and with the source (fig. 3.23(b)), are shown. This detector presents a particular behaviour. Trying to lower the threshold while measuring without the source, the detector becomes noisy at $54\,Vcal$, but then it seems to work properly again between $42\,Vcal$ and $34\,Vcal$. However, when taking data with the source in this latter interval no signal is measured, indicating that these threshold values do not allow the correct behaviour of the detector.

The evaluation of the working threshold of a detector is even more important for testbeam measurements. I did an analysis to get the thresholds of 3D detectors tested with beam at the Fermi National Accelerator Laboratory (FNAL) in Batavia (Illinois, USA). Since this work is not directly related to the thesis, it can be found in appendix D.

3.4.3 Charge collection

The measurements of the charge collection as a function of the bias voltage have been performed at CERN with a ^{90}Sr source producing electrons by β^- decay. The source has an activity of 2.53 MBq and the emitted electrons have a maximum energy of $E_\beta = 0.546$ MeV. This source did not have any attenuation layer, which determined smaller cluster sizes with respect to the ones measured for the threshold scans discussed in sec. 3.4.2. The two cluster size distributions for sensor 1E_5 are compared in fig. 3.24(a) and fig. 3.24(b).

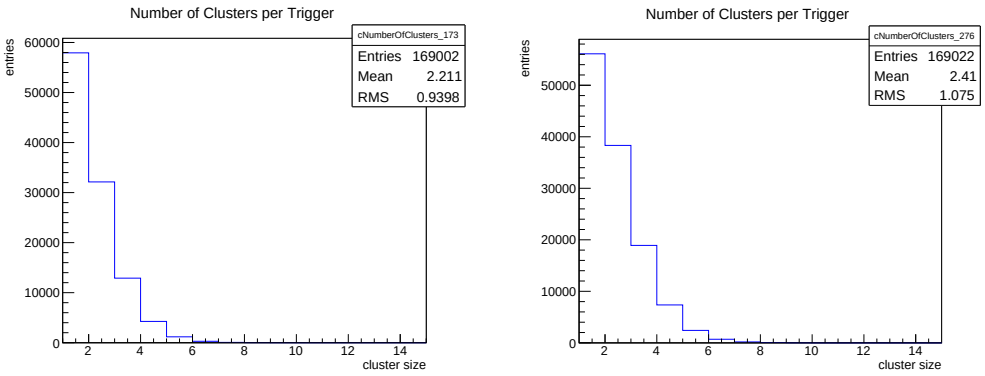

(a) CERN source. (b) INFN source.

Figure 3.24: Cluster size distributions. Events with cluster size zero (no hit pixel) are not drawn.

As described in sec. 1.1.1, the energy deposited by a MIP in the sensor should have a Landau probability distribution. The ideal distribution is

affected by the detector noise, which can be assumed gaussian. Therefore the function used for fitting the charge collection is a convolution of these two distributions. The most probable (MP) value obtained by the fit is taken as the collected charge.

Sensors considered for the charge collection measurements were 1E_5, 1E_7, 2E_10 and 2E_11. As an example, fig. 3.25 shows the result for sensor 1E_5.

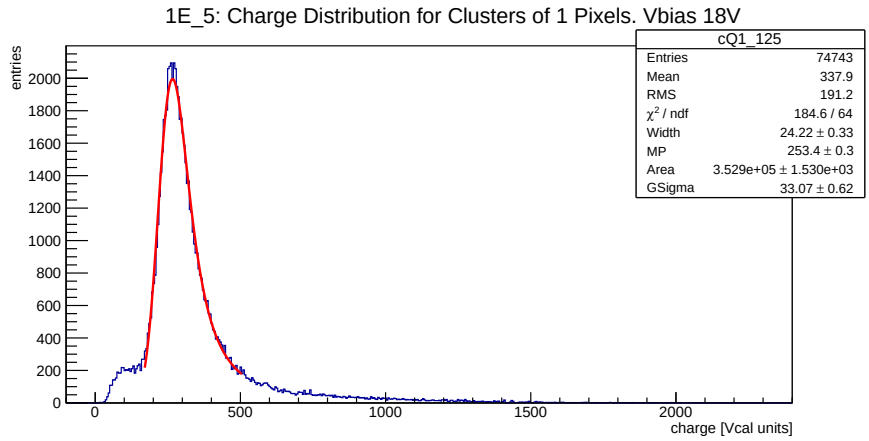

Figure 3.25: Example of a charge collection for 1E_5 sensor.

In the plot the charge is expressed in $Vcal$ units. The conversion factor which allows to convert $Vcal$ units in electrons was measured for planar sensors with X-rays. The obtained value is $1\,Vcal = 65$ e$^-$ [49]. Looking at the pixel unit cell shown in fig. 2.27, one can see that the signal at the input of the amplification chain due to the calibration charge injection is influenced by the calibration capacitor and by the sensor capacitance, which is connected to the bump-bonding pad. A different sensor capacitance varies the conversion factor. For these reason, the data which are presented here might have problems with the conversion in electrons.

Nevertheless, the measurement of the charge collection as a function of the bias voltage is very interesting to understand the working point of the detector. The results of the measurements are presented of fig. 3.26. The plots show the charge collected in electrons for the four sensors which have been tested. Figure 3.26(a) shows the results for events with cluster size of one pixel, while fig. 3.26(b) shows the events with cluster size of one or two pixel.

As explained above the value in electrons is not reliable. Sensors have a thickness of 200 μm. The electron-hole pairs generated in silicon are approxi-

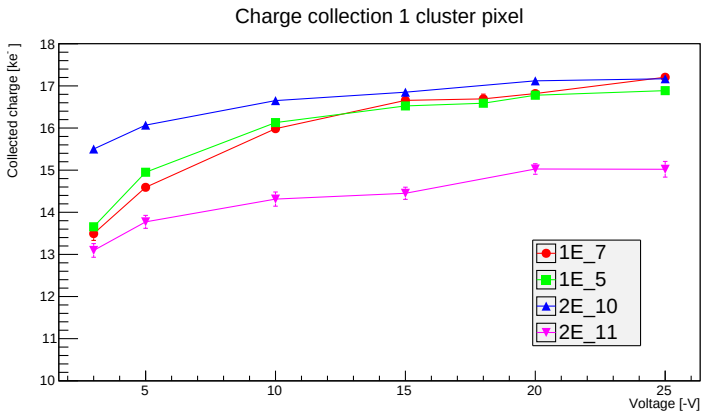

(a) Charge collection as function of bias voltage for events with cluster size 1

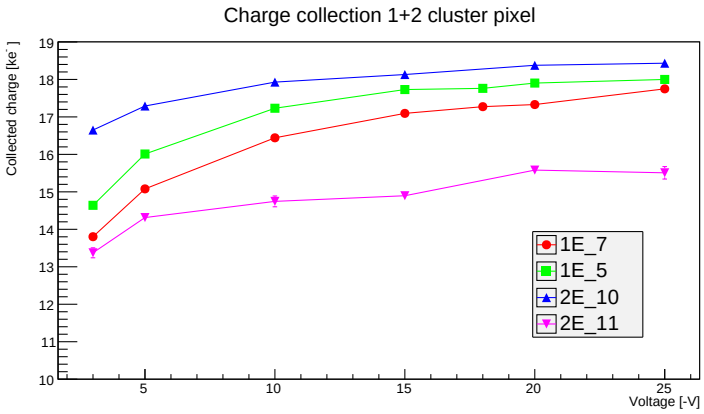

(b) Charge collection as function of bias voltage for events with cluster size 1+2

Figure 3.26: Charge collection as function of bias voltage.

mately 80 pairs/μm. Therefore 16 ke$^-$ are expected, which is not compatible with the results plotted in fig. 3.26.

In spite of this, some interesting observations can be derived from the plots. In particular, the difference in reaching the plateau between 1E and 2E sensors is evident. As expected, sensors with lower electrodes distance (2E) are depleted, and hence collect all deposited charge, at lower voltage. In fact, while 2E sensors at 10 V completely collect the deposited charge, 1E ones need at least 15 V.

3.5 Conclusions on laboratory tests

A few FBK 3D sensors for CMS, with different electrodes configurations, have been characterized in laboratory. A procedure for the test measurements has been derived and it consists of five steps: chip calibration and functionality tests, IV curve, noise vs bias voltage, detector behaviour at different thresholds, and charge collection vs bias voltage.

Functionality tests and setting of the DACs are necessary for the correct behaviour of the readout chip and provide essential information on the detector, like the bump-bonding status. For having an immediate response, a summary page has been created, which summarizes the most important test results. With some exceptions of bad bumps or noisy pixels, the tested detectors seem to work correctly.

IV curves show leakage currents which reach a plateau at a reverse voltage below 5 V and at the plateau the measured currents are between 50 and 150 nA, reasonable values for pixel silicon sensors. The breakdown for these ATLAS08 sensors occurs at $\sim$ 30 V, a low value which is known to be related to the p-stop implant and which has been improved in subsequent batches.

The noise measured as a function of the bias voltage behaves as expected, with a initial reduction followed by a plateau. Comparing results of sensors with different electrodes configurations indicates that a higher sensor capacitance, proportional to the number of electrodes per pixel, produces a higher noise contribution, according to eq. 1.3.4. Tests done for this thesis did not use a cooling system and therefore the noise values could be overestimated with respect to measurements obtained with temperature and humidity controlled conditions.

Studying the behaviour of the device at different thresholds allows to optimize this value to enhance the detector performance avoiding to lose signals, in particular in case of charge sharing.

The measurements of charge collection as function of the bias voltage show that 3D detectors are able to collect all the deposited charge with a low reverse bias, dependent on the electrodes configuration. Absolute values of collected charge are not fully reliable because the conversion factor could not yet be measured with 3D sensors. A measurement with a gamma source is foreseen.

The procedure which has been set allows to study the most important characteristics of 3D detectors and will be used for the sensors from new batches which are expected.

Chapter 4

Laser Test

One of the most important parameter of a tracker detector is its pixel efficiency to detect the particles. This becomes particularly relevant for 3D sensors because the columns etched in the substrate determine a geometrical inefficiency for tracks entering the detector perpendicularly to the surface since no charge can be created in the empty columns. All the more so for the FBK detectors studied in this thesis, which have hollow electrodes that completely pass through the sensor. To increase the geometrical efficiency, electrodes can be made not passing through (CNM) or filled by polysilicon (SINTEF), and the final detector is usually placed tilted with respect to the crossing particles. Moreover geometrical efficiency can be gained at the sensor edges, implementing slim or active edges.

A way to measure a the efficiency of a detector is by means of a testbeam. A particle beam crosses a tracking device called telescope, usually formed by layers of silicon detectors which allow to reconstruct tracks with high spatial resolution. The Detector Under Test (DUT) is inserted in the telescope between the tracking layers and its efficiency is measured.

A different way to measure the pixel efficiency is by using a laser. Measurements which can be performed with this device are equivalent to those with a testbeam, with the advantage that they can be done in laboratory. The drawback is that a laser cannot penetrate metals and hence sensors with large metallized areas on the backside cannot be tested efficiently.

For this thesis I built a setup for laser testing of silicon pixel detectors. In this chapter the setup realization is described, explaning the problems found and the chosen solutions. First results obtained with such a setup are presented.

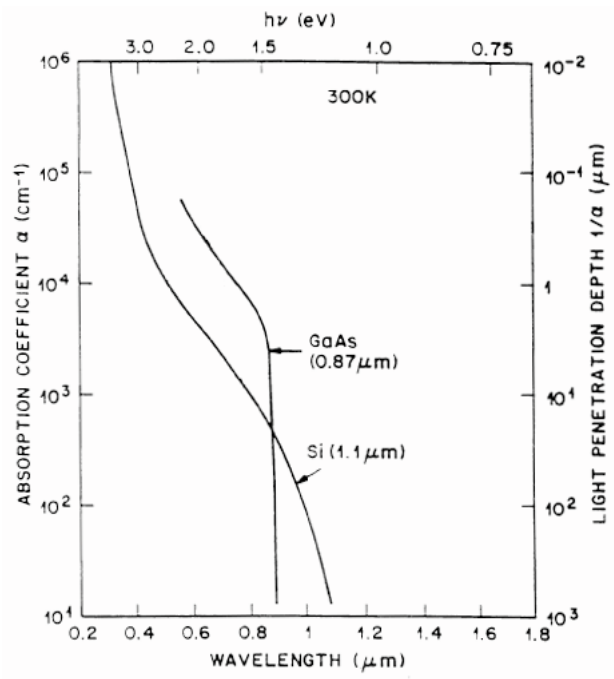

Figure 4.1: Absorption coefficient and light penetration depth ($d = 1/\alpha$) in Si and GaAs as a function of wavelength and photon energy [51].

4.1 Infrared absorption in silicon

The laser devices considered for the test setup use infrared photons. These photons have an energy which can become comparable to the one of the band gap in silicon. This has important implications because when the photon energy goes below this value the material becomes transparent to the light.

When studying the interaction of an infrared photon beam with matter, the absorption coefficient α is defined, which corresponds to the parameter μ of eq. 4.1.1. Figure 4.1 shows the absorption coefficient dependence on the photon wavelength for silicon and gallium arsenide. For photon energy close to the gap energy, the absorption probability becomes very small and is sensitive to thermal fluctuation.

$$I(x) = I_0 e^{-\mu x} \tag{4.1.1}$$

A photon with energy of the order of the gap energy, if absorbed, produces only one electron-hole pair. Therefore a high intensity beam, which can be provided by a laser, is needed to produce an appreciable signal. As shown in fig. 4.1 the absorption coefficient, and therefore the penetration in silicon, is strongly dependent on the laser wavelength.

If the intent is to simulate a MIP with the laser, the chosen wavelength must have a penetration depth higher than the sensor thickness. In this way the interaction probability of the laser beam photons is almost constant along the entire sensor depth. This is obtained in silicon with a 1060 nm laser, which has a penetration of the order of a millimetre, while lasers with shorter wavelengths are absorbed either at the surface or in the substrate.

4.2 Setup

Most of the instrumentation used for building the laser setup comes from a ten years hold setup for the test of CMS strip detectors. Modifications to the hardware and the software were necessary and will be described in the following.

4.2.1 CMS strip setup

The setup used for the CMS strip modules characterization is illustrated in fig. 4.2 [52]. The acquisition system was based on a VME crate controlled by a CPU RIO power PC. On it, a Front-End Driver (FED) was installed for module signal digitalization. The three VME boards in fig 4.2, called TTC-vi, TTC-vx and TTC-rx, were used for synchronizing signals and trigger. The VME-I2C interface was used for programming the Tracker Readout Interface Card (TRI-Card). On the VME crate also a laser board was installed which produced a laser pulse sent to the detector via optical fibre and collimated with a lens. This device, produced by INFN, will be described in sec. 4.2.2. Micrometric stages were used to move the collimating lens in the vertical direction (Mercury stage) for focusing and in the two horizontal dimensions (IntelliStage) for scanning.

The control of the whole setup was performed by two computers, one for the data acquisition and one for the slow control of stages and high voltage. Because of the synchronization required between the laser positioning and the acquisition chain, the two computers communicated via a TCP/IP protocol.

4.2.2 Laser board

The laser board was designed and produced in Turin by INFN. The device was realised to produce a laser signal with adjustable timing and intensity. The board has laser diodes with wavelength $\lambda = 850$ nm, which are commonly used for commercial applications. As mentioned in sec. 4.1, this wavelength provides a charge deposit only in the first few microns under the sensor

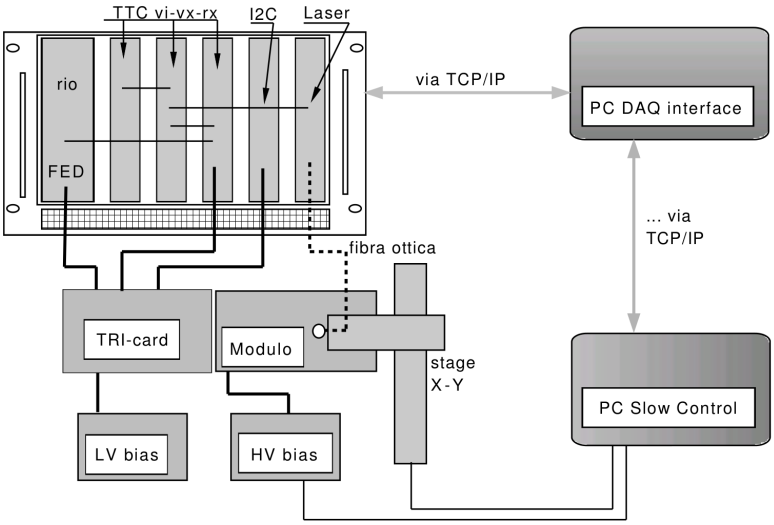

Figure 4.2: Schematic of the CMS strip module characterization setup.

surface and cannot be used for pixel characterization. Beside these optical outputs, electrical outputs are implemented for driving external laser diodes.

The laser board, shown in fig. 4.4, needs a trigger to produce the output (electric or optical). The trigger signal can be provided either in LVDS[1] or in NIM[2] logic. The latter input is chosen for the new setup.

The board is equipped with five output channels. Channels A to D have one electric and two 850 nm laser outputs. A and B produce an electric pulse of maximum amplitude 2 V, while C and D are limited to 1 V. Channel E has only the electric output with maximum amplitude 5 V, and was used to produce the backplane input[3].

For outputs A to D it is possible to set the amplitude and the width of the pulse and the delay between output and input signals. The amplitude is controlled by an 8 bits DAC which fixes the pulse height from 0 V to the channel maximum. The delay is adjusted with an 8 bits DAC in steps of 0.25 ns. The width can be set with 1 bit in fix or variable mode. The fixed mode has a width of 5 ns, while the adjustable mode gives from 9 to 30 ns in 8 step (3 bits). Other 2 bits are used to enable the two optical outputs of

[1]Low-voltage differential signal (LVDS) is a differential signaling system, which transmits information as the difference between the voltages on a pair of wires.

[2]NIM is an acronym for Nuclear Instrumentation Methods. In this standard the logic 0 is 0 V and the logic 1 is −0.8 V.

[3]For testing strips it is useful to induce charge in the sensor which is collected by the electrodes. To do that, a calibration signal is sent to the sensor backplane metallization.

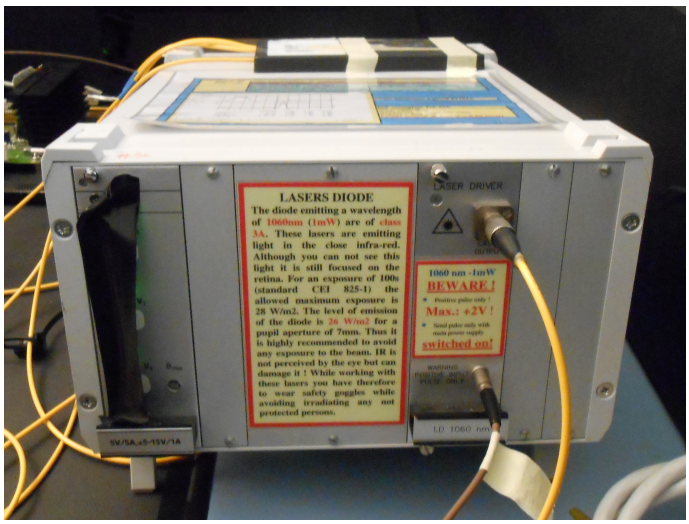

Figure 4.3: 1060 nm laser produced at CERN.

the channel. Therefore 22 bits are necessary for each channel. Other 3 bits are used to select the channel.

The bit can be set via manual switches, via VME or via RS-232. The communication mode can be selected with three jumpers installed on the laser board. The communication via manual switches requires a pulse signal to be sent with the strobe button of fig. 4.4.

For the laser setup the RS-232 interface has been chosen. Missing the manual, I derived the correct protocol from the schematics.

The communication via RS-232 needs an interface card. Communication is managed with 9 bytes. The better way to explain the sequence is to think in hexadecimal units, where a byte goes from 00 (0 in decimal) to FF (255). The left hand digit is used for enabling the data storage on the interface board (data are not yet saved in the laser board). Only if this digit is equal to 3 the data in the right hand digit are saved. Any other value is used to send a clear signal.

After the clear byte, the subsequent 7 bytes are used to send the data. The right hand digits of the 7 bytes are:

- First byte. First four amplitude bits.
- Second byte. Second four amplitude bits.
- Third byte. First four delay bits.
- Fourth byte. Second four delay bits.

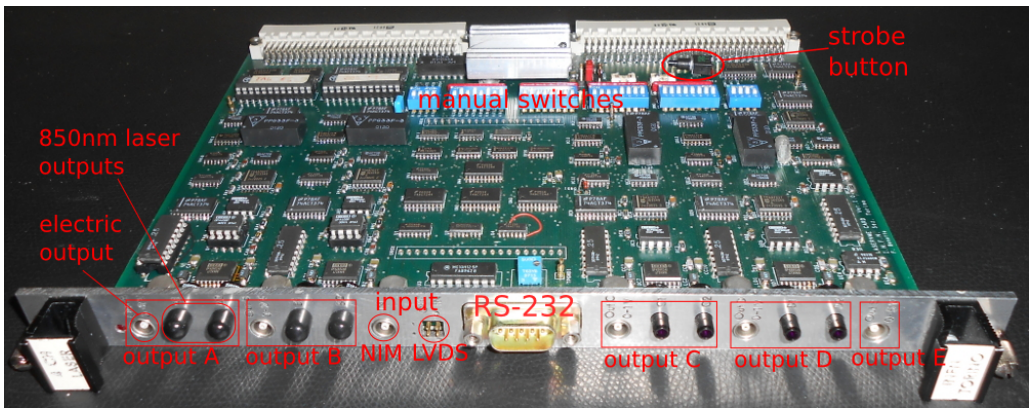

Figure 4.4: Laser board. In this picture the RS-232 interface board is not present.

- Fifth byte. First three bits for the variable width value and the fourth bit to enable the second laser output.
- Sixth byte. First bit to enable the first laser and second bit to enable the variable width mode. The other two bits are not used.
- Seventh byte. A value from 0 to 4 to select the channel from A to E for data saving.

Data sent via RS-232 are only saved on the interface board. To transfer them to the laser board a ninth byte must be sent whose value is $3X$, where X means any value from 0 to F. This byte is used to create the strobe signal which, as for the strobe button used in the manual configuration, saves data on the laser board.

This signal sequence can be managed by different softwares. The one chosen is LabVIEW, a system-design platform and development environment for a visual programming language from National Instruments. The easiest way to interface LabVIEW with external devices via RS-232 is the so-called VISA[4]. VISA is a standard I/O language for instrumentation programming. VISA is capable of controlling VXI, GPIB or serial (as RS-232) instruments and makes the appropriate driver calls depending on the type of instrument being used. Thanks to VISA properties, the way to send data to a device becomes very simple.

Studies on the characteristics of the laser board have been performed in [52]. For what concerns the electrical outputs, which are those of interest

[4]Virtual Instrument Software Architecture API (Application Programming Interfaces)

for the setup, the linearity between the set value, amplitude, delay or width, and the pulse displayed on an oscilloscope is excellent.

Thanks to the electrical outputs of the laser board, a 1060 nm laser (fig. 4.3), produced at CERN, is used for building the new laser setup. Only channel A and B are useful for driving the 1060 nm laser because it has been verified that the laser signal starts to be produced over ~ 1.5 V.

The electric pulse from the laser board is sent to the 1060 nm laser shown in fig. 4.3. The optical output is displayed on the oscilloscope thanks to an opto-electro converter TIA-950FC, shown in fig. 4.5. With this device the gain (1200 or 12000) and the coupling (DC or AC) can be set. For a better displaying, AC coupling and 12000 gain are used. Strong fluctuation have been observed in the optical pulse height produced by the 1060 nm laser.

Figure 4.5: Opto-electro converter TIA-950FC.

The laser behaviour is very much influenced by the ambient conditions. The setup is presently built in a room where temperature and humidity conditions cannot controlled.

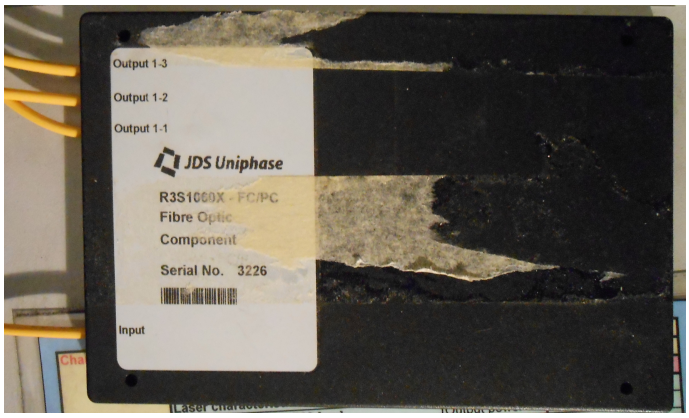

Figure 4.6: Optical splitter R3S1060X-FC/PC

To avoid problems due to laser fluctuation, the laser pulse height displayed on the oscilloscope is taken as reference.. For this reason, a three channel optical splitter R3S1060X-FC/PC (fig. 4.6) is used to split the laser output, sending a line to the oscilloscope and another one to the sensor for the measurements. In this way it is possible to monitor in real time the laser output.

4.2.3 X-Y-Z stages

For the planned measurements, laser collimated light needs to be moved in tree directions.

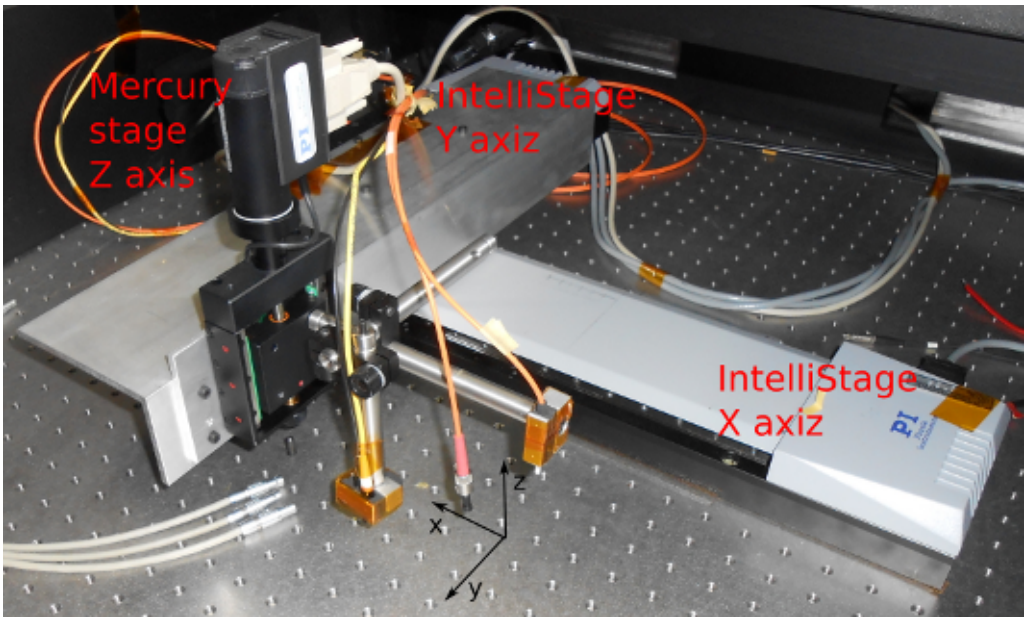

Figure 4.7: Stages for 3-dimensional motion.

The system IntelliStage, shown in fig 4.7, is a system formed by two micrometric motion stages produced by Physik Instrumente [53]. These stages have a design resolution and a minimum incremental motion of 0.1 μm with two different travel ranges: 306 mm for x and 204 mm for y.

The IntelliStage control is performed via RS-232. Thanks to an address for each stage, the two stages are controlled with the same cable. Therefore, commands sent from the computer consist in a string where the first byte must contain the address number. After addressing, two characters indicate the action required, followed by the required number (steps for motion, velocity or acceleration). Commands must not contain spaces and end with a line feed character.

The z axis motion is performed by a Mercury DC-Motor Controller [54] which interfaces the computer to a micropositioning motor. The interface used is the RS-232 and the command strings are similar to those of the IntelliStage. The Mercury DC-Motor Controller must be addressed once at the beginning to set the motor in ON state. Each command must be followed by a carrier return character.

While for the IntellyStage a step correspond to 0.1 μm, for the z axis the conversion from steps to spatial shift needs to be measured because it depends on the characteristics of the micropositioning motor device connected to the Mercury DC-Motor Controller. From measurements, it is found that a shift of 0.1 μm corresponds to 11.8 steps.

As for the laser board, 3-dimensional motions with LabVIEW with VIs programs which I wrote to this purpose.

4.2.4 Pulser

To produce a pulse the laser board needs to receive a NIM trigger signal, therefore a pulser is needed to temporize the chain. An Agilent 81110A pulse and pattern generator, shown in fig. 4.8, has been chosen to this purpose.

Figure 4.8: Agilent 81110A front panel.

The timing of the setup is very important for scanning the pixel area. Knowing the laser beam position and the number of pulses sent by the Agilent 81110A, it is possible to reconstruct a map of the pixel efficiency by measuring the number of recorded events.

To perform the scan, an automatic procedure has been prepared, which controls the device remotely via GPIB. To send the desidered number of burst, I created a LabVIEW VI which communicate to the device through the GPIB drivers. The program switches temporarily the device to local mode, then emulates the hardware command which sends the burst and finally switches back the device to remote mode.

To verify the correct behaviour of the pulser a FLUKE PM6680B counter is used, which confirms that the counted number of pulses is that expected.

4.2.5 External trigger for PSI board

To use the laser setup also the data acquisition must be synchronized by an external trigger in coincidence with the laser pulse. The data acqusition program can also work with an internal random trigger.

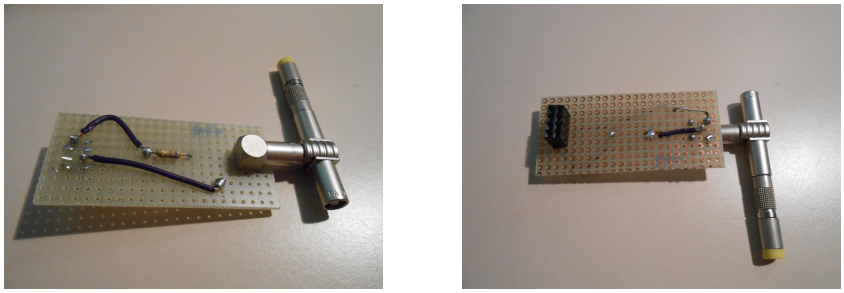

(a) Top side. (b) Bottom side.

Figure 4.9: Trigger adapter.

The external trigger, brought with a LEMO[5] cable, needs to be given to a dedicated connector of the PSI board. For doing this I realized a small adapter (fig. 4.9), based on a design by the Desy group.

The signal of the external trigger is a TTL[6] whose logic 0 is 0 V and logic 1 is 3.3 V. The delay between the trigger signal received by the PSI board and the time when the event is requested to the ROC is set by the WBC. This value depends on the particular board setting, like cable, adapters and so on. Before data taking a WBC scan must be performed to set the correct delay.

4.2.6 Final setup configuration

All the devices described in the previous sections have been used for assembling the final laser setup, which is shown in fig. 4.10. The setup has been designed for being as much as possible independent on the tested detectors, in particular in view of the fact that a new digital readout chip is foreseen for the tracker update. In the built setup the only connection between acquisition and laser systems is the trigger signal, ensuring a high versatility.

The timing of the entire setup is provided by the Agilent 81110A which creates a NIM signal. This signal is sent to a fan-in fan-out installed on a NIM crate which makes two copies of the signal: one is used for the trigger, the other for the laser chain.

[5]LEMO is a standard connector for coaxial cable.
[6]Transistor-Transistor Logic

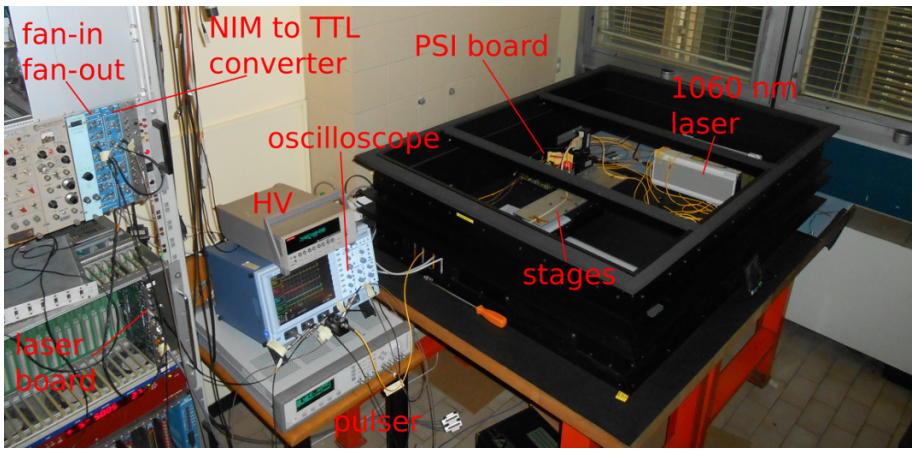

Figure 4.10: Laser setup.

For PSI board triggering, the first signal is converted to a TTL signal with a NIM to TTL converter installed on the NIM crate, which provides the correct trigger signal expected by the PSI board. The laser timing signal is sent to the laser board, which produces the pulse for the 1060 nm laser, whose optical output is then deliverd for the detector measurement.

4.3 LabVIEW control and timing

For controlling the setup, I wrote a series of VIs which can be divided in two main projects: the first one manages the laser board, while the other one controls motion, pulse and scan. The choice has been to keep the two projects separated in order to have more flexibility.

4.3.1 Laser board control

The VI for the laser board sets the board parameters following the protocol. The Front Panel[7] (a screenshot in fig. 4.11) is divided in two parts: one for sending data to the laser board and the other which keeps in memory data saved on the laser board.

In the part dedicated to sending data, for each channel A to E of the board it is possible to set amplitude, delay, to switch to variable width and

[7]LabVIEW VIs have two windows: one is te GUI (Graphical User Interface) called Front Panel which contains indicators and controls, and the other is the Block Diagram where there are instruments for data managing which make the operations with controls and indicators.

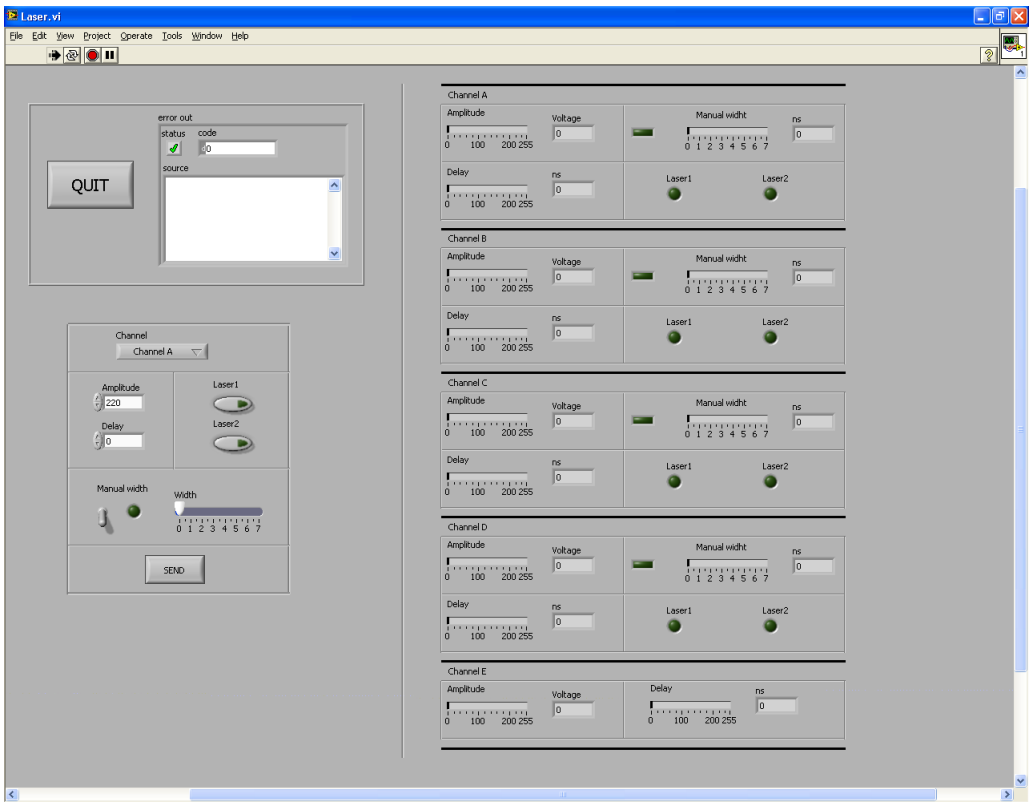

Figure 4.11: Screenshot of the laser VI Front Panel. On the left there are the controls while on the right the data saved on the laser board are kept in memory.

choose its value and to turn on laser 1 or 2. Selectable values for amplitude and delay are expressed in 8 bit units, which means from 0 to 255. Following the protocol described in sec. 4.2.2, these data must be split into two values of 4 bits. With a slide it is possible to set the 3 bits (from 0 to 7) for the width value, once the variable width option has been switched on.

The right part of the panel is used to keep in memory the last data sent to the device. For each channel the GUI shows: the amplitude and the delay in DAC units and converted in V and ns, respectively; the pulse width in ns and if it is set in variable mode; which one of the two lasers is on. For channel E only the amplitude and the delay can be set.

Besides creating the data sequence described in sec. 4.2.2, the Block Diagram resets all laser board parameters and disables the laser optical outputs. This happens when the VI starts and when it is closed, in order not to leave the laser board in an unknown state.

4.3.2 Stages and pulser control and pixel scan

The VI for controlling stages and pulser is based on the Queued State Machine (QSM) concept. The QSM architecture allows programming LabVIEW's event structure to send commands for asynchronous processing in a parallel loop, so that event cases can exit code execution quickly and avoid GUI lock up. In other words two loops are created: one for user interface, which creates commands, and the other, the consumer loop, which handles these commands. The two loops are joined together by a LabVIEW item called *Queue*. States can be created by different VIs while command execution must be handled only by the consumer loop to avoid data loss.

Figure 4.12: Screenshot of the stages and pulser control VI Front Panel.

The Front Panel shown in fig. 4.12 has a tab menu to perform three principal operations: stage control, burst control and pixel area scan. In addition, a message indicator shows the operation that the consumer loop is performing. For quitting the devices a dedicated button is present. Pushing it, the VI waits for the previously programmed operation to finish and then stops all loops. An emergency stop button is also present. Pushing it the VI cancels queued operations, stops stage motion and disables the pulse output. At the same time, by means of a global variable, the laser VI described above (sec. 4.3.1) is also closed, ensuring the complete switch off of the setup.

The stage control allows, either for IntellyStage or Mercury stage, to

get information concerning the most important parameters such as position, velocity or acceleration. To avoid potential dangerous modification of the work parameters, the only value which can be set from the user interface is the position, expressed in 0.1 μm units[8].

The tab dedicated to the pulser control allows to set a limited number of burst parameters to avoid unintentional modification of the pulse characteristics, which can damage the timing chain. In particular the period, the pulse width and the number of pulses per burst can be chosen. From the GUI it is also possible to enable or disable the pulse output and to send a single burst. The other pulse parameters are set in the Block Diagram and are not alterable during VI running.

The scan tab allows to produce a series of instructions for scanning with the laser the area of the sensor. Step length in x and y and the total number of points can be given. When a scan is started, a window asks where to save the file containing the information to be used for data analysis. In each point, a burst is sent from the pulse to the timing chain and at the end stages move to the next position. Iterating it, I implemented a serpentine motion to scan the pixel area.

4.4 Laser setup test with a planar pixel sensor

Testing the laser properties and trying to find the best working parameters with the available 3D sensors is not very convenient. In fact, these devices have a metallization grid on which the laser is reflected and have inefficient zones at the electrodes. For these reasons, a preliminary setting up has been made with a CMS planar pixel detector, which does not have inefficient regions and has the backside not metallised. The sensor has a thickness of 280 μm and it is read out with the PSI46 chip [55].

Tests made with the planar sensor allowed to fix the trigger delay, and verify if there were timing problems. In addition, laser parameters such as amplitude and width of the signal and the lens distance from the sensor were optimised. Finally, since the planar sensor is bump-bonded to the same readout chip used for 3Ds, some parameters of the amplification chain have been studied.

[8]This value is the minimum step for IntelliStage. To avoid confusion, also the Mercury stage has been expressed in the same units.

4.4.1 Trigger delay and timing control

The first step of the synchronization is the WBC scan (sec. 4.2.5) for setting the correct delay. The procedure provides an histogram with the number of non empty entries as a function of the WBC. The correct delay is the one for which the higher number of entries is obtained.

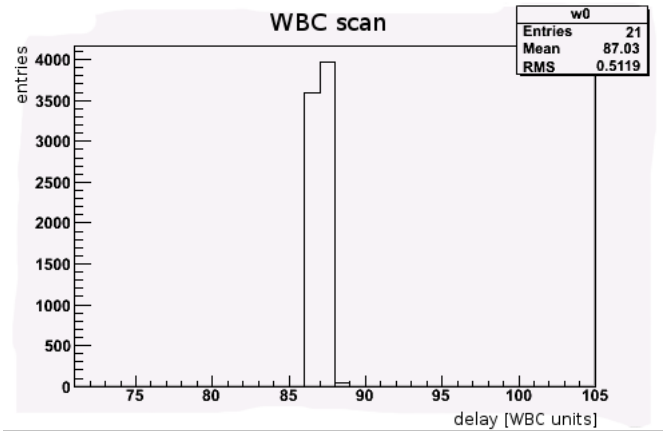

Figure 4.13: WBC scan result obtained with the planar pixel sensor.

The measurement has been done for the planar sensor and the result is shown in fig. 4.13. The WBC value to which corresponds the highest number of entries is 87. The value should only depend on the setup and not on the detector under test. The scan has been anyway repeated for a 3D sensors, obtaining, as expected, the same value.

A check was made to monitor possible trigger loss. To do this an acquisition was run with a continuous trigger and the distribution of the difference between timestamps of subsequent events was plotted. The trigger period chosen was 1 ms and hence the distribution is expected to be centred around that value. Figure 4.14 shows the result. One can notice that the number of overflows or underflows is 0, which confirms that no triggers are lost once the acquisition is started. A small bias can be seen in the plot, but the deviation from the expected value is less than 0.5%.

It was also checked if the number of triggers sent corresponds to the number of triggers acquired. This is a way to monitor possible data losses at the beginning of the acquisition. Repeating several acquisitions with different numbers of triggers sent, it was verified that the number of registered triggers always differs by one event. This happens because the first trigger is used to start the acquisition. This is not a real problem, but needs to be taken into account during the data analysis.

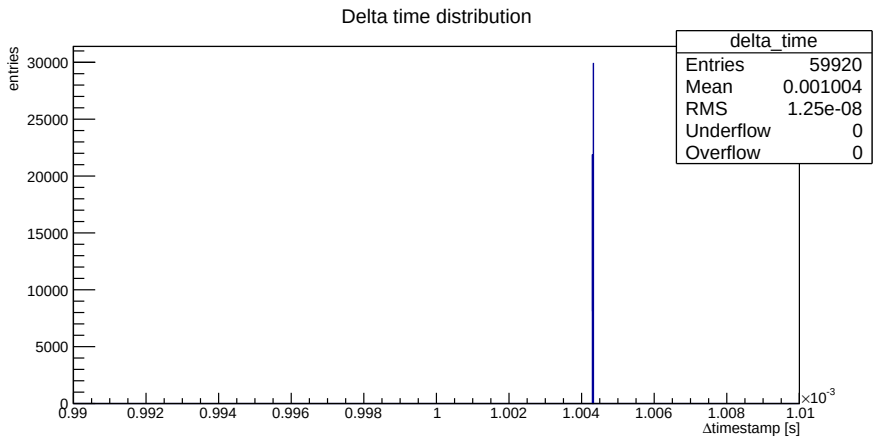

Figure 4.14: Distribution of the difference between timestamps of two subsequent events.

4.4.2 Focusing

Changing the distance between the focusing lens and the sensor it is possible to select the spot dimension of the incident laser beam.

After several measurements it was clear that trying to adjust the focus without modifying the laser amplitude was not possible. In fact, a more focused beam corresponds to a more intense deposition of charge, which saturates the pixel readout.

To find a reasonable compromise, a different strategy was chosen: fix the distance to the focal length and then adjust the laser amplitude. The nominal lens value is 12 mm, which determines a spot dimension of 10.9 μm at 50% of intensity. The vertical stage was used to find the lens position where only one pixel was hit.

4.4.3 Amplitude and width of the 1060 nm laser output

Since the purpose of using a 1060 nm laser is to simulate a MIP, the time during which the charge is deposited must be as short as possible to reproduce the charge deposited by a relativistic particle. The shorter available laser width is 5 ns.

The amplitude adjustment is more complicated because a too high pulse saturates the amplification chain and cannot be observed. The saturation effect is visible in the chip map of fig. 4.15, where an unfocused laser beam is sent to the chip. The laser beam has a gaussian intensity shape with the

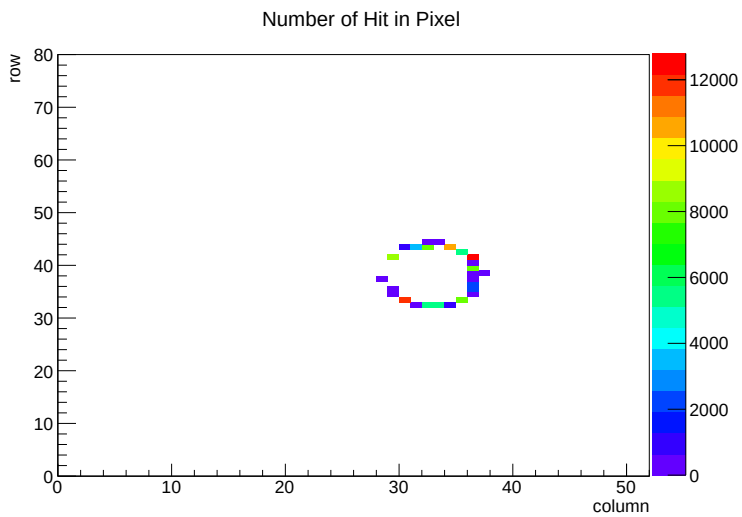

Figure 4.15: Pixel map resulted from an acquisition with an unfocused laser beam. The empty circle is an evidence of saturation.

spread dependent on the focusing. A full circle of hit pixels is expected while only pixels on the circle edge are hit (fig. 4.15). This is because the too intense beam in the central region "kills" the readout of the corresponding pixels.

With a 1060 nm laser, part of the photons can pass through the sensor and be reflected back by the readout chip metallization. An example is shown in fig. 4.16, where the laser beam, already focused on a single pixel, is increased in amplitude. The effect of the reflection is that a second pixel starts to be hit, with an increasing number of recorded events, until the first pixel does not register hits anymore due to the saturation problem and only the second pixel gives a signal.

Various tests have been performed changing the laser intensity. The results indicate that the displayed signal on the oscilloscope must be lower than 130 mV and higher than 60 mV to produce a signal in the detector. The sensibility of the laser board is not sufficient to make a fine tuning between this two values.

4.4.4 Parameters for the PSI46 amplification chain

Increasing the laser amplitude, the mean collected charge is expected to increase. Once found the amplitude upper limit to avoid saturation and reflection, the best intensity which reproduces the charge deposited by a MIP was searched.

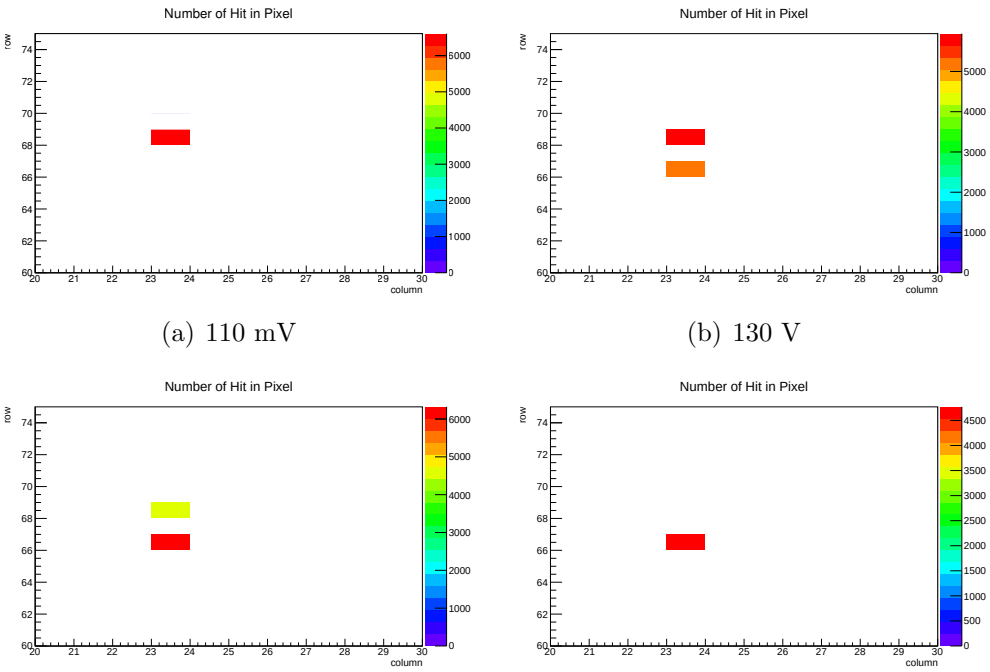

(a) 110 mV (b) 130 V

(c) 140 mV (d) 210 mV

Figure 4.16: Effect of reflection increasing the laser beam intensity. The value of the laser intensity is derived from the pulse height displayed on the oscilloscope.

In these conditions of amplitude, a signal with mean value higher than $65\,Vcal$ ($\sim$ 4200 e$^-$) is not reached. The effect is due to the time in which the charge is deposited. In fact, for a MIP the ionization happens in few picoseconds, while the signal of the laser has a duration much larger, in particular it is comparable with the charge collection time. This causes a signal at the amplifier input with a shape lower and longer.

To produce a sharper shape, a faster laser signal is needed. Since this was not available, I tried to adjust a few parameters of the amplification chain of the PSI46 PUC to get an amplified sharper signal, sampling the value as much as possible near the peak.

The first DAC which can be modified is the $VHldDel$. With the laser signal fixed to 110 mV, this DAC value is scanned from 0 to 255 and the result is plotted in fig. 4.17. As one can see, even with the maximum delay the peak pulse is not reached.

The second DAC which can be modified is the $VrgSh$, which changes the shape of the amplified signal. Since this DAC fixes the gate voltage applied to

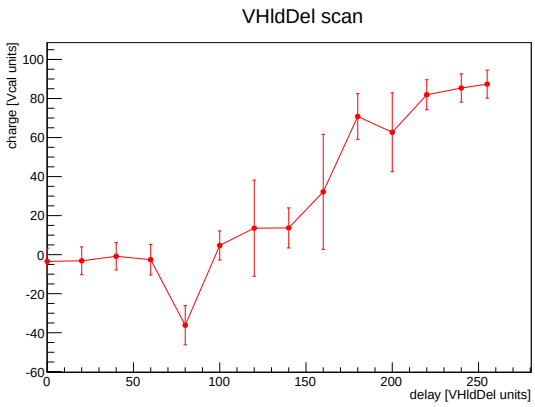

Figure 4.17: $VHldDel$ scan result obtained with the planar pixel sensor.

the PMOS transistor used as feedback resistance of the shaper, by increasing $VrgSh$ the resistance increases and the signal shape becomes sharper. The values which have been tried are 0, 7 and 15. As shown in fig. 4.18, the best value for $VrgSh$ is 7 because the signal is higher.

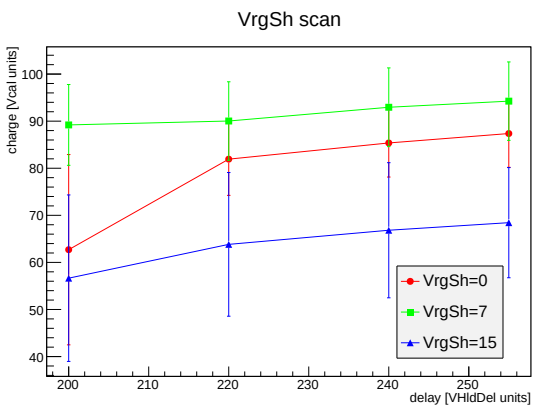

Figure 4.18: $VrgSh$ scan result obtained with the planar pixel sensor.

To be more precise, after changing $VrgSh$ a new pulse height calibration should be performed. This was not done because for this optimization a relative measurement of the charge collection was sufficient.

4.5 Test with a 3D pixel sensor

After the studies of the laser setup done with the planar sensor, some measurements with the 3D sensor 2E_11 have been made. Since studies of

focusing and laser amplitude are more difficult with this device due to the inefficiency of the columnar electrodes and the backplane metallization, the results of the pixel scans are used for finding the best parameters. The metallization grid on the sensor backplane, shown in fig. 4.19, has a width of ~ 50 μm and hence the visible pixel area is reduced to 50×100 μm^2.

Scans have been performed on an area of 200×300 μm^2 for ensuring the coverage of at least one pixel. The scan is done in 5 μm steps, since this value almost corresponds to half of the spot diameter.

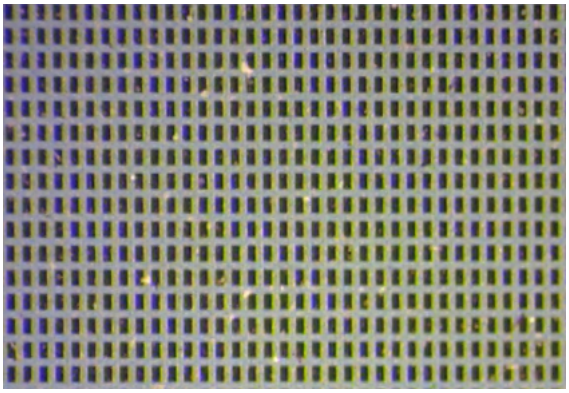

Figure 4.19: Picture of a 3D sensor backplane.

A first consideration is that, due to the shorter time collection of 3D with respect to planar sensors, the influence of the time width of the laser output should be less strong. The amplifier DACs have thus been kept to the standard values, $VHldDel = 160$ and $VrgSh = 0$.

The effects of a too high intensity and not well collimated laser beam are shown in fig. 4.20(a), where the result is the opposite of what expected since the metallization region is observed, while the sensitive part of the pixel is empty. This is due to the saturation of the readout chain, similarly to what has been presented in fig. 4.15.

To measure the expected efficient regions and not the metallized ones, the laser intensity needs to be reduced. The reasonable map shown in fig. 4.20(b) has been obtained with a laser intensity corresponding to ~ 10 mV on the oscilloscope. However the expected right angles of the pixel area cannot be seen because of the not precise focusing. A more fine tuning of focusing and laser amplitude allowed to obtain the measurements shown in fig. 4.21 for the efficiency (b) and the charge collection (c), which geometrically compares very well with the picture of the scanned area.

Still, the expected column inefficiency is not yet visible, probably due to a too large laser spot. However, the latter cannot be further reduced for the

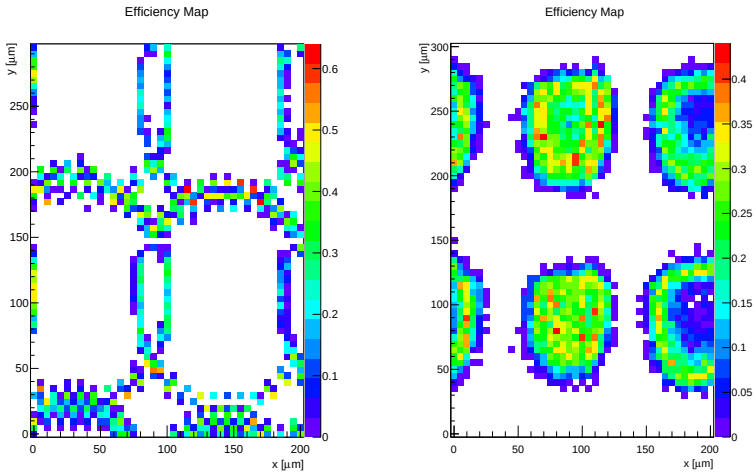

(a) (b)

Figure 4.20: Efficiency maps from scans made with (a) a too intense unfocused laser and (b) an unfocused laser with the correct intensity.

lens mounted in the setup.

For improving the granularity of the scan, a more focusing lens is used, with a focal length of 8 mm and a minimum spot diameter of 5.5 μm. After a few course scans for finding the correct vertical position and the amplitude of the laser, the scan of an area of 100×160 μm^2 in steps of 2.5 μm has been carried out.

The efficiency map for a single pixel of the 2E_11 detector is shown in fig. 4.22(a). Two holes corresponding to the columnar empty electrodes are now visible, with a distance between them and a diameter comparable with the layout of this sensor shown in fig. 4.22(b). The observed columns are not centred in the visible pixel area, however, observing the sensor at the microscope, it is possible to see that the metallization is slightly misaligned. This is visible in the picture of fig.4.23, looking at the displayed metallization with respect to the ohmic columns.

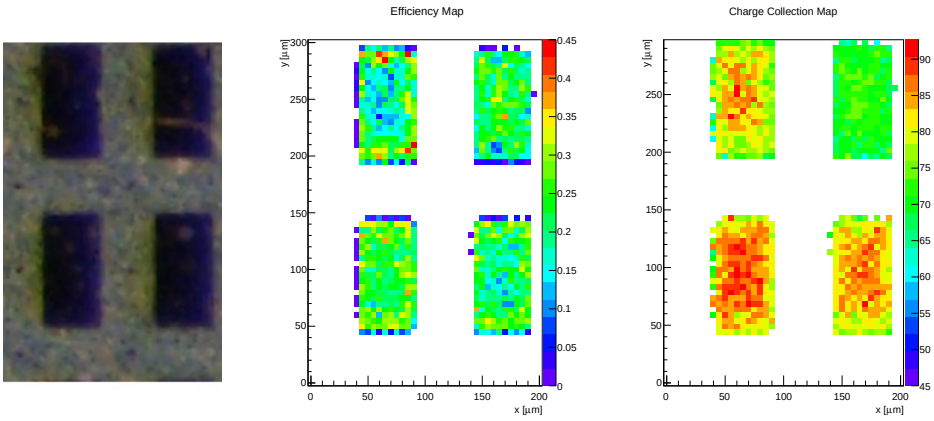

(a) Picture of the scanned area.

(b) Efficiency map.

(c) Charge collection map.

Figure 4.21: Result of a scan of a limited four pixels region of the 2E_11 sensor. The collected charge is expressed in $Vcal$ units.

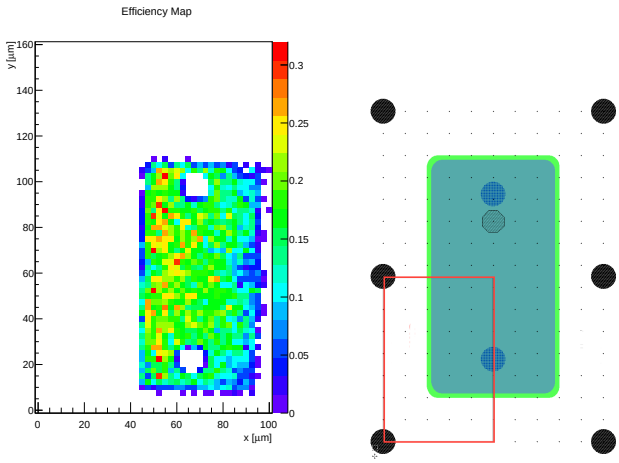

(a) Pixel efficiency map.

(b) Layout of the pixel.

Figure 4.22: Result of a scan for 2E_11 sensor with the best focusing lens. The collected charge is expressed in $Vcal$ units.

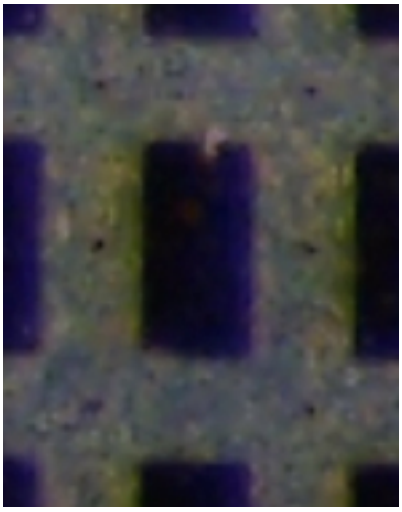

Figure 4.23: Picture of the misalignment between metallization grid and columns.

4.6 Conclusions on laser test

A new laser setup for testing silicon pixel sensors was prepared, partially using instrumentation inherited from the test setup of the CMS strip modules. The new setup is temporized by a pulser which at the same time controls the trigger for the data acquisition and the timing of the laser beam. Photons have a 1060 nm wave length, chosen because such a laser beam well simulates the charge deposition of a MIP.

The control of the entire setup was realized with LabVIEW programs, divided in two projects to keep separate the control of the laser board from the one of stages, pulser and scan procedure. Security operations are automatically performed to avoid dangerous situations.

Various tests were performed on the setup timing: the trigger latency can be well optimized and there are no evidence of trigger losses.

Focusing and intensity of the laser beam were optimized for planar sensors. Such two parameters were found not to be independent, due to the saturation of the pixel amplification chain when a too large charge is deposited.

The available laser has a charge deposition not shorter than 5 ns, much longer than the charge deposition time for a MIP which is of the order of a picosecond. A laser signal so long with respect to the charge collection time has a negative influence on the shape of the amplified signal. Even modifying a few readout parameters, to obtain a sharper signal, more similar to that of a MIP, the measured charge deposition is less than half of that obtained for a MIP, with a loss of efficiency. The use of a picosecond laser beam should probably attenuate this problem.

Considering 3D sensors, measurements showed that the amplitude of the laser needed to produce a recordable charge deposition is one order of magnitude lower than the one used for planar sensors, probably due to the faster time collection of 3D sensors.

Once the beam intensity and the focusing of a new lens with a smaller spot were adjusted, the efficiency map of a single pixel could be measured, which shows the expected inefficiency regions in coincidence with readout electrodes. This result demonstrates the capability of the new laser setup to study the efficiency of pixel detectors with the resolution of a few microns.

Chapter 5

Conclusions

Novel 3D silicon pixel sensors are characterized by columnar electrodes which are etched perpendicularly through the bulk. Depending on the production, columns can reach the opposite bulk surface or stop few tents of μm before.

Because of their radiation hardness, 3D sensors are considered as very promising candidates for the HL-LHC upgrades of the inner layers of the ATLAS and CMS tracking detectors. Thanks to the qualification effort of the ATLAS 3D Collaboration, 3D sensors will be used for the first time in a high energy experiment as part of the Insertable B-Layer of the ATLAS pixel detector.

To study the performance of these sensors when coupled to the CMS readout, a laboratory test procedure was set up for this thesis work. The relevant steps are: chip calibration and functionality tests, IV curve, noise vs bias voltage, detector behaviour at different thresholds, and charge collection vs bias voltage.

To all these tests a laser measurement was added. To this purpose, a complete setup was prepared and commissioned as part of the thesis work. The final result is an instrument, controlled by LabVIEW, which scans the pixel area for efficiency and charge collection measurements, with a spatial resolution of a few microns. Data acquisition and setup control systems are menaged separately to ensure flexibility, with the only connection represented by the trigger signal.

With the established procedure, sensors belonging to an early FBK production were analysed. Most significant results are expected from incoming sensors from newer batches.

Appendix A

Calibration procedure

Before starting the calibration procedure, the PSI board needs to be connected to the computer hosting the relative software via USB cable and the communication must be enabled with an apposite script. The analysis program ROOT has to be installed for using the calibration program.

The PSI board functionalities are managed by the *psi46expert* program, which is a ROOT-based software developed at PSI. This program allows, through a graphical user interface, to perform different tests on the detector, to set readout chip DACs and to run the calibration procedure.

To calibrate a chip, a dedicated folder containing the configuration files with the initial chip settings is needed. Depending on the specific connection of the chip carrier board with the PSI board, timing must be optimized modifying delay parameters which are present in these files, in particular in tbParameters.dat, where clk, sda and ctr are set. These parameters fix the delay, expressed in ns, for ROC clock, data flow and trigger, respectively.

Calibration consists of four steps, and for each step the results are saved in a ROOT file with a specific name. With the configuration files in the singleROC## directory, steps are:

Pre-Test. It makes the setting of the most important DACs of the device and verify the address levels of the chip. Furthermore it sets the $CalDel$ and $VThrComp$ for the subsequent calibration procedures.

```
./psi46expert -dir singleROC## -r PreTest.root -log PreTest.log
```

Full-Test. It checks the main functionalities of the chip: address decoding, pixel response, bump-bond quality, test of $TrimBit$ DAC, and it makes the S-curves for the noise measurement.

./psi46expert -dir singleROC## -r FullTest.root -log FullTest.log

Trimming. It performs the trimming procedure described in sec. 3.3.5. The target threshold of the procedure is set in testParameters.dac by the TrimVcal value.

./psi46expert -dir singleROC## -r trim.root -log trim.log

Pulse Height Calibration. It calibrates the pixel response as described in sec. 3.3.8. It requires the target threshold at which the trimming has been previously done (60 $Vcal$ in this case).

./psi46expert -dir singleROC## -r Ph_cal.root -log Ph_cal.log -trimVcal 60

Dedicated ROOT macros are used for fitting S-curves and pulse height calibration data to obtain noise information and conversion from registered ADC value to deposited charge, respectively.

At the end of the calibration, a ROOT macro summarizes in a single page the most important information on the chip behaviour.

Appendix B

Data taking procedure

Data acquisition through the PSI board is performed by the program *takeData*, which uses ROOT libraries. Before any acquisition, the chip has to be already calibrated. For running *takeData*:

./takeData -l -dir singleROC## -trimVcal 60

where the directory singleROC## contains the calibration files of the chip and trimVcal indicates the threshold in $Vcal$ units set by the calibration procedure (in this case 60 $Vcal$). If -l is used the internal trigger is enabled, which is generated randomly by the FPGA; omitting -l, an external trigger is expected.

takeData has a graphical user interface where the parameters for the acquisition can be set, in particular duration of the acquisition and WBC, i.e. the trigger latency in LHC bunch crossing units of 25 ns.

Collected data are saved in a binary file, which is then converted in a ROOT Tree:

./convert_to_tree -l -r ⟨run number⟩

For data analysis different macros have been written. In particular, source test data are studied with the macro *pulseHeightMain.C*, while for laser scan data are analysed with *scan_analysis.C*.

Appendix C

Detector behaviour with threshold

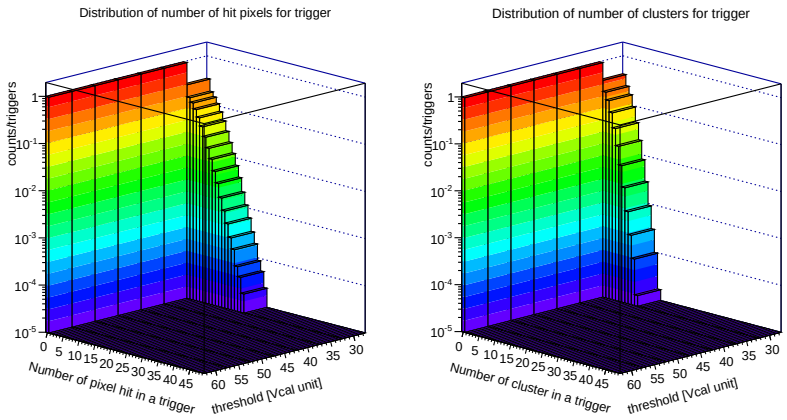

(a) Without source.

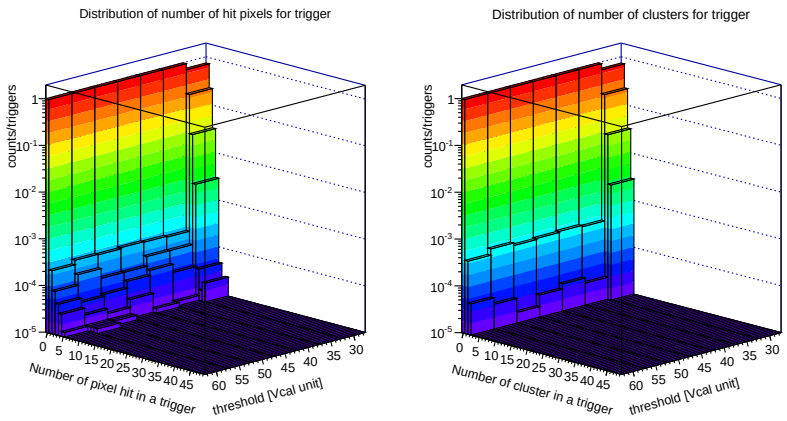

(b) With source.

Figure C.1: Behaviour of detector 1E_7 at different thresholds

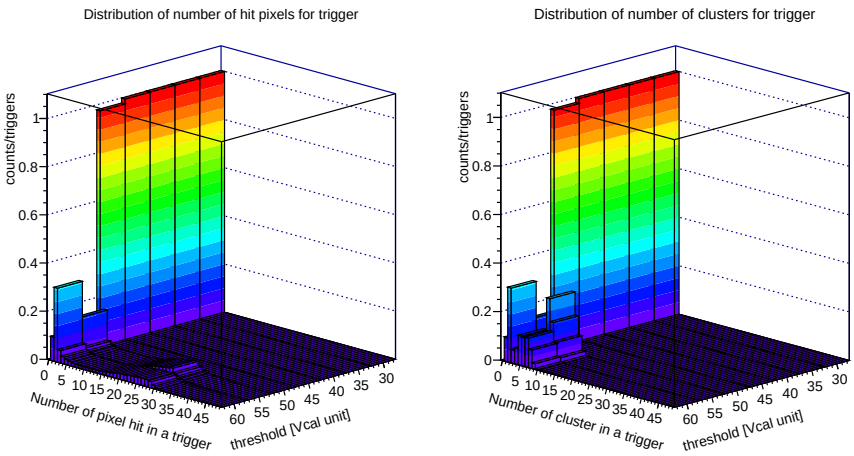

(a) Without source.

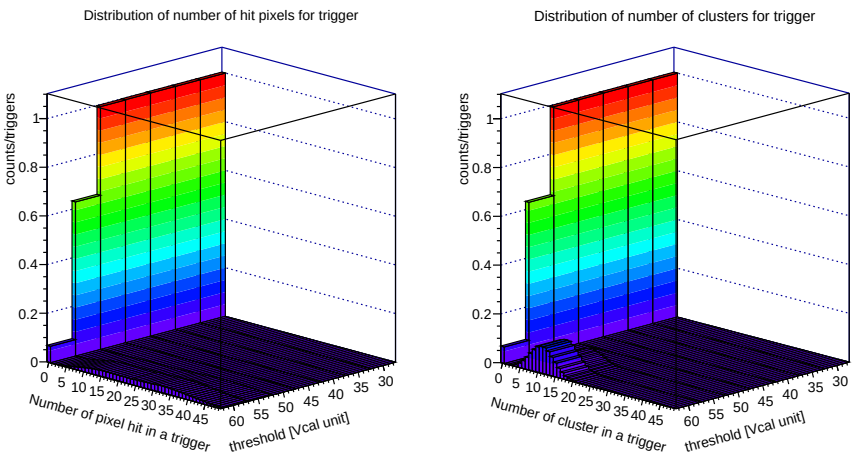

(b) With source.

Figure C.2: Behaviour of detector 2E_10 at different thresholds

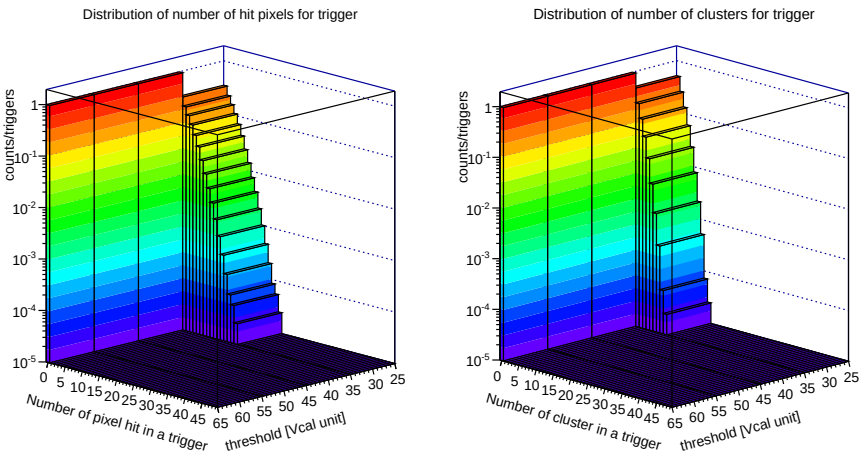

(a) Without source.

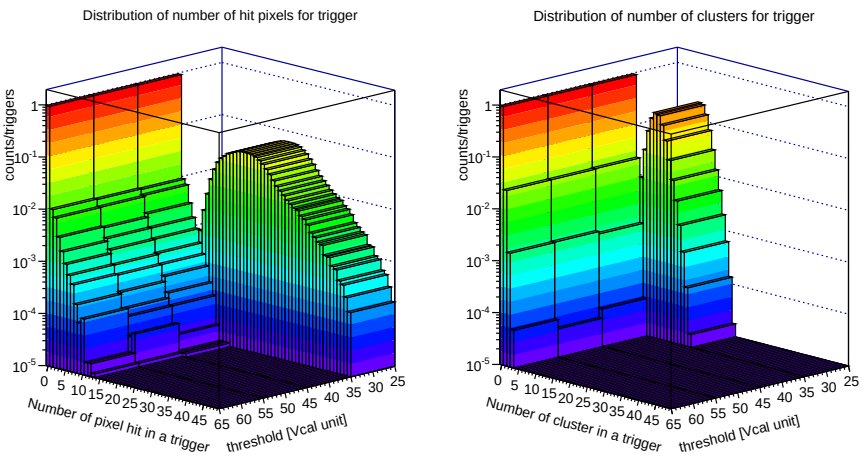

(b) With source.

Figure C.3: Behaviour of detector 2E_11 at different thresholds

Appendix D

Testbeam threshold measurements

Several prototypes of 3D and diamond pixel sensors have been tested on a beam of 120 GeV protons at the Test Beam Facility (FTBF) of the Fermi National Accelerator Laboratory (FNAL) in Batavia (Illinois, USA) [56]. The final goal is to compare the performance of the prototypes before and after irradiation, in order to understand if the proposed technologies can stand the high fluences expected at the HL-LHC with the required design specifications.

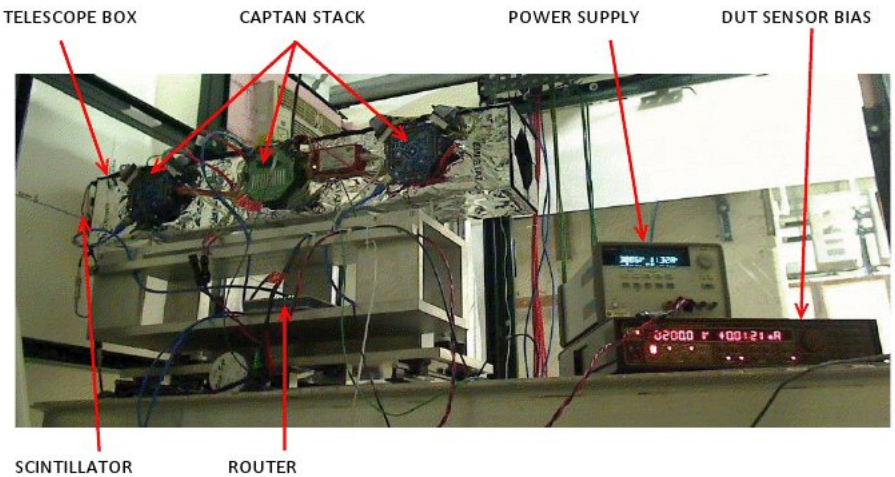

Figure D.1: MTest pixel telescope.

Detectors Under Test (DUTs) are placed in a telescope which performs the tracking. The structure, shown in fig. D.1, consists of height layers of

CMS silicon pixel detectors. A scintillator placed downstream behind the telescope generates the trigger signal.

For a better resolution, the tracking layers are rotate of 25° with respect the two directions perpendicular to the proton beam. A tree-dimensional view of the telescope structure is shown in fig. D.2. As one can see, the axis with respect to which layers are rotated is the one perpendicular to the shorter pixel side. The result is a tracking resolution of $\sim 6\ \mu$m.

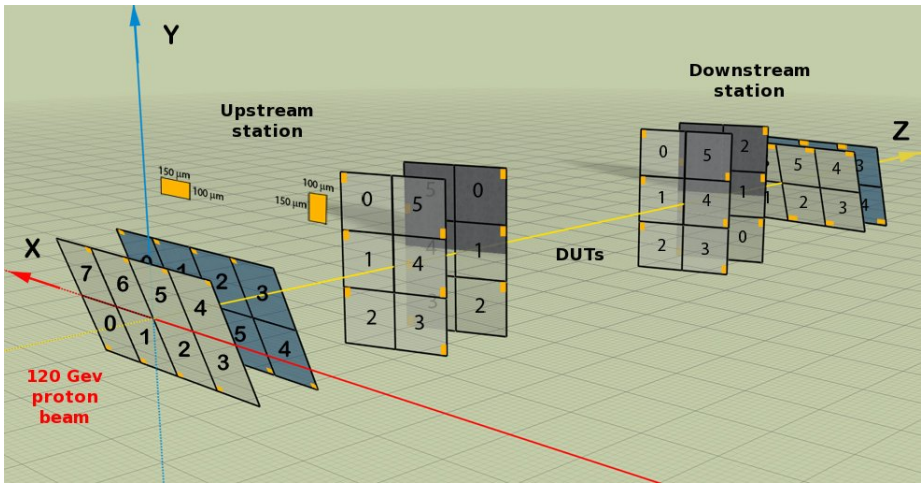

Figure D.2: Three-dimensional representation of the telescope tracking layers.

In each run, two DUTs can be tested at the same time. Their position is in the middle of the telescope, as illustrated in fig. D.2. Their readout, as for the telescope detectors, is performed with the CAPTAN (Compact And Programmable daTa Acquisition Node) data acquisition system [57].

Testbeams of October 2011 and April 2012 have tested 3Ds produced at FBK and CNM before and after irradiation. Irradiation was performed with 800 MeV protons at Los Alamos National Laboratory (USA).

I have analysed the threshold of the 3D detectors which were tested. The way to measure this value is to send a series of increasing amplitude test signals to the PUC amplification chain: the amplitude for which the efficiency is 50% is the threshold.

For these measurements the $Vcal$ DAC is set in high range and in this case $1\,Vcal = 455$ e$^-$. The use of this range do not provide enough granularity to justify a fit with an error function (eq. 3.3.3), hence it is chosen to trace a straight line from the last $Vcal$ for which no hit is registered to the first one for which all signals are seen. The middle point of this line is an estimates of the pixel threshold. The procedure is shown in fig. D.3.

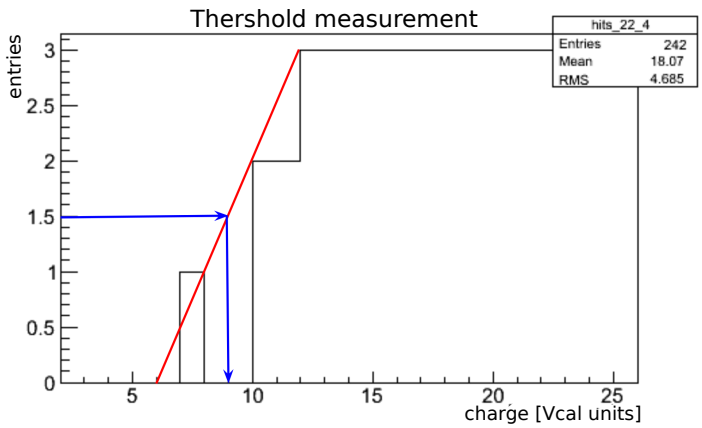

Figure D.3: Method used for determining the threshold of one pixel.

Iterating the procedure for all pixels in a chip, it is possible to get the threshold map and the distribution, as shown in fig D.4. The results for all 3D sensors are summarized in table D.1.

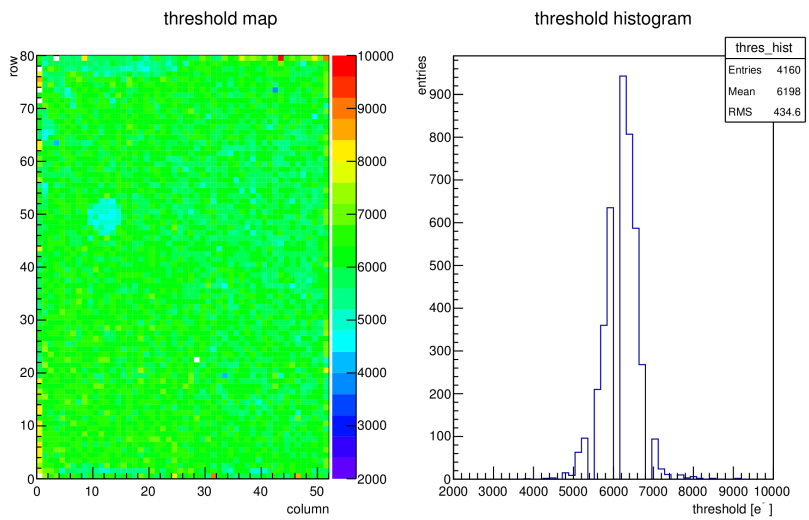

Figure D.4: Example of the threshold analysis results for detectors FBK 2E_9, batch ATLAS08, wafer W8.

The obtained threshold values are rather high in comparison with the one set for the laboratory measurements (3900 e^-). This can affect the tracking precision when the deposited charge is shared among several pixels. Another problem is the high RMS. This is due to the fact that the trimming procedure is not implemented on the CAPTAIN DAQ system. These results are used

DUT	Threshold [e^-]	RMS [e^-]
FBK_1E_1 (ATLAS08_W8)	4407	891
FBK_1E_2 (ATLAS08_W8)	6245	428
FBK_2E_9 (ATLAS08_W8)	7000	549
FBK_4E_12 (ATLAS08_W8)	6671	527
FBK_1E_2 (ATLAS09)	7392	239
FBK_1E_3 (ATLAS09)	7009	334
FBK_1E_1 (ATLAS08_W8) ($5 \cdot 10^{15}$ p/cm^2)	5429	446
FBK_1E_2 (ATLAS08_W8) ($1 \cdot 10^{15}$ p/cm^2)	6125	432
FBK_1E_2 (ATLAS08_W8) ($1 \cdot 10^{15}$ p/cm^2)	4805	575
FBK_2E_9 (ATLAS08_W8) ($1 \cdot 10^{15}$ p/cm^2)	5534	593
FBK_4E_14 (ATLAS08_W8) ($1 \cdot 10^{15}$ p/cm^2)	6859	482
CNM_12-2_75B ($5 \cdot 10^{14}$ p/cm^2)	5470	1418
CNM_17-1_62O ($1 \cdot 10^{15}$ p/cm^2)	5763	1063

Table D.1: Summary of threshold analysis for 3D detectors tested at FNAL.

for the testbeam data analysis which is in progress.

Bibliography

[1] H. Bethe and W. Heitler, "On the stopping of fast particles and on the creation of positive electrons," in *Proc. Royal Soc. London*, vol. A 146, pp. 83–112, 1934.

[2] J. Beringer et al. (Particle Data Group), "Particle Physics booklet," *Phys. Rev.*, vol. D 86, 2012.

[3] F. Rivero, "Characterization of FBK-irst 3D Double Side Double Type Column Silicon Sensors," Master's thesis, Università degli Studi di Torino, 2009.

[4] L. Rossi et al., *Pixel Detectors - From Fundamentals to Applications*. Springer, 2006.

[5] S. M. Sze and K. K. Ng, *Physics of Semiconductor Devices*. McGraw-Hill Company, 2002.

[6] M. Krammer, "Silicon Detectors." Presentation. Praktikum 2010/2011, Institute of High Energy Physics, Vienna, Austria.

[7] G. Lindström et al., "Radiation hardness of silicon detectors - a challenge from high-energy physics," *Nucl. Instrum. Meth.*, vol. A 426, pp. 1–15, 1999.

[8] M. Moll, *Radiation Damage in Silicon Particle Detectors*. PhD thesis, Hamburg university, 1999.

[9] M. Friedl et al., "CVD diamond detectors for ionizing radiation," *Nucl. Instrum. Meth.*, vol. A 435, pp. 194–201, 1999.

[10] J. C. Angus and C. C. Hayman, "Low-Pressure, Metastable Growth of Diamond and "Diamondlike" Phases," *Science*, vol. 241, pp. 913–921, 1988.

[11] J. Ngadiuba, "A Diamond Pixel Detector for CMS Tracker Upgrade at Super-LHC," Master's thesis, Università di Milano Bicocca, 2012.

[12] J. R. Janesick, *Scientific Charged-Coupled Devices.* SPIE, 2001.

[13] R. Turchetta et al., "A monolithic active pixel sensor for charged particle tracking and imaging using standard VLSI CMOS technology," *Nucl. Instrum. Meth.*, vol. A 458, pp. 677–689, 2001.

[14] N. Wermes, "Pixel Detectors for Charged Particles," *Nucl. Instrum. Meth.*, vol. A 640, pp. 370–379, 2009.

[15] F. Gianotti et al., "Physics potential and experimental challenges of the LHC luminosity upgrade," *Eur. Phys. J.*, vol. C 9, pp. 293–333, 2005.

[16] S. Parcker, C. Kenney, and J.Sengal, "3D — A proposed new architecture for solid-state radiation detectors," *Nucl. Instrum. Meth.*, vol. A 395, pp. 328–343, 1997.

[17] V. Eremin and E. Verbitskaya, "Analytical model for 3D detectors parameterization," *Nucl. Instrum. Meth.*, vol. A 612, pp. 516–520, 2010.

[18] I. Tsveybak, W. Bugg, J. Harvey, and J. Walter, "3D - A proposed new architecture for solid-state radiation detectors," *IEEE Trans. Nucl. Sci.*, vol. 39, pp. 1720–1729, 1992.

[19] C. Kenney, S. Parker, J. Segal, and C. Storment, "Silicon Detectors with 3-D Electrode Arrays: Fabrication and Initial Test Results," *IEEE Trans. Nucl. Sci.*, vol. 46, pp. 1224–1236, 1999.

[20] J. Bhardwaj and H. Ashraf, "Advanced silicon etching using high density plasmas," *SPIE*, vol. 2639, pp. 224–233, 1995.

[21] C. J. Kenney, S. Parker, and E. Walckiers, "Results From 3-D Silicon Sensors With Wall Electrodes: Near-Cell-Edge Sensitivity Measurements as a Preview of Active-Edge Sensors," *IEEE Trans. Nucl. Sci.*, vol. 48, pp. 2405–2410, 2001.

[22] M. Povoli, A. Bagolini, M. Boscardin, G. F. D. Betta, G. Giacomini, E. Vianello, and N. Zorzi, "Slim edges in double-sided silicon 3D detectors," *Journal of Instrumentation*, vol. 7, no. 01, p. C01015, 2012.

[23] "Sintef, Oslo, Norway." Online. Avaiable: `http://www.sintef.no/home/`.

[24] C. Piemonte, M. Boscardin, G.-F. D. Betta, S. Ronchin, and N. Zorzi, "Development of 3D detectors featuring columnar electrodes of the same doping type," *Nucl. Instrum. Meth.*, vol. A 541, pp. 441–448, 2005.

[25] L. Tlustos, J. Kalliopuska, R. Ballabriga, M. Campbell, S. Eranen, and X. Llopart, "Characterisation of a semi 3-D sensor coupled to Medipix2," *Nucl. Instrum. Meth.*, vol. A 580, pp. 897–901, 2007.

[26] Z. Li, W. Chen, Y. Guo, D. Lissauer, D. Lynn, V. Radeka, and G. Pellegrini, "Development, simulation and processing of new 3D Si detectors," *Nucl. Instrum. Meth.*, vol. A 583, pp. 139–148, 2007.

[27] A. Zoboli, M. Boscardin, L. Bosisio, G.-F. D. Betta, C. Piemonte, S. Ronchin, and N. Zorzi, "Double-Sided, Double-Type-Column 3-D Detectors: Design, Fabrication, and Technology Evaluation," *IEEE Trans. Nucl. Sci.*, vol. 55, pp. 2775–2784, 2008.

[28] Gian-Franco Dalla Betta et al., "Development of Modified 3D Detectors at FBK," *IEEE Nucl. Sci. Symp. Conf. Rec.*, vol. 2010, 2010.

[29] M. Capeans et al., "ATLAS Insertable B-Layer Technical Design Report," tech. rep., CERN-LHCC-2010-013, 2010.

[30] G. Pellegrini et al., "First double-sided 3-D detectors fabricated at CNM-IMB," *Nucl. Instrum. Meth.*, vol. A 592, pp. 38–43, 2008.

[31] "3D silicon sensors: Design, large area production and quality assurance for the ATLAS IBL pixel detector upgrade," *Nucl. Instrum. Meth.*, vol. A 694, pp. 321–330, 2012.

[32] M. Karagounis et al., "Development of the ATLAS FE-I4 pixel readout IC for B-layer Upgrade and Super-LHC," *CERN-2008-008*, pp. 70–75, 2009.

[33] Ivan Perić et al., "The FEI3 Readout Chip forthe ATLAS Pixel Detector," *Nucl. Instrum. Meth.*, vol. A 565, pp. 178–187, 2006.

[34] M. Barbero et al., "A new ATLAS pixel front-end IC for upgraded LHC luminosity," *Nucl. Instrum. Meth.*, vol. A 604, pp. 397–399, 2009.

[35] C. da Viá et al., "3D active edge silicon sensors with different electrode configurations: Radiation hardness and noise performance," *Nucl. Instrum. Meth.*, vol. A 604, pp. 505–511, 2009.

[36] F. Lemeilleur et al., "Study of characteristics of silicon detectors irradiated with 24 GeV/c protons between −20 ℃ and +20℃," *Nucl. Instrum. Meth.*, vol. A 360, pp. 438–444, 1995.

[37] G. Casse et al., "Performances of miniature microstrip detectors made on oxygen enriched p-type substrates after very high proton irradiation," *Nucl. Instrum. Meth.*, vol. A 535, pp. 362–365, 2004.

[38] T. Rohe et al., "Fluence dependence of charge collection of irradiated pixel sensors," *Nucl. Instrum. Meth.*, vol. A 552, pp. 232–238, 2005.

[39] G. Kramberger at al., "Trapping in silicon detectors." Workshop on Defect Analysis in Silicon Det, Hamburg, August 2006.

[40] S. Sze, *Semiconductor Devices, Physics and Technology.* John Wiley & Sons, 1985.

[41] E. Alagoz et al., "Simulation and laboratory test results of 3D CMS pixel detectors for HL-LHC," *Journal of Instrumentation*, vol. 7, no. 08, p. P08023, 2012.

[42] m. Povoli et al., "Impact of the layout on the electrical characteristics of double-sided silicon 3D sensors fabricated at FBK," *Nucl. Instrum. Meth.*, vol. A 699, pp. 22–26, 2011.

[43] M. Obertino et al., "Performance of CMS 3D silicon pixel detectors before and after irradiation," in *Nucl. Instrum. Meth.*, 2013.

[44] M. Obertino et al., "3D-FBK pixel sensors with CMS readout: First test results," *Nucl. Instrum. Meth.*, vol. A 718, pp. 342–344, 2012.

[45] P. S. Institut, *PSI46 Pixel Chip - External Specification*, 2004.

[46] H. Chr. Kästli et al., "Design and performance of the CMS pixel detector readout chip," *Nucl. Instrum. Meth.*, vol. A 565, pp. 188–194, 2006.

[47] E. Vianello et al, "Optimization of double side 3D detector technology for first production at FBK," *IEEE Nucl. Sci. Symp. Conf. Rec.*, vol. 2011, pp. 523–528, 2011.

[48] G-F Dalla Betta. private communication.

[49] A. Starodumov et al., "Qualification Procedures of the CMS Pixel Barrel Modules," *Nucl. Instrum. Meth.*, vol. A 565, pp. 67–72, 2006.

[50] C. Eggel, *CMS pixel module qualification and search for $B_s^0 \to \mu^+\mu^-$*. PhD thesis, Zurich, ETH, 2009.

[51] W. Gu, *Characterization of the CMS Pixel Detectors*. PhD thesis, Aachen, Tech. Hochsch., 2002.

[52] G. Favro, *Studio delle prestazioni del rivelatore centrale di tracciamento dell'esperimento CMS*. PhD thesis, Università degli Studi di Torino, 2002.

[53] *MS 85E User Manual APOLLO & IntelliStage Stepper Motor Controllers*, 2005.

[54] *C-860.10 Mercury Operating Manual MS 67E*, 2002.

[55] "The CMS tracker system project: Technical Design Report," tech. rep., CERN-LHCC-98-006, 1998.

[56] "Fermilab Test Beam Facility Website." Online. Avaiable: `http://www-ppd.fnal.gov/FTBF/`.

[57] M. Turqueti et al., "CAPTAN: A hardware architecture for integrated data acquisition, control, and analysis for detector development," 2008. FERMILAB-PUB-08-527-CD.

Acknowledgement

This thesis has been realised during almost a year when I had the possibility to improve my knowledge in various fields thanks to lots of people. Besides receiving fundamental advises, I could establish with them good friendship outside the work time.

I would like to express my acknowledgement to Prof. Ada Solano and Dott. Margherita Obertino for their guidance, support and continuous encouragement. A special thanks goes also to Dott. Marta Ruspa for her careful reading of the thesis.

I also have to thank Dott. Natale Demaria whose help was essential for the laser setup realization and for the discussion of the results. For this setup I received an enormous help from Giorgio Cotto for the LabVIEW software and for the several hardware inconvenient which I faced. A special thanks goes to Franco Benotto, who is the designer of the laser board and helped me a lot with it. For controlling the laser board via RS-232, an interface board was realised by Pier Paolo Trapani, who gave me essential advices while deriving the protocol of this communication mode. For building the setup I would also like to thank Ottavio Giuliano for the realization of the mechanical pieces used for fixing the detector and the focusing lens. Advices of Dott. Stefania Beolè and Dott. Francesco Prino have been of great help the for laser setup, thanks to their experience with similar devices.

I wish to acknowledge the help provided by Dott. Helio Nogima for measurements done at CERN with the radioactive source. I would like to offer my special thanks to Dott. Henning Larsen and Dott. Beat Meier for the help given to me on understanding the PSI board functionality. I am particularly grateful for the assistance given by Daniel Pitzl on the external trigger of the PSI board. I would like to especially special thank Dott. Angelo Rivetti and Dott. Tilman Rohe for the advices of the PSI46 DAC settings, in particular for their optimization for the laser test. For the part concerning 3D sensors, I am particularly grateful for the assistance given by Prof. Gian-Franco Dalla Betta.

I wish to acknowledge the help provided by Dott. Paolo De Remigis and

Florea Dumitrache for the pitcures of the detectors.

I am particularly grateful for the assistance given by Dott. Nadia Pastrone and Dott. Silvia Maselli with the CERN and INFN associations.

I ringraziamenti più grandi, però, vanno alla mia famiglia ed a Laura che mi hanno sempre sostenuto durante tutto il percorso di studi. Grazie per l'aiuto a superare i molti momenti difficili ed ad avermi spronato a dare sempre il massimo. Grazie di cuore.